



Title	Study on the Thermoelectric Properties of SrTiO <sub>3</sub> -SrNbO <sub>3</sub> Solid Solutions using the Epitaxial Thin Films and the Artificial Superlattices
Author(s)	Zhang, Yuqiao
Citation	北海道大学. 博士(情報科学) 甲第13515号
Issue Date	2019-03-25
DOI	10.14943/doctoral.k13515
Doc URL	<a href="http://hdl.handle.net/2115/74193">http://hdl.handle.net/2115/74193</a>
Type	theses (doctoral)
File Information	Yuqiao_Zhang.pdf



[Instructions for use](#)

**Study on the Thermoelectric Properties of SrTiO<sub>3</sub>-  
SrNbO<sub>3</sub> Solid Solutions using the Epitaxial Thin Films  
and the Artificial Superlattices**

エピタキシャル薄膜と人工超格子を用いた SrTiO<sub>3</sub>-  
SrNbO<sub>3</sub> 固溶体の熱電特性に関する研究

**YUQIAO ZHANG**

**Graduate School of Information Science and  
Technology, Hokkaido University**



# Content

<b>1. General Introduction.....</b>	<b>1</b>
1.1 Introduction to thermoelectrics .....	1
1.2 Oxide thermoelectrics .....	6
1.2.1 Layered cobaltites .....	6
1.2.2 CaMnO <sub>3</sub> .....	7
1.2.3 ZnO .....	8
1.2.4 SrTiO <sub>3</sub> .....	8
1.3 2D electron system in SrTiO <sub>3</sub> .....	10
1.3.1 Electron doped SrTiO <sub>3</sub> superlattices .....	12
1.3.2 SrTiO <sub>3</sub> based heterostructures .....	13
1.3.3 SrTiO <sub>3</sub> based field effect transistor .....	15
1.4 Outline of thesis .....	17
References .....	19
<b>2. Experimental Methods .....</b>	<b>25</b>
2.1 Synthesis method of thermoelectric materials .....	25
2.1.1 Bulk ceramic synthesis .....	25
2.1.2 Bulk single crystal synthesis .....	26
2.1.3 Epitaxial films.....	30
2.2 Structure characterizations .....	34
2.3 Band calculations .....	37
References .....	38
<b>3. Thermoelectric phase diagram of the SrTiO<sub>3</sub>–SrNbO<sub>3</sub> solid solution system .</b>	<b>41</b>
3.1 Introduction .....	41
3.2 Experimental.....	43
3.3 Results and discussion .....	44
3.4 Conclusion.....	55
References .....	56
<b>4. Fabrication and Thermoelectric Properties of SrTi<sub>1-x</sub>Nb<sub>x</sub>O<sub>3</sub> SrTiO<sub>3</sub> (0.1 ≤ x ≤ 0.9) Superlattices.....</b>	<b>60</b>

*Content*

4.1	Introduction .....	60
4.2	Experimental.....	64
4.3	Results and discussion .....	66
4.4	Conclusion.....	75
	References .....	76
<b>5.</b>	<b>Summary .....</b>	<b>79</b>
	<b>Acknowledgements .....</b>	<b>81</b>
	<b>Publication Lists .....</b>	<b>83</b>
	<b>Presentation Lists .....</b>	<b>84</b>

## 1. General Introduction

### 1.1 Introduction to thermoelectrics

Securing a reliable source of energy always has been the primary concern for humankind since the first industrial revolution. However, even in modern society, most of energy resources are wasted in forms of heat, which can even reach to 60% of the primary energy. Therefore, there are increasing attentions on thermoelectric energy conversion since it can directly convert waste heat to electricity<sup>1,2</sup>. In general, thermoelectric effect can be divided into “Seebeck effect”, “Pielter effect” and “Thomson effect”.

The principle of thermoelectric energy conversion was first discovered by T.J. Seebeck in 1821<sup>3</sup>. He found that the two ends of a metal bar at different temperatures exhibit a voltage difference. Thus, when electric loads are connected at both ends of the metal bar, electric current can be obtained. This phenomenon is now known as the Seebeck effect. As shown in Fig.1.1(a), when a temperature difference ( $\Delta T$ ) is introduced to both ends of a thermoelectric material, the charge carriers will be pushed away from the hot side to the cold side. Correspondingly, a potential difference ( $\Delta V$ ) will be generated.  $\Delta V$  is proportional to  $\Delta T$ , and their ratio is called thermopower ( $\equiv$ Seebeck coefficient),

$$S = \frac{\Delta V}{\Delta T} \quad (1-1)$$

In 1834, J.C.A. Peltier discovered that applying electric current to the heterogeneous metal circuit heated or cooled the junction. He named this phenomenon as Peltier effect, which utilize electricity to control the flow of heat. This has been commercially applied

1. General Introduction

for electronic refrigerators [Fig. 1.1(b)]. Pielter effect could be quantified by the Pielter coefficient,

$$\Pi = \frac{q}{I} \quad (1-2)$$

where  $\Pi$  is Pielter coefficient,  $q$  is the heating/cooling rate and  $I$  is current. The Pieltier coefficient is also regarded as the energy carried per unit charge.

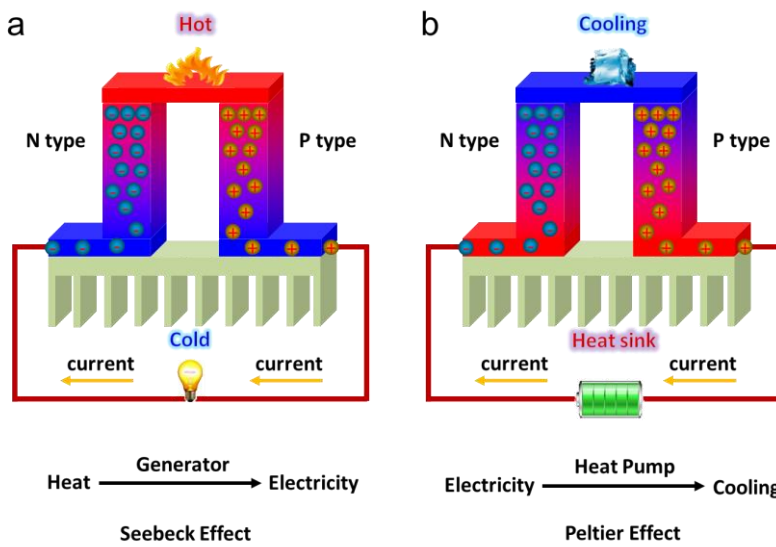


**Figure 1.1.** Schematic illustrations of (a) Seebeck effect and (b) Peltier effect.

Although the Seebeck effect and Pielter effect can be defined in a single material, they were all firstly discovered in a circuit connected by two conductors. However, in a single semiconductor, if there is a temperature difference along the trajectory of electrical current, there will be a continuous Pielter effects gradient as the thermopower depends on the temperature. This effect was discovered by William Thomson in 1854 and is now called the Thomson effect. The heating/cooling rate of Thomson effect can be express as:

$$q = \tau_T \cdot I \cdot \Delta T \quad (1-3)$$

where  $\tau_T$  is Thomson coefficient.

## 1. General Introduction

Seebeck effect, which realizes the power generation from waste heat, is the main focus for the thermoelectrics research. Generally, the maximum power generation efficiency ( $\eta_{\max}$ ) of thermoelectric materials could be calculated by:

$$\eta_{\max} = \frac{T_h - T_c}{T_h} \frac{\sqrt{1 + ZT} - 1}{\sqrt{1 + ZT} + T_c/T_h} \quad (1-4)$$

where  $ZT$  is a dimensionless figure of merit,  $T_h$  is the temperature of the hot side and  $T_c$  is the temperature of the cold side. Usually we use the  $ZT$  value to indicate the overall performance of a thermoelectric material. The  $ZT$  is expressed as:

$$ZT = \frac{S^2 \cdot \sigma \cdot T}{\kappa} \quad (1-5)$$

where  $T$  is the absolute temperature,  $S$  is the thermopower ( $\equiv$  Seebeck coefficient),  $\sigma$  is electrical conductivity and  $\kappa$  is thermal conductivity. Therefore, a good thermoelectric material should have large  $S$ , which is required to obtain high voltage, high  $\sigma$ , which is required to maintain high current, and low  $\kappa$ , which is required to create a large temperature difference between the ends of the material. The  $|S|$  of a thermoelectric material can be expressed by the Mott equation <sup>4</sup>,

$$S = \frac{\pi^2 k_B^2 T}{3 e} \left\{ \frac{d[\ln(\sigma(E))]}{dE} \right\}_{E=E_F} = \frac{\pi^2 k_B^2 T}{3 e} \left\{ \frac{1}{n} \cdot \frac{dn(E)}{dE} + \frac{1}{\mu} \cdot \frac{d\mu(E)}{dE} \right\}_{E=E_F} \quad (1-6)$$

where  $k_B$ ,  $e$ ,  $n$ ,  $E_F$ , and  $\mu$  are the Boltzmann constant, electron charge, carrier concentration, Fermi energy, and carrier mobility, respectively. As shown in [Fig. 1.2](#), the  $ZT$  value of a thermoelectric material must be maximized by means of  $n$  because of the commonly observed trade-off relationship between  $S(n)$  and  $\sigma(n)$ :  $|S|$  decreases rapidly with increasing  $n$  while  $\sigma$  increases almost linearly ( $\sigma = n \cdot e \mu$ ). In addition,  $\kappa$  is a very important factor for enhancing the  $ZT$  value.  $\kappa$  is comprised of two major components: the electron thermal conductivity ( $\kappa_{\text{ele}}$ ) and lattice thermal conductivity ( $\kappa_{\text{lat}}$ ).  $\kappa_{\text{ele}}$  is closely

related to  $\sigma$  by the Wiedemann-Franz law<sup>5</sup>,

$$\kappa_{\text{ele}} = L \cdot \sigma \cdot T = L n \cdot e \cdot \mu \cdot T \quad (1-7)$$

where  $L$  is the Lorenz number. As indicated by equation (1-7), the  $\kappa_{\text{ele}}$  increases linearly with  $n$ .  $\kappa_{\text{lat}}$  is the only one factor that does not depend strongly on  $n$ . For these reasons, most studies are focused on maximizing power factor ( $\text{PF} = S^2\sigma$ ) and minimize  $\kappa_{\text{lat}}$ .

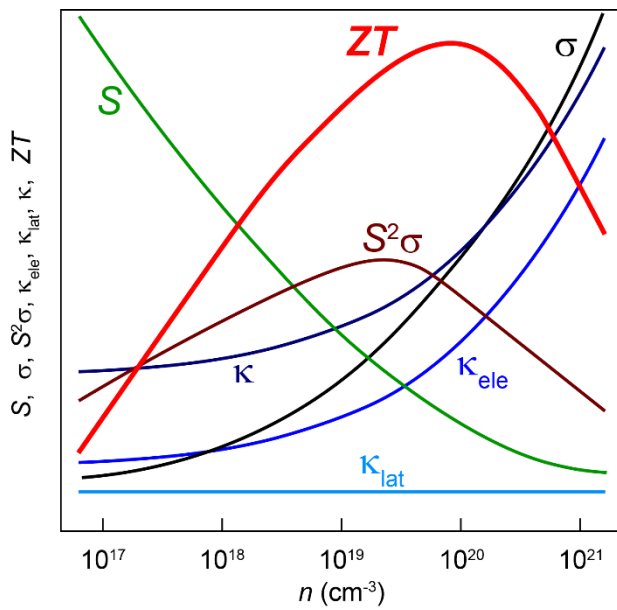


**Figure 1.2.** Schematic diagram of relationship between  $ZT$  value, thermopower ( $S$ ), electrical conductivity ( $\sigma$ ), power factor ( $\text{PF} = S^2\sigma$ ) and thermal conductivity [ $\kappa$ , sum of electron thermal conductivity ( $\kappa_{\text{ele}}$ ) and lattice thermal conductivity ( $\kappa_{\text{lat}}$ )].

The  $ZT$  values of practical thermoelectric materials such as  $\text{Bi}_2\text{Te}_3$  and  $\text{PbTe}$  are  $\approx 1$ , which is now considered as the lowest requirement for practical applications.<sup>6,7</sup> Examples of high-performance thermoelectric materials are summarized in [Fig. 1.3](#)<sup>8</sup>.

## 1. General Introduction

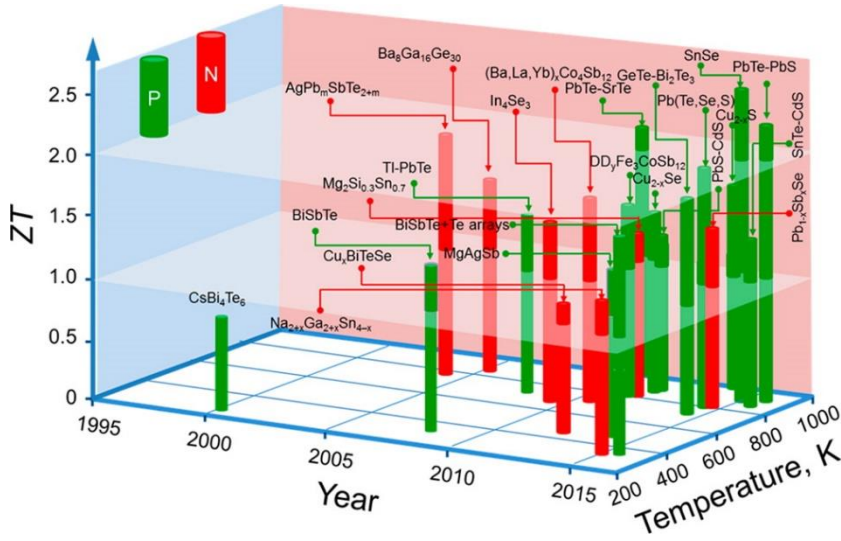


**Figure 1.3.** Current representative state-of-the-art thermoelectric materials<sup>8</sup>. The thermoelectric figure of merit  $ZT$  is plotted as a function of temperature and year (Green cylinders represent the p-type materials, while red cylinders represent the n-type ones). CsBi<sub>4</sub>Te<sub>6</sub><sup>9</sup>, BiSbTe<sup>10</sup>, AgPbmSbTe<sub>2+m</sub><sup>11</sup>, Ba<sub>8</sub>Ga<sub>16</sub>Ge<sub>30</sub><sup>12</sup>, TI-PbTe<sup>13</sup>, In<sub>4</sub>Se<sub>3</sub><sup>14</sup>, Cu<sub>x</sub>BiTeSe<sup>15</sup>, (BaLaYb)<sub>x</sub>Co<sub>4</sub>Sb<sub>12</sub><sup>16</sup>, MgAgSb<sup>17</sup>, BiSbTe+Te arrays<sup>18</sup>, PbTe-SrTe<sup>19</sup>, DD<sub>y</sub>Fe<sub>3</sub>CoSb<sub>12</sub><sup>20</sup>, Mg<sub>2</sub>Si<sub>0.3</sub>Sn<sub>0.7</sub><sup>21</sup>, Cu<sub>2-x</sub>Se<sup>22</sup>, Na<sub>2+x</sub>Ga<sub>2+x</sub>Sn<sub>4-x</sub><sup>23</sup>, GeTe-Bi<sub>2</sub>Te<sub>3</sub><sup>24</sup>, Pb(Te,Se,S)<sup>25</sup>, PbS-CdS<sup>26</sup>, SnSe<sup>27</sup>, Cu<sub>2-x</sub>S<sup>28</sup>, PbTe-PbS<sup>29</sup>, SnTe-CdS<sup>30</sup>, and Pb<sub>1-x</sub>Sb<sub>x</sub>Se<sup>31</sup>.

As traditional thermoelectric materials, Bi<sub>2</sub>Te<sub>3</sub> and PbTe based compounds play important roles in the thermoelectric devices<sup>10,11,13,19,25,26,29,31-33</sup>. However, the low abundance and high toxicity of Pb/Te create demands for developing other harmless compounds showing comparable or higher performance at low-cost. Many alternative materials have been investigated, including MgAgSb<sup>17</sup>, skutterudites<sup>16,20</sup>, and copper/tin chalcogenides<sup>22,27,28,30</sup>. Particularly, single crystalline SnSe shows record high  $ZT$  values of 2.6 in p-type and 2.8 in n-type<sup>27,34</sup>. However, since most of the thermoelectric devices are designed to be used at high temperature ( $\geq 500$  °C), even though they showed high  $ZT$

value, these are not so attractive because decomposition, vaporization or melting of the constituents can easily occur at high temperatures. Therefore, even today, there are ongoing debates on the reliability and practicality of these materials in device applications.

## 1.2 Oxide thermoelectrics

Based on this background, recently, metal oxides are attracting increasing attentions for thermoelectric power generations at high temperatures on the basis of their advantages over heavy metallic alloys in chemical and thermal robustness<sup>35-37</sup>. In fact, there is a long history for the developments in oxide thermoelectrics. During 1950's and 1970's, the pioneering studies were performed on thermoelectric properties of simple conducting oxides, such as CdO<sup>38</sup>, NiO<sup>39</sup>, ZnO<sup>40</sup>, In<sub>2</sub>O<sub>3</sub><sup>41</sup>, SrTiO<sub>3</sub><sup>42</sup>, rutile-TiO<sub>2</sub><sup>43</sup>, SnO<sub>2</sub><sup>44</sup>, Cu<sub>2</sub>O<sup>45</sup> and Fe<sub>3</sub>O<sub>4</sub><sup>46</sup>. In 1986, the discovery of cuprous oxide based high  $T_c$  superconducting oxide created another wave of studies on the thermoelectric properties of superconducting oxides, such as La<sub>2</sub>CuO<sub>4</sub><sup>47</sup>, La-Ba-Cu-O<sup>48</sup>, YBa<sub>2</sub>Cu<sub>3</sub>O<sub>7- $\delta$</sub> <sup>49</sup> and Tl-Ca-Ba-Cu-O<sup>50</sup>. Most recently, the discovery of CaMnO<sub>3</sub><sup>51</sup>, Al-doped ZnO<sup>52</sup>, Na<sub>x</sub>CoO<sub>2</sub><sup>53</sup>, Ca<sub>3</sub>Co<sub>4</sub>O<sub>9</sub><sup>54,55</sup> and SrTiO<sub>3</sub><sup>56-58</sup> has attracted even more interest in thermoelectric oxide research, and these materials are also regarded as the most promising oxides to replace their heavy metal based counterparts.

### 1.2.1 Layered cobaltites

For p-type thermoelectric oxides, layered cobaltites show very high potential for replacing heavy metal based thermoelectric materials. The most popular Na<sub>x</sub>CoO<sub>2</sub> and

## 1. General Introduction

$\text{Ca}_3\text{Co}_4\text{O}_9$  were reported by Terasaki *et al.* and Funahashi *et al.*<sup>53,59</sup>. Due to the low spin state of  $\text{Co}^{3+}$ , these materials show very high thermopower<sup>60</sup>. As shown in Fig. 1.4, these two materials are all composed of layer structure.  $\text{CoO}_2$  plane can provide a path for p-type charge transport while layer structures can effectively scatter phonons and reduce the lattice thermal conductivity. This kind of materials is a good example of “phonon-glass, electron-crystal” in thermoelectric materials design<sup>61</sup>. The highest  $ZT$  values of these materials could reach to 0.15–0.5 at 1000 K for  $\text{Ca}_3\text{Co}_4\text{O}_9$  and 0.3–0.9 at 950 K for  $\text{Na}_x\text{CoO}_2$ .

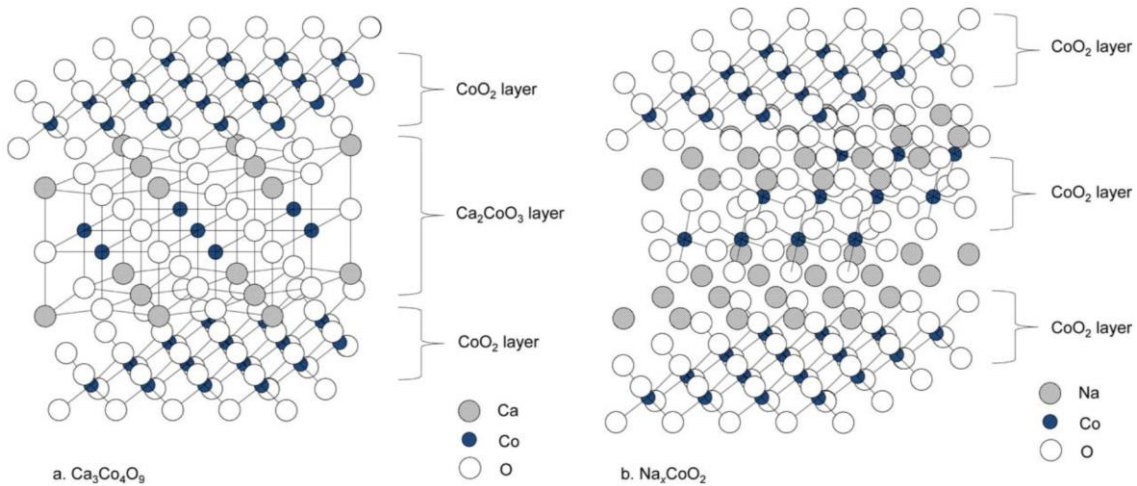


**Figure 1.4.** Schematic structure of (a)  $\text{Ca}_3\text{Co}_4\text{O}_9$  and (b)  $\text{Na}_x\text{CoO}_2$ <sup>62</sup>.

### 1.2.2 $\text{CaMnO}_3$

$\text{CaMnO}_3$  is one of the most widely known perovskites for its electrical and magnetic properties at room temperature or below<sup>63-66</sup>.  $\text{CaMnO}_3$  is an n-type semiconductor which could be doped either at A site or B site. In 1995, Ohtaki *et al.* reported its high temperature thermoelectric performance after different dopings at A sites<sup>51</sup>. It was found

## 1. General Introduction

ytterbium doping could increase both electrical conductivity and thermopower, enhancing the  $ZT$  value<sup>67,68</sup>. In addition, if ytterbium is co-doped with dysprosium, the electrical conductivity could be increased while thermal conductivity could be reduced. The optimal  $ZT$  value could reach to 0.1-0.2 at 1000 K, which makes  $\text{CaMnO}_3$  a good candidate for high temperature applications.

### 1.2.3 ZnO

ZnO is another very promising oxide thermoelectric material at high temperatures. ZnO is a wide bandgap semiconductor. To make it into a thermoelectric material, adequate doping is required to introduce n-type conduction, and Aluminum is the most widely adopted doping element. Doping appropriate amount of Al introduces conduction electrons and refines the grains, which suppresses the thermal conductivity. Other dopings such as nickel, titanium, tin and antimony, are also used to modulate electron and phonon transports of ZnO<sup>69-72</sup>. At 1073 K,  $ZT$  value of ZnO could be optimized to 0.5.

### 1.2.4 SrTiO<sub>3</sub>

$\text{SrTiO}_3$  is known for its special behaviors in superconductivity and ferroelectricity. It is also a famous single crystal substrate for epitaxial growth of other materials with similar lattice structures, such as  $\text{SrRuO}_3$ ,  $\text{LaAlO}_3$ ,  $\text{FeSe}$ , etc.. As shown in Fig. 1.5, pure  $\text{SrTiO}_3$  (space group  $\text{Pm}\bar{3}\text{m}$ , cubic perovskite structure,  $a = 3.905 \text{ \AA}$ ) is an insulator with a bandgap of 3.2 eV, of which the bottom of the conduction band is composed of triply degenerate, empty Ti 3  $d-t_{2g}$  orbitals while the top of the valence band is composed of

fully occupied O 2p orbitals<sup>73</sup>. The electrical conductivity of SrTiO<sub>3</sub> can be easily controlled from insulator to metal by substitutional doping of La<sup>3+</sup> or Nb<sup>5+</sup>.

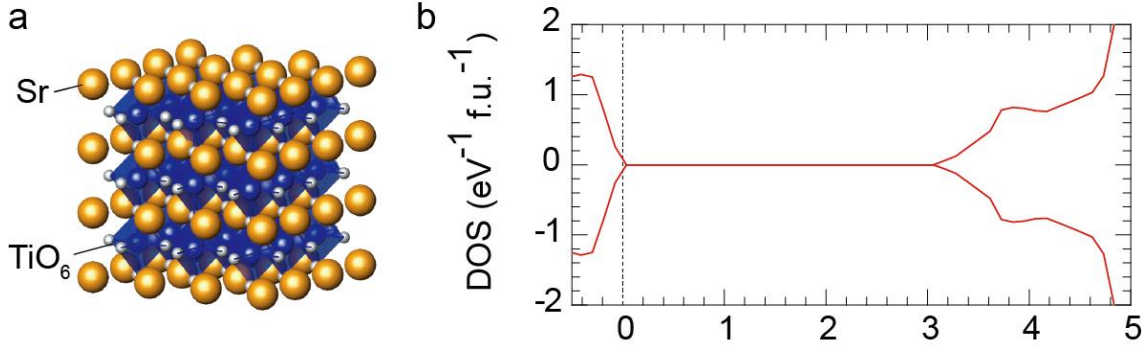


**Figure 1.5.** (a) Crystal structure and (b) band structure of pure SrTiO<sub>3</sub>.

In 2001, Okuda *et al.* reported large thermoelectric power factors from (2.8–3.6 mW m<sup>-1</sup> K<sup>-2</sup>) Sr<sub>1-x</sub>La<sub>x</sub>TiO<sub>3</sub> (0 ≤ x ≤ 0.1) single crystals fabricated by floating-zone method<sup>56</sup>. After that, Ohta *et al.* clarified thermoelectric transport properties of Nb- and La-doped SrTiO<sub>3</sub> single crystals ( $n_e \sim 10^{20}$  cm<sup>-3</sup>) at high temperatures (~1000 K)<sup>57</sup>, and the experimental data indicated that  $ZT$  value could be further optimized by heavily Nb doping. However, due to the solubility limit of Nb<sup>5+</sup> in SrTiO<sub>3</sub>, it was very difficult to fully clarify the enhancement using bulk crystals. Therefore, using epitaxial films, Ohta *et al.* further increased  $n_e$  by doping Nb to  $\sim 2 \times 10^{21}$  cm<sup>-3</sup> and got an enhanced  $ZT$  value of 0.37 at 1000 K<sup>58</sup>.

Although lots of promising oxide based thermoelectric materials have been examined to date, their  $ZT$  values are compared low compared to the minimum applicable level ( $ZT \geq 1$ ). These studies suggest that it is almost impossible to further improve the  $ZT$  value of thermoelectric oxides in the conventional three-dimensional (3D) bulk states.

### 1.3 2D electron system in SrTiO<sub>3</sub>

In optoelectronic devices, two-dimensional (2D) structures usually show exotic electron transport properties compared with their bulk counterparts due to the increased density of state (DOS) near the conduction band or the valence band edges with decreasing quantum well thickness. In 1993, Hicks and Dresselhaus theoretically predicted similar 2D enhancement effects in thermoelectric materials. In other words, two-dimensional thermoelectric figure of merit,  $Z_{2D}T$ , of quantum well can dramatically be enhanced compared to the  $ZT$  of 3D systems if the well thickness is narrower than the de Broglie wavelength ( $\lambda_D = \left(\frac{2\pi\hbar}{m^*k_B T}\right)^{1/2}$ , where  $\hbar$ ,  $m^*$  and  $k_B$  are reduced Planck's constant, effective mass of conductive electron or hole, and Boltzmann constant, respectively)<sup>74</sup>. The increased DOS only enhances  $S$  without sacrificing electrical conductivity, resulting in the rise of PF.

The 2D enhancement effect in the thermoelectric performance was first calculated assuming that the electrons were in simple parabolic bands and occupied the lowest subband of the quantum well. The 2D electron dispersion relations is given by:

$$\varepsilon_{2D}(k_x, k_y) = \frac{\hbar^2 k_x^2}{2m_x} + \frac{\hbar^2 k_y^2}{2m_y} + \frac{\hbar^2 \pi^2}{2m_z d_W^2} \quad (1-8)$$

where  $d_W$  is the width of quantum well, and  $m_x$ ,  $m_y$  and  $m_z$  are the effective mass tensor components of the constant energy surfaces. According to the Mott equation (1-6),  $S$  is proportional to the slope of DOS(E) at the Fermi level ( $E_F$ ):  $\left[\frac{\partial \text{DOS}(E)}{\partial E}\right]_{E=E_F}$ . As shown in

**Fig. 1.6(a)**, by the 2D confinement electronic, the DOS will be modified from 3D state to 2D state, resulting in an infinite slope along the  $z$  direction<sup>75</sup>. This will increase the density of states per unit volume and per unit energy ( $g(E)$ ) and therefore the energy-dependence

## 1. General Introduction

of  $n(E) = g(E)f(E)$  in the Mott relationship, where  $f(E)$  is the Fermi function. This concept can also be expressed in terms of the effective mass  $m_d^*$  by the following equations<sup>13</sup>,

$$S = \frac{8\pi^2 k_B^2 T}{3qh^2} m_d^* \left(\frac{\pi}{3n}\right)^{2/3} \quad (1-9)$$

where  $m_d^*$  is given by

$$m_d^* = \left(\frac{g(E)\hbar^3\pi^2}{\sqrt{2E}}\right)^{3/2} \quad (1-10)$$

By increasing the  $m_d^*$  from  $g(E)$ ,  $S$  can be enhanced accordingly. In this case,  $\lambda_D$  plays a very important role in dividing the 3D state and 2D state. Furthermore, as shown in Fig. 1.6(b), in addition to  $x$ - $z$  plane, the 2D effect will also increase the thermoelectric performance along the  $x$ - $y$  plane. In 1996, Hicks *et al.* fabricated PbTe/Pb<sub>0.927</sub>Eu<sub>0.073</sub>Te multiple quantum wells (MQWs) and confirmed that decreasing the well thickness from 55 to 17 Å for Pb<sub>1-x</sub>Eu<sub>x</sub>Te/PbTe MQWs increased the ' $S^2n$ ' value by a factor of  $\sim 3$  compared with that of bulk PbTe [Fig. 1.6(c)]<sup>76</sup>.

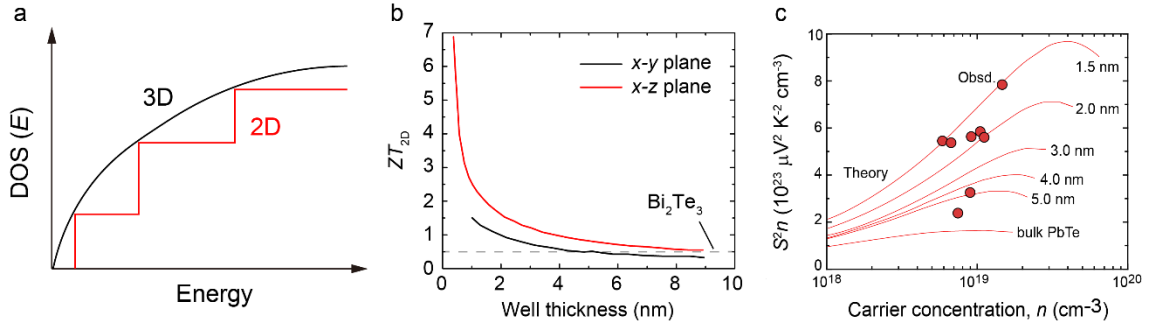


**Figure 1.6.** (a) Electronic density of states for a 3D bulk semiconductor (black curve) and a 2D quantum well (red curve). (b)  $ZT_{2D}$  of quantum well as a function of the layer thickness.  $S^2n$  of PbTe/Pb<sub>0.927</sub>Eu<sub>0.073</sub>Te quantum wells as a function of carrier concentration at 300 K<sup>74-77</sup>.

Similar experiments were also conducted in SrTiO<sub>3</sub> based materials, such as SrTiO<sub>3</sub> based superlattices, heterostructures and field effect transistor structures, which

successfully observed similar 2D enhancement effects in the thermoelectric performance.

### 1.3.1 Electron doped SrTiO<sub>3</sub> superlattices

In 2007, Ohta *et al.* adopted this hypothesis and fabricated SrTiO<sub>3</sub> based superlattices using highly conductive Nb doped SrTiO<sub>3</sub>, which is sandwiched by insulating SrTiO<sub>3</sub> barrier layers<sup>78</sup>. As shown in Fig. 1.7(a) in Cs-corrected high-angle angular dark-field scanning transmission electron microscope (HAADF-STEM), Nb doping was indeed confined perfectly in the single SrTi<sub>0.8</sub>Nb<sub>0.2</sub>O<sub>3</sub> layer. In Fig. 1.7(b), a dramatic increase in thermopower was observed when the SrTi<sub>0.8</sub>Nb<sub>0.2</sub>O<sub>3</sub> layer thickness was below 4 unit cells.  $|S|$  value of one unit thick cell 2D electron gas (2DEG) reached to 480  $\mu\text{V K}^{-1}$ , which is  $\sim 4.4$  times larger than that of SrTi<sub>0.8</sub>Nb<sub>0.2</sub>O<sub>3</sub> bulk value ( $|S| = 108 \mu\text{V K}^{-1}$ ), and the electron transport property remained constant. This resulted in a largely increased  $ZT$  value in 2DEG of  $\sim 2.4$  at room temperature.

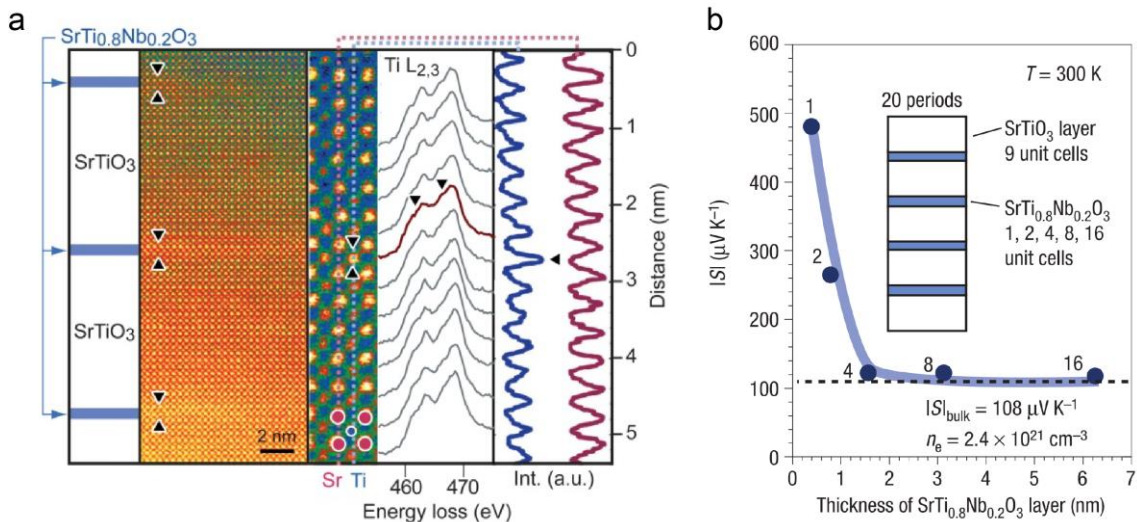


**Figure 1.7.** (a) HAADF-STEM image of [(SrTiO<sub>3</sub>)<sub>24</sub>/(SrTi<sub>0.8</sub>Nb<sub>0.2</sub>O<sub>3</sub>)<sub>1</sub>]<sub>20</sub> superlattice and intensity profiles across Ti and Sr atomic column. Stripe-shaped contrast is clearly seen.

## 1. General Introduction

Furthermore, the intensity of Ti column in one unit cells thickness of  $\text{SrTi}_{0.8}\text{Nb}_{0.2}\text{O}_3$  shows higher intensity than that of  $\text{SrTiO}_3$  barrier layer, confirming that the doped  $\text{Nb}^{5+}$  ions are exclusively confined in the  $\text{SrTi}_{0.8}\text{Nb}_{0.2}\text{O}_3$  layer. (b) Room temperature thermopower of  $\text{SrTiO}_3/\text{SrTi}_{0.8}\text{Nb}_{0.2}\text{O}_3/\text{SrTiO}_3$  superlattices as a function of  $\text{SrTi}_{0.8}\text{Nb}_{0.2}\text{O}_3$  layer thickness<sup>78</sup>.

### 1.3.2 $\text{SrTiO}_3$ based heterostructures

In 2004, Ohtomo *et al.* reported the presence of 2D electron gas (2DEG) at the interface of  $\text{LaAlO}_3/\text{SrTiO}_3$  interface, which exhibits amazingly high Hall mobility ( $\mu_{\text{Hall}}$ ) over  $10000 \text{ cm}^2 \text{ V}^{-1} \text{ s}^{-1}$  at low temperature<sup>79</sup>. This kind of 2DEG exhibits a large phonon drag effect in  $|S|$  at low temperature<sup>80</sup>. Similarly, in  $\text{TiO}_2/\text{SrTiO}_3$  heterostructures, a 2DEG was also observed by Ohta *et al.*<sup>78</sup>. As shown in Fig. 1.8(a),  $\text{TiO}_2$  films were deposited on  $\text{SrTiO}_3$  and  $\text{LaAlO}_3$  substrates, respectively. At the interface of  $\text{TiO}_2/\text{SrTiO}_3$  heterostructure, an increase in carrier concentration ( $n_e \sim 7.0 \times 10^{20} \text{ cm}^{-3}$ ) was observed within a thickness of  $\sim 0.3 \text{ nm}$  (approximately one unit cell of  $\text{SrTiO}_3$ ), and phonon drag peaks were clearly confirmed in  $\text{TiO}_2/\text{SrTiO}_3$  heterostructure, which is much more intense than that of  $\text{SrTiO}_3$  single crystal, indicating the formation of 2DEG [Fig. 1.8(b)].

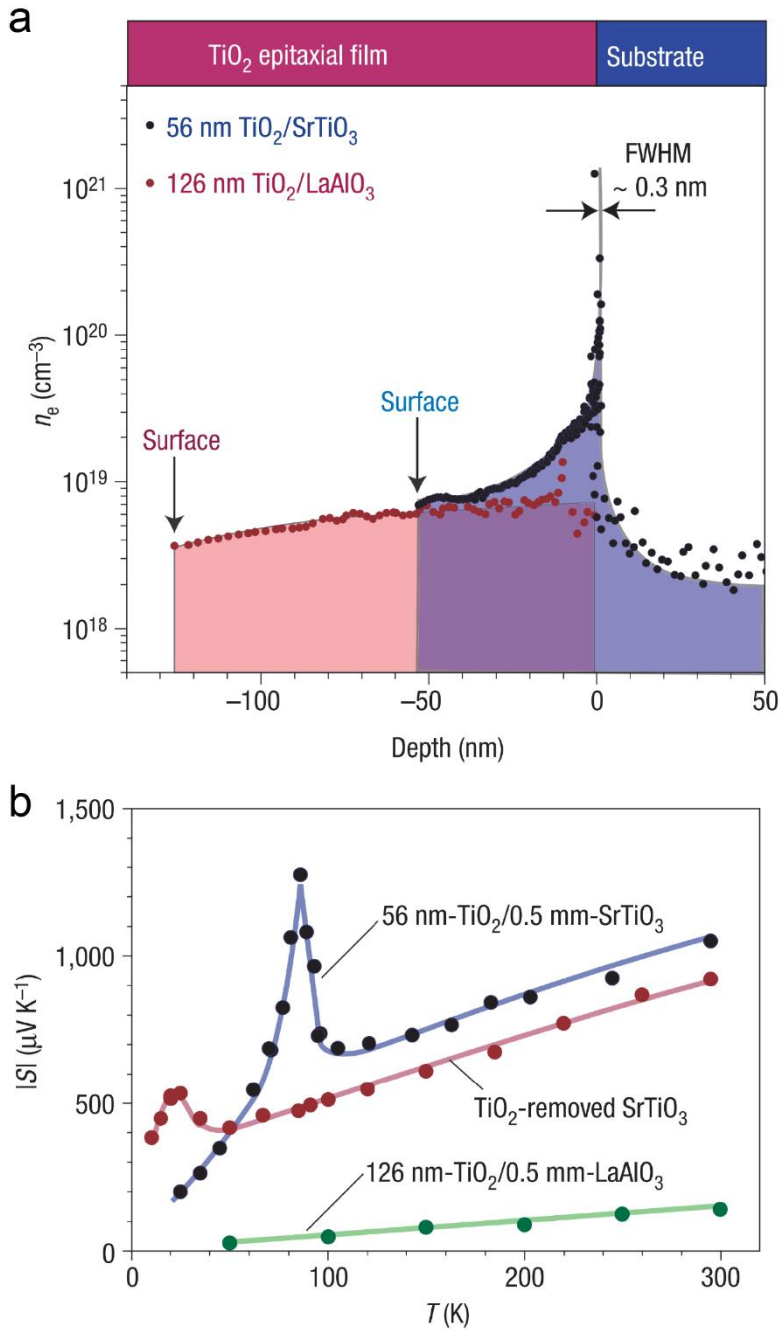


**Figure 1.8.** 2DEG localized at the TiO<sub>2</sub>/SrTiO<sub>3</sub> heterointerface. (a) Depth profile of carrier concentration around the interface between a 56-nm-thick TiO<sub>2</sub> epitaxial film and the SrTiO<sub>3</sub> substrate (blue). That for the interface between a 126-nm-thick epitaxial layer and insulating LaAlO<sub>3</sub> is also plotted for comparison (red). An intense carrier concentration peak ( $n_e \sim 1.4 \times 10^{21} \text{ cm}^{-3}$ ) with a full-width at half maximum of  $\sim 0.3 \text{ nm}$  is

seen at the  $\text{TiO}_2/\text{SrTiO}_3$  heterointerface. (b) Temperature dependence of  $|S|$  and for the  $\text{TiO}_2$  epitaxial films grown on (100)- $\text{SrTiO}_3$  (blue) and (100)- $\text{LaAlO}_3$  (green). Solid-lines are guides for the eyes<sup>78</sup>.

### 1.3.3 $\text{SrTiO}_3$ based field effect transistor

As the fabrication of superlattices can be complicated, Ohta *et al.* developed a simpler alternative technique to confine 2DEG in  $\text{SrTiO}_3$ , which was the utilization of field effect transistors (TFTs)<sup>81</sup>. The configuration of TFT structure is shown in Fig. 1.9(a), where a gate insulator is deposited on  $\text{SrTiO}_3$  single crystal substrate. Due to the n-type characteristic of  $\text{SrTiO}_3$ , when positive voltage is introduced, 2DEG will accumulate at the interface between the gate insulator and  $\text{SrTiO}_3$ . As the thickness of 2DEG ( $t_{\text{eff}}$ ) is narrower than the critical thickness, 2DEG enhanced  $|S|$  could be observed [Fig. 1.9(b)]. The TFT structure could realize an ultimate modification of DOS, which decides the dimensional crossover of  $|S|-n_e$  behaviors. This approach based on the electric field induced 2DEG simply and effectively verified the effectiveness of quantum effect in enhancing  $|S|$ , which may accelerate the development of nanostructures for high performance thermoelectric materials.

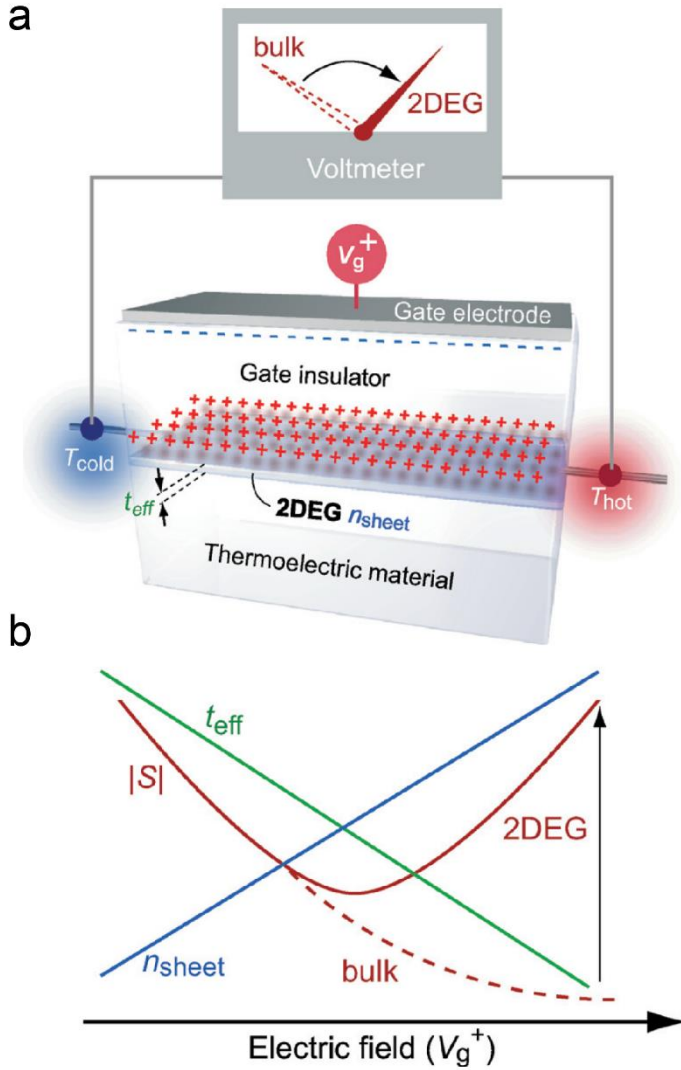


**Figure 1.9.** (a) Configuration of the field effect transistor structure on an n-type thermoelectric material. A 2DEG layer is formed at the gate insulator/semiconductor interface by a positive  $V_g$ .  $S$  of the 2DEG layer (effective thickness:  $t_{\text{eff}}$ , sheet carrier concentration:  $n_{\text{sheet}}$ ) is measured by introducing a temperature gradient at both ends of the 2DEG layer. (b) Electric field modulation of  $|S|$ ,  $n_{\text{sheet}}$  and  $t_{\text{eff}}$ . As the applied electric field increases,  $n_{\text{sheet}}$  (blue) of the 2DEG layer monotonically increases and the  $t_{\text{eff}}$  (green) becomes thinner. When  $t_{\text{eff}}$  is thinner than the critical thickness, unusually large enhancement of  $|S|$  is observed<sup>81</sup>.

#### 1.4 Outline of thesis

Due to the energy crisis, thermoelectric materials are attracting increasing attentions because of their exotic ability to directly convert waste heat into electricity. With the developments in design philosophy and synthesis techniques, many thermoelectric materials with high  $ZT$  value have been developed to date. However, most of these high performance materials are composed of heavy metals with low thermal stability, making it really difficult to apply them in devices operating at high temperatures. To solve this problem, we need alternative thermoelectric materials with higher thermal stability. In this regard, recently discovered oxide based materials are attracting the attentions of thermoelectric scientists and engineers. Among the various oxides, crystalline  $\text{SrTiO}_3$  is one of the most promising candidate due to its high PF, which is comparable to that of commercial  $\text{Bi}_2\text{Te}_3$ . However, difficulties in suppressing the high thermal conductivity hinders the practical device application of  $\text{SrTiO}_3$  based materials. Therefore, further improvements in PF is required to enhance the thermoelectric performance of  $\text{SrTiO}_3$ .

As described earlier, 2DEG in electron doped  $\text{SrTiO}_3$  system is an effective method to enhance the thermoelectric performance, and its effectiveness has already been proven in  $\text{SrTi}_{0.8}\text{Nb}_{0.2}\text{O}_3|\text{SrTiO}_3$  based superlattices. However, high  $ZT$  value could only obtained in thin layers of 2DEG systems. If the presence of the insulating  $\text{SrTiO}_3$  barrier layers, which are essential for the 2D confinement, is taken into consideration, the effective  $ZT$  value is only  $\sim 0.24$  at room temperature. This value is insufficient for practical applications. Due to the solubility limit of  $\text{Nb}^{5+}$  in  $\text{SrTiO}_3$ , few studies have managed to reach heavily Nb doped region. Therefore, clarification of thermoelectric performance for the full range Nb doped  $\text{SrTiO}_3$  system (including bulk-like films and superlattices) is

## 1. General Introduction

required to further improve the performance of SrTiO<sub>3</sub> based materials. In this study, using pulsed laser deposition (PLD), we successfully fabricated high quality SrTi<sub>1-x</sub>Nb<sub>x</sub>O<sub>3</sub> ( $0 \leq x \leq 1$ ) epitaxial films and artificial superlattices. This thesis is mainly composed of two sections:

### 1. Thermoelectric phase diagram of SrTiO<sub>3</sub>-SrNbO<sub>3</sub> full range solid solutions<sup>82</sup>.

In this study, SrTi<sub>1-x</sub>Nb<sub>x</sub>O<sub>3</sub> ( $0.05 \leq x \leq 1$ ) solid solution thin films were epitaxially grown on (001) LaAlO<sub>3</sub> substrates, and a thermoelectric phase diagram for SrTi<sub>1-x</sub>Nb<sub>x</sub>O<sub>3</sub> ( $0 \leq x \leq 1$ ) solid solution system was obtained. We observed two thermoelectric phase boundaries in the system, which originate from the step-like decrease in carrier effective mass at  $x \sim 0.3$  and a local minimum in carrier relaxation time at  $x \sim 0.5$ . These phase boundaries are related to the isovalent/heterovalent B-site substitution: parabolic Ti 3d orbitals dominate electron conduction for compositions with  $x < 0.3$ , whereas the Nb 4d orbital dominates when  $x > 0.3$ . At  $x \sim 0.5$ , a tetragonal distortion of the lattice, in which the B-site is composed of Ti 3d and Nb 4d ions, leads to the formation of tail-like impurity bands, which maximizes the electron scattering. These results provide a foundation for further improving the thermoelectric performance of SrTi<sub>1-x</sub>Nb<sub>x</sub>O<sub>3</sub>.

### 2. Double thermoelectric power factor of a 2D electron system (2DES)<sup>83</sup>.

Based on the thermoelectric phase diagram, we found two different  $\lambda_D$  in the SrTiO<sub>3</sub>-SrNbO<sub>3</sub> full range solid solution system, which are due to the conduction band transition at  $x = 0.3$  ( $x > 0.3$ :  $\lambda_D \sim 5.3$  nm;  $x < 0.3$ :  $\lambda_D \sim 4.1$  nm). Therefore, SrTi<sub>1-x</sub>Nb<sub>x</sub>O<sub>3</sub> is an ideal system to clarify the effectiveness of utilizing two-dimensionality to enhance the thermoelectric PF in superlattice structures. Using superlattices of [ $N$  unit cell SrTi<sub>1-</sub>

## 1. General Introduction

$_{x}\text{Nb}_x\text{O}_3[11 \text{ unit cell SrTiO}_3]_{10}$  ( $0.1 \leq x \leq 0.9$ ), we successfully enhanced the effective PF to  $\sim 5 \text{ mW m}^{-1} \text{ K}^{-2}$ , which doubles the value of optimized bulk  $\text{SrTi}_{1-x}\text{Nb}_x\text{O}_3$ . The present 2DES approach, the use of longer  $\lambda_D$ , is epoch-making and is fruitful for designing good thermoelectric materials.

This study provides the a fundamental contribution for the developments in  $\text{SrTiO}_3$  based thermoelectric materials as well as direct experimental evidences for the effectiveness of 2D quantum wells in enhancing the thermoelectric performance.

## References

- 1 Bhandari, C. & Rowe, D. M. CRC Handbook of thermoelectrics. *CRC Press, Boca Raton, FL*, 49 (1995).
- 2 Goldsmid, H. J. in *Introduction to thermoelectricity* 1-7 (Springer, 2016).
- 3 Seebeck, T. Abh. K. *Akad Wiss (Berlin)*, 265 (1823).
- 4 Cutler, M. & Mott, N. F. Observation of Anderson Localization in an Electron Gas. *Phys. Rev.* **181**, 1336, doi:DOI 10.1103/PhysRev.181.1336 (1969).
- 5 Franz, R. & Wiedemann, G. Ueber die Wärme-Leitungsfähigkeit der Metalle. *Annalen der Physik* **165**, 497-531 (1853).
- 6 Tritt, T. M. & Subramanian, M. A. Thermoelectric materials, phenomena, and applications: A bird's eye view. *MRS Bulletin* **31**, 188-194, (2006).
- 7 Snyder, G. J. & Toberer, E. S. Complex thermoelectric materials. *Nat Mater* **7**, 105-114 (2008).
- 8 Tan, G. J., Zhao, L. D. & Kanatzidis, M. G. Rationally Designing High-Performance Bulk Thermoelectric Materials. *Chemical Reviews* **116**, 12123-12149 (2016).
- 9 Chung, D. Y. *et al.*  $\text{CsBi}_4\text{Te}_6$ : A high-performance thermoelectric material for low-temperature applications. *Science* **287**, 1024-1027 (2000).
- 10 Poudel, B. *et al.* High-thermoelectric performance of nanostructured bismuth antimony telluride bulk alloys. *Science* **320**, 634-638 (2008).
- 11 Hsu, K. F. *et al.* Cubic  $\text{AgPb}_m\text{SbTe}_{2+m}$ : Bulk thermoelectric materials with high

- figure of merit. *Science* **303**, 818-821 (2004).
- 12 Saramat, A. *et al.* Large thermoelectric figure of merit at high temperature in Czochralski-grown clathrate  $\text{Ba}_8\text{Ga}_{16}\text{Ge}_{30}$ . *J Appl Phys* **99**, 2163979 (2006).
- 13 Heremans, J. P. *et al.* Enhancement of thermoelectric efficiency in PbTe by distortion of the electronic density of states. *Science* **321**, 554-557 (2008).
- 14 Rhyee, J. S. *et al.* Peierls distortion as a route to high thermoelectric performance in  $\text{In}_4\text{Se}_3$ -delta crystals. *Nature* **459**, 965-968 (2009).
- 15 Wang, S. Y., Li, H., Lu, R. M., Zheng, G. & Tang, X. F. Metal nanoparticle decorated n-type  $\text{Bi}_2\text{Te}_3$ -based materials with enhanced thermoelectric performances. *Nanotechnology* **24**, 285702 (2013).
- 16 Shi, X. *et al.* Multiple-Filled Skutterudites: High Thermoelectric Figure of Merit through Separately Optimizing Electrical and Thermal Transports. *J Am Chem Soc* **133**, 7837-7846 (2011).
- 17 Zhao, H. Z. *et al.* High thermoelectric performance of MgAgSb-based materials. *Nano Energy* **7**, 97-103 (2014).
- 18 Kim, S. I. *et al.* Dense dislocation arrays embedded in grain boundaries for high-performance bulk thermoelectrics. *Science* **348**, 109-114 (2015).
- 19 Biswas, K. *et al.* High-performance bulk thermoelectrics with all-scale hierarchical architectures. *Nature* **489**, 414-418 (2012).
- 20 Rogl, G., Grytsiv, A., Bauer, E., Rogl, P. & Zehetbauer, M. Thermoelectric properties of novel skutterudites with didymium:  $\text{DDy}(\text{Fe}_{1-x}\text{Co}_x)_4\text{Sb}_{12}$  and  $\text{DDy}(\text{Fe}_{1-x}\text{Ni}_x)_4\text{Sb}_{12}$ . *Intermetallics* **18**, 57-64 (2010).
- 21 Liu, W. *et al.* Convergence of Conduction Bands as a Means of Enhancing Thermoelectric Performance of n-Type  $\text{Mg}_2\text{Si}_{1-x}\text{Sn}_x$  Solid Solutions. *Phys Rev Lett* **108**, 166601 (2012).
- 22 Liu, H. L. *et al.* Copper ion liquid-like thermoelectrics. *Nature Materials* **11**, 422-425 (2012).
- 23 Yamada, T., Yamane, H. & Nagai, H. A Thermoelectric Zintl Phase  $\text{Na}_{2+x}\text{Ga}_{2+x}\text{Sn}_{4-x}$  with Disordered Na Atoms in Helical Tunnels. *Adv Mater* **27**, 4708-4713 (2015).
- 24 Wu, D. *et al.* Origin of the High Performance in GeTe-Based Thermoelectric Materials upon  $\text{Bi}_2\text{Te}_3$  Doping. *J Am Chem Soc* **136**, 11412-11419 (2014).
- 25 Korkosz, R. J. *et al.* High ZT in p-Type  $(\text{PbTe})_{1-2x}(\text{PbSe})_x(\text{PbS})_x$  Thermoelectric Materials. *J Am Chem Soc* **136**, 3225-3237 (2014).
- 26 Zhao, L. D. *et al.* Raising the Thermoelectric Performance of p-Type PbS with Endotaxial Nanostructuring and Valence-Band Offset Engineering Using CdS and ZnS. *J Am Chem Soc* **134**, 16327-16336, (2012).

## 1. General Introduction

- 27 Zhao, L. D. *et al.* Ultralow thermal conductivity and high thermoelectric figure of merit in SnSe crystals. *Nature* **508**, 373 (2014).
- 28 He, Y. *et al.* High Thermoelectric Performance in Non-Toxic Earth-Abundant Copper Sulfide. *Adv Mater* **26**, 3974-3978 (2014).
- 29 Wu, D. *et al.* Superior thermoelectric performance in PbTe-PbS pseudo-binary: extremely low thermal conductivity and modulated carrier concentration. *Energ Environ Sci* **8**, 2056-2068 (2015).
- 30 Tan, G. J. *et al.* Codoping in SnTe: Enhancement of Thermoelectric Performance through Synergy of Resonance Levels and Band Convergence. *J Am Chem Soc* **137**, 5100-5112 (2015).
- 31 Lee, Y. *et al.* Contrasting role of antimony and bismuth dopants on the thermoelectric performance of lead selenide. *Nat Commun* **5**, 4640 (2014).
- 32 Biswas, K. *et al.* Strained endotaxial nanostructures with high thermoelectric figure of merit. *Nat Chem* **3**, 160-166 (2011).
- 33 Pei, Y. Z. *et al.* Convergence of electronic bands for high performance bulk thermoelectrics. *Nature* **473**, 66-69 (2011).
- 34 Chang, C. *et al.* 3D charge and 2D phonon transports leading to high out-of-plane ZT in n-type SnSe crystals. *Science* **360**, 778-782 (2018).
- 35 Koumoto, K., Terasaki, I. & Funahashi, R. Complex oxide materials for potential thermoelectric applications. *MRS Bull.* **31**, 206-210 (2006).
- 36 Koumoto, K., Wang, Y. F., Zhang, R. Z., Kosuga, A. & Funahashi, R. Oxide 'Thermoelectric Materials: A Nanostructuring Approach. *Annu Rev Mater Res* **40**, 363-394 (2010).
- 37 Koumoto, K. *et al.* Thermoelectric Ceramics for Energy Harvesting. *J Am Ceram Soc* **96**, 1-23 (2013).
- 38 Hogarth, C. CA Hogarth and JP Andrews, *Phil. Mag.* **40**, 273 (1949). *Phil. Mag.* **40**, 273 (1949).
- 39 Parravano, G. Thermoelectric behavior of nickel oxide. *The Journal of Chemical Physics* **23**, 5-10 (1955).
- 40 Hutson, A. Electronic properties of ZnO. *Journal of Physics and Chemistry of Solids* **8**, 467-472 (1959).
- 41 Arvin, M. Electrical conductivity and thermoelectric power of indium oxide. *Phys. Chem. Solids* **23** (1962).
- 42 Frederikse, H., Thurber, W. & Hosler, W. Electronic transport in strontium titanate. *Physical Review* **134**, A442 (1964).
- 43 Thurber, W. & Mante, A. Thermal Conductivity and Thermoelectric Power of

## 1. General Introduction

- Rutile (Ti O 2). *Physical Review* **139**, A1655 (1965).
- 44 Marley, J. & Dockerty, R. Electrical properties of stannic oxide single crystals. *Physical Review* **140**, A304 (1965).
- 45 Young, A. & Schwartz, C. Electrical conductivity and thermoelectric power of Cu<sub>2</sub>O. *Journal of Physics and Chemistry of Solids* **30**, 249-252 (1969).
- 46 Griffiths, B., Elwell, D. & Parker, R. The thermoelectric power of the system NiFe<sub>204</sub>-Fe<sub>304</sub>. *Philosophical Magazine* **22**, 163-174 (1970).
- 47 Bednorz, J. G. & Müller, K. A. Possible highT c superconductivity in the Ba– La– Cu–O system. *Zeitschrift für Physik B Condensed Matter* **64**, 189-193 (1986).
- 48 Cooper, J., Alavi, B., Zhou, L., Beyermann, W. & Grüner, G. Thermoelectric power of some high-T c oxides. *Phys Rev B* **35**, 8794 (1987).
- 49 Chen, J., McEwan, C., Wenger, L. & Logothetis, E. Determination of charge carriers in superconducting La-Ba-Cu-O by thermoelectric measurements. *Phys Rev B* **35**, 7124 (1987).
- 50 Mitra, N. *et al.* Thermoelectric power of the Tl-Ca-Ba-Cu-O superconductor. *Phys Rev B* **38**, 7064 (1988).
- 51 Ohtaki, M., Koga, H., Tokunaga, T., Eguchi, K. & Arai, H. Electrical transport properties and high-temperature thermoelectric performance of (Ca<sub>0.9</sub>M<sub>0.1</sub>) MnO<sub>3</sub> (M= Y, La, Ce, Sm, In, Sn, Sb, Pb, Bi). *J Solid State Chem* **120**, 105-111 (1995).
- 52 Ohtaki, M., Tsubota, T., Eguchi, K. & Arai, H. High-temperature thermoelectric properties of (Zn<sub>1-x</sub>Al<sub>x</sub>) O. *J Appl Phys* **79**, 1816-1818 (1996).
- 53 Terasaki, I., Sasago, Y. & Uchinokura, K. Large thermoelectric power in NaCo<sub>2</sub>O<sub>4</sub> single crystals. *Phys Rev B* **56**, 12685-12687 (1997).
- 54 Masset, A. *et al.* Misfit-layered cobaltite with an anisotropic giant magnetoresistance: Ca<sub>3</sub>Co<sub>4</sub>O<sub>9</sub>. *Phys Rev B* **62**, 166 (2000).
- 55 Funahashi, R. *et al.* An oxide single crystal with high thermoelectric performance in air. *Japanese Journal of Applied Physics* **39**, L1127 (2000).
- 56 Okuda, T., Nakanishi, K., Miyasaka, S. & Tokura, Y. Large thermoelectric response of metallic perovskites: Sr<sub>1-x</sub>La<sub>x</sub>TiO<sub>3</sub> (0 < x < 0. 1). *Phys Rev B* **63**, 113104 (2001).
- 57 Ohta, S., Nomura, T., Ohta, H. & Koumoto, K. High-temperature carrier transport and thermoelectric properties of heavily La-or Nb-doped SrTiO<sub>3</sub> single crystals. *J Appl Phys* **97**, 034106 (2005).
- 58 Ohta, S. *et al.* Large thermoelectric performance of heavily Nb-doped SrTiO<sub>3</sub> epitaxial film at high temperature. *Appl Phys Lett* **87**, 092108 (2005).
- 59 Funahashi, R. *et al.* An oxide single crystal with high thermoelectric performance

## 1. General Introduction

- in air. *Jpn J Appl Phys* 2 **39**, L1127-L1129 (2000).
- 60 Koshibae, W., Tsutsui, K. & Maekawa, S. Thermopower in cobalt oxides. *Phys Rev B* **62**, 6869-6872 (2000).
- 61 Slack, G. A. New materials and performance limits for thermoelectric cooling. *CRC handbook of thermoelectrics*, 407-440 (1995).
- 62 Fergus, J. W. Oxide materials for high temperature thermoelectric energy conversion. *J Eur Ceram Soc* **32**, 525-540 (2012).
- 63 Jonker, G. & Van Santen, J. *Physica (Utrecht)* 16, 337 (1950). *CrossRef Google Scholar* (1950).
- 64 Wollan, E. EO Wollan and WC Koehler, *Phys. Rev.* 100, 545 (1955). *Phys. Rev.* **100**, 545 (1955).
- 65 Goodenough, J. B. JB Goodenough, *Phys. Rev.* 100, 564 (1955). *Phys. Rev.* **100**, 564 (1955).
- 66 MacChesney, J., Williams, H., Potter, J. & Sherwood, R. Magnetic Study of the Manganate Phases:  $\text{CaMnO}_3$ ,  $\text{Ca}_4\text{Mn}_3\text{O}_{10}$ ,  $\text{Ca}_3\text{Mn}_2\text{O}_7$ ,  $\text{Ca}_2\text{MnO}_4$ . *Physical Review* **164**, 779 (1967).
- 67 Wang, Y. *et al.* High Temperature Thermoelectric Response of Electron-Doped  $\text{CaMnO}_3$ . *Chem Mater* **21**, 4653-4660 (2009).
- 68 Funahashi, R. *et al.* in *Thermoelectrics, 2007. ICT 2007. 26th International Conference on*. 124-128 (IEEE).
- 69 Park, K., Seong, J. & Kim, G. NiO added  $\text{Zn}_{1-x}\text{Ni}_x\text{O}$  ( $0 \leq x \leq 0.05$ ) for thermoelectric power generation. *Journal of Alloys and Compounds* **473**, 423-427 (2009).
- 70 Park, K. & Ko, K. Y. Effect of  $\text{TiO}_2$  on high-temperature thermoelectric properties of ZnO. *Journal of Alloys and Compounds* **430**, 200-204 (2007).
- 71 Park, K. & Seong, J. Influence of simultaneous addition of  $\text{Sb}_2\text{O}_3$  and  $\text{SnO}_2$  on thermoelectric properties of  $\text{Zn}_{1-x-y}\text{Sb}_x\text{Sn}_y\text{O}$  prepared by tape casting. *Journal of Alloys and Compounds* **464**, 1-5 (2008).
- 72 Park, K., Seong, J. & Nahm, S. Improvement of thermoelectric properties with the addition of Sb to ZnO. *Journal of Alloys and Compounds* **455**, 331-335 (2008).
- 73 Mattheiss, L. Energy Bands for  $\text{KNiF}_3$ ,  $\text{SrTiO}_3$ ,  $\text{KMoO}_3$ , and  $\text{KTaO}_3$ . *Phys Rev B* **6**, 4718 (1972).
- 74 Hicks, L. D. & Dresselhaus, M. S. Effect of quantum-well structures on the thermoelectric figure of merit. *Phys Rev B* **47**, 12727-12731 (1993).
- 75 Dresselhaus, M. S. *et al.* New directions for low-dimensional thermoelectric materials. *Adv Mater* **19**, 1043-1053 (2007).

## 1. General Introduction

- 76 Hicks, L. D., Harman, T. C., Sun, X. & Dresselhaus, M. S. Experimental study of the effect of quantum-well structures on the thermoelectric figure of merit. *Phys Rev B* **53**, 10493-10496 (1996).
- 77 Hicks, L. D. & Dresselhaus, M. S. Thermoelectric Figure of Merit of a One-Dimensional Conductor. *Phys Rev B* **47**, 16631-16634 (1993).
- 78 Ohta, H. *et al.* Giant thermoelectric Seebeck coefficient of two-dimensional electron gas in SrTiO<sub>3</sub>. *Nature Materials* **6**, 129-134 (2007).
- 79 Ohtomo, A. & Hwang, H. A high-mobility electron gas at the LaAlO<sub>3</sub>/SrTiO<sub>3</sub> heterointerface. *Nature* **427**, 423 (2004).
- 80 Pallecchi, I. *et al.* Large phonon-drag enhancement induced by narrow quantum confinement at the LaAlO<sub>3</sub>/SrTiO<sub>3</sub> interface. *Phys Rev B* **93**, 195309 (2016).
- 81 Ohta, H. *et al.* Unusually Large Enhancement of Thermopower in an Electric Field Induced Two-Dimensional Electron Gas. *Adv Mater* **24**, 740-744 (2012).
- 82 Zhang, Y. Q. *et al.* Thermoelectric phase diagram of the SrTiO<sub>3</sub>-SrNbO<sub>3</sub> solid solution system. *J Appl Phys* **121**, 185102 (2017).
- 83 Zhang, Y. Q. *et al.* Double thermoelectric power factor of a 2D electron system. *Nat Commun* **9**, 2224 (2018).

## 2. **Experimental Methods**

### 2.1 **Synthesis method of thermoelectric materials**

Recently, most of the popular thermoelectric materials are fabricated in forms of bulk materials like polycrystalline ceramics and single crystalline ingots. In bulk materials, hot processing and spark plasma sintering (SPS) are usually used to synthesize polycrystalline specimens, whereas Bridgman crystal growth, zone melting, Czochralski process, etc. are usually used for growing single crystals. With the developments in film growth technologies, 2D materials are attracting increasing attentions due to their unique performances at quantum size scales. For the growth of high quality epitaxial films, molecular beam epitaxy (MBE) and pulsed laser deposition (PLD) are among the most popular fabrication techniques.

#### 2.1.1 **Bulk ceramic synthesis**

In thermoelectrics, polycrystalline ceramics are the most commonly used due to the low fabrication cost and simple fabrication process. By controlling grain size and boundary density, the thermal conductivity by polycrystalline ceramics can be effectively optimized.

Hot pressing method is the most traditional synthesis technique for bulk ceramic fabrication. As shown in [Fig. 2.1\(a\)](#), raw powders are sealed into a mould, which is usually made of graphite. During the sintering process, high temperature and high pressure are exerted on both side of the specimen, ensuring highly dense specimens with

low porosity. However, as this process takes place at extreme environments (high temperature + high pressure), the synthesis usually long and it is difficult to obtain samples with small grains.

In order to overcome these disadvantages, researchers looked into the spark plasma sintering (SPS). In contrast to the hot pressing, heating modules of SPS are changed to self-heating of specimen by introducing a large DC current (1–10 kA). As show in Fig. 2.1(b), along the pressure direction, a high DC power is applied, which can induce a large amount of Joule heating within a short time (the maximum heating rate can reach to 1000 K min<sup>-1</sup>). As sintering time is short, most of micro/nano morphologies of raw powers could be conserved into bulk states. Therefore, through SPS technique, bulk materials with very fine grains and textures can be prepared. This is very meaningful for thermoelectric materials design, especially for nano-textured bulk materials.

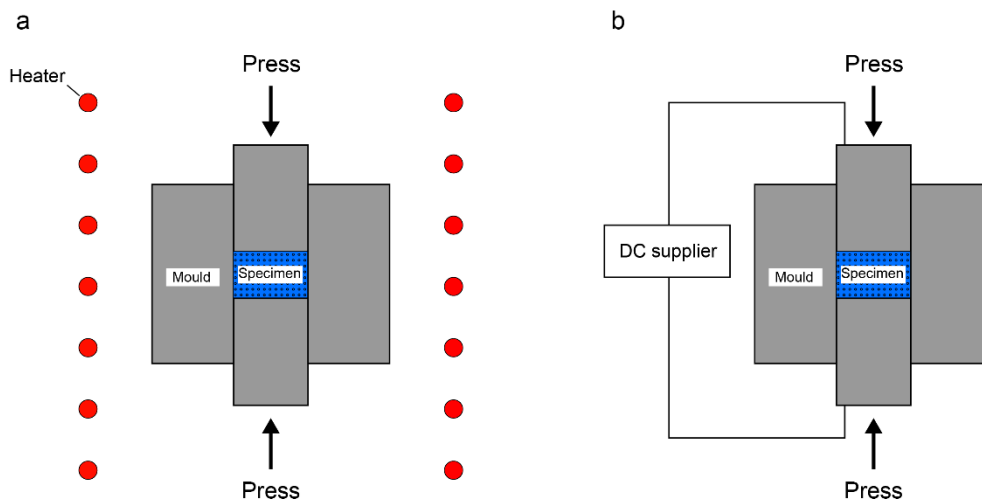


**Figure 2.1.** Schematic illustrations of (a) pressing sintering and (b) spark plasma sintering.

### 2.1.2 Bulk single crystal synthesis

## 2. Experimental Methods

Single crystal based bulk materials are also important in thermoelectrics. Macro-scale single crystalline bulks have perfect lattice structures, which can remove effects from grain boundaries and other defects. Therefore, they are essential for clarifying intrinsic properties of materials. Many single crystalline thermoelectric materials with good performances have been developed. For example, La/Nb doped SrTiO<sub>3</sub> single crystals show very high PF at room temperature, which is attributed to the high electron transport property of single crystal phase<sup>1,2</sup>. In addition, a record high  $ZT$  value was achieved in single crystalline SnSe<sup>3,4</sup>. However, the growth of bulk single crystals is a very difficult and time-consuming. Therefore, cost-effective single crystal fabrications are always of great interest in the community. Nowadays, the most famous single crystal synthesis methods include Czochralski process, Verneuil method, Bridgman–Stockbarger technique, and more.

Czochralski process was firstly developed by Jan Czochralski in 1916, which is now widely used for producing silicon ingots in modern semiconductor devices<sup>5</sup>. As shown in [Fig. 2.2](#), during the growth of Si ingots, polycrystalline Si is first melted and doped with specific elements to make Si into n- or p-type. Then a precisely oriented rod-mounted seed crystal is dipped into the molten silicon. The seed crystal rod is slowly pulled upwards and rotated simultaneously. By precisely controlling the temperature gradients, rate of pulling and speed of rotation, it is possible to extract a large single-crystal cylindrical ingot from the melt. Currently, many high performance thermoelectric materials such as Ba<sub>8</sub>Ga<sub>16</sub>Ge<sub>30</sub><sup>6</sup> and SiGe alloy<sup>7</sup>, which is promising for application at high temperature, are fabricated by Czochralski process.

## 2. Experimental Methods

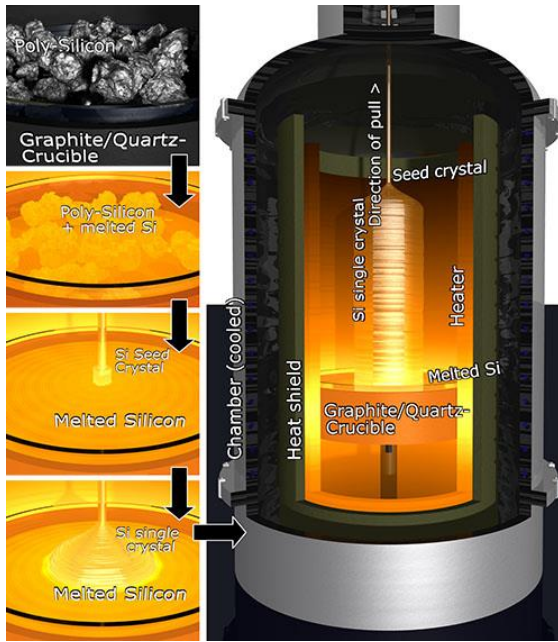


**Figure 2.2.** Schematic illustration of Czochralski process.

The Verneuil method, also called flame fusion, was firstly developed by Auguste Verneuil in 1902 to manufacture artificial gemstones. This method is still widely used for the synthesis of single crystal  $\text{Al}_2\text{O}_3$  and  $\text{SrTiO}_3$  substrates. As shown in Fig. 2.3, this process involves melting a finely powdered substance using an oxyhydrogen flame and crystallizing the melted droplets into a boule. The Verneuil method is considered to be the founding step of the modern industrial crystal growth technology. In 2005, Ohta *et al.* used La and Nb doped  $\text{SrTiO}_3$  single crystals prepared by Verneuil method and clarified their thermoelectric properties at high temperatures<sup>1</sup>.

## 2. Experimental Methods

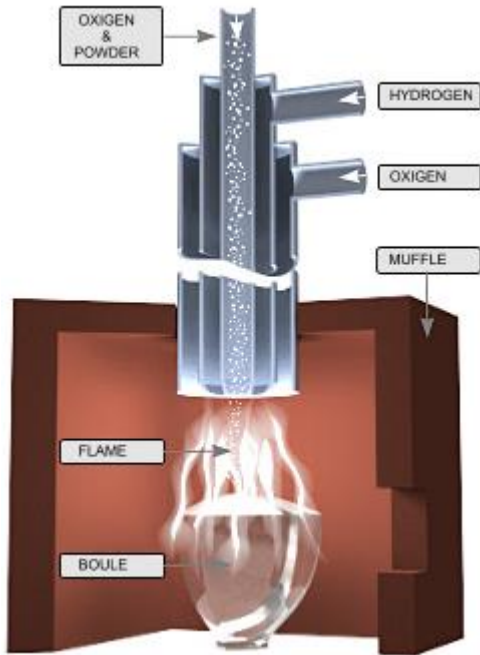


**Figure 2.3.** Schematic illustration of Verneuil technique.

Another single crystal synthesis method is Bridgman-Stockbarger method, which is proposed by Percy Williams Bridgman and Donald C. Stockbarger. As shown in [Fig. 2.4](#), in the Bridgman-Stockbarger method, raw powders were mixed and sealed into ampoules. By heating, the raw powder will be melted into liquid phase. At one end of the ampoule, a seed crystal is attached. With the other end of the ampoule slowly cooling down, the liquid mixture will crystallize around the seed crystal into a single crystal ingot. The Bridgman-Stockbarger method is usually used to produce semiconductor single crystals such as SiAs, SnAs, CsMnBr, AuTe<sub>2</sub>, etc., and the SnSe single crystals which exert record high  $ZT$  values were also synthesized by this method<sup>4,8</sup>.

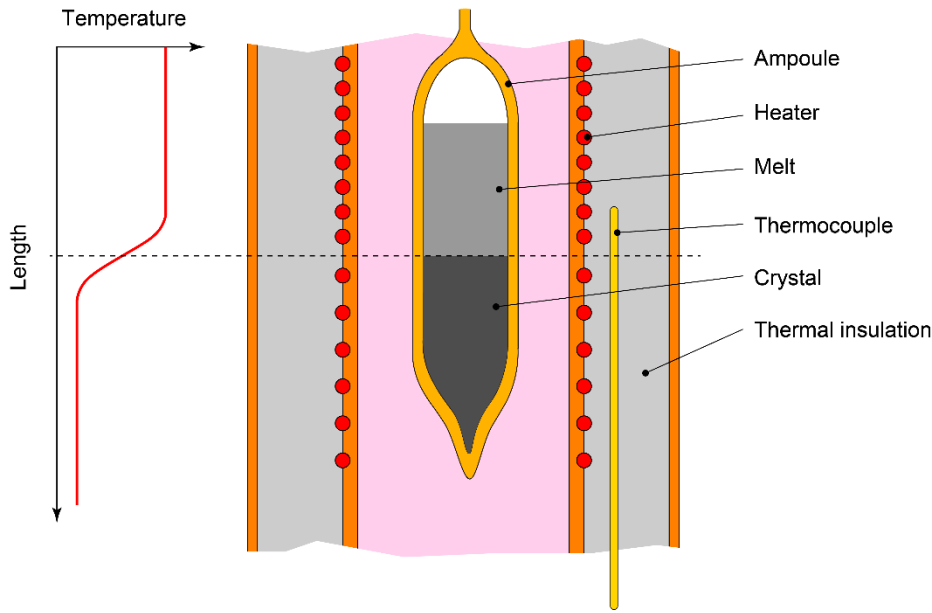


**Figure 2.4.** Schematic illustration of Bridgman-Stockbarger method.

### 2.1.3 Epitaxial films

Although the fabrication technologies of bulk thermoelectrics have been extensively examined, they are not perfect sample fabrication processes in all aspects. For example, to fulfil the objectives of this study, we need to prepare a full range of  $\text{SrTiO}_3\text{-SrNbO}_3$  solid solutions. However, due to the solubility limit of  $\text{Nb}^{5+}$  in  $\text{SrTiO}_3$ , it is almost impossible to synthesize uniform bulk ceramics or single crystals of  $\text{SrTi}_{1-x}\text{Nb}_x\text{O}_3$  at  $x > 0.2^9$ . An effective way to solve this problem is film fabrication, especially since epitaxial films have electron transport properties closed to the bulk single crystals. Nowadays, the most popular film epitaxy methods are MBE and PLD.

MBE, which stands for molecular beam epitaxy, is an ultra-high vacuum ( $< 10^{-8}$  Pa) film fabrication technique, which is widely used in fabrications of single crystalline epitaxial films and transistors. It was firstly invented by K. G. Günther in 1958 and

## 2. Experimental Methods

improved by J. R. Arthur and Alfred Y. Cho in the late 1960s<sup>10,11</sup>. As shown in Fig. 2.5, in a typical MBE facility, ultra-high pure elements constituting the targeting films are heated in effusion cells and sublimed onto the substrate where they can react with each other into the targeting films. Usually the deposition rate is controlled at very low level, which allows a high quality layer by layer epitaxial growth. If the MBE is equipped with reflection high-energy electron diffraction (RHEED) system, in-situ deposition status of films can be observed. By adjusting the atomic float rate of each material source, one can precisely control the composition of targeting films. Special atmosphere such as oxygen can also be introduced during the deposition. MBE is widely used in fabrication of high quality oxide based films, including  $\text{BaSnO}_3$  and  $\text{SrTiO}_3$ .

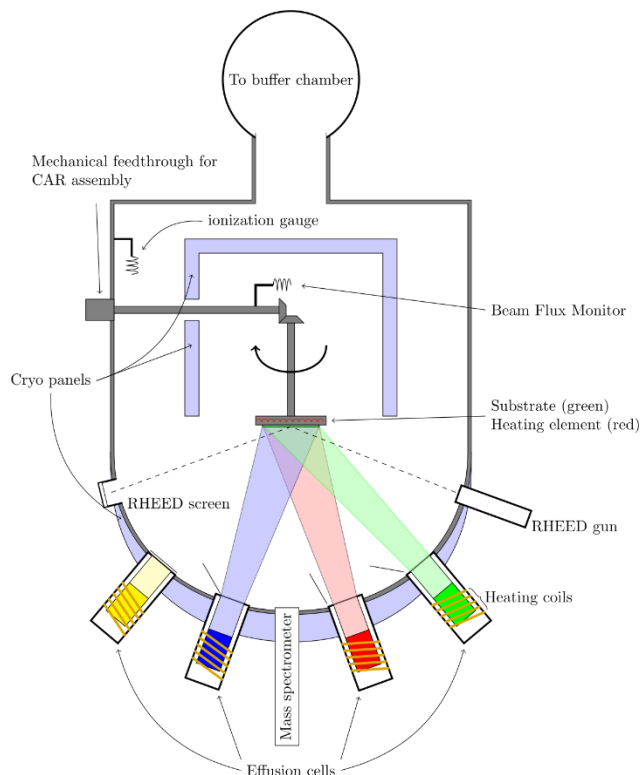


**Figure 2.5.** Schematic illustration of molecular beam epitaxy (MBE).

## 2. Experimental Methods

PLD, which stands for pulsed laser deposition, is another technique widely used in epitaxial growth of films. As shown in Fig. 2.6, PLD is composed of an excimer laser and a high-vacuum film growth chamber. During the deposition, high power pulsed laser will be directed by mirrors and ablate the surface of targets. Ablation will excite plasma plume with highly energetic ions, electrons as well as neutral atoms, which will be deposited on the heated substrate and form the film. The details on the PLD method are very complex, but it can generally be simplified into two stages: (1) laser ablation of target surface and creation of a plasma plume; (2) Film growth on the substrate. During the irradiation of laser, the surface part of target will be heated up and vaporized. The plasma will move towards the substrate due to Coulomb repulsion and recoil from the target surface. The shape and color of plume is dependent on laser power, ablation area and background pressure. By controlling these parameters, one can control the stoichiometric ratio during the vaporization. After vaporization, ions from the target will be accumulated on the surface of substrates. At the same time, ions striking the substrate with high energy can also sputter off atoms from the substrate surface. However, as the condensation rate is sufficiently high, film growth will occur on the substrate surface. The quality, composition, and phase of the film are strongly related to the deposition parameters mentioned above, and various types of films including amorphous, single crystals, and even nonstoichiometry can be achieved. In contrast to MBE, the targets used in PLD can be prepared easily. Even though the quality of films prepared by PLD sometimes is lower than those prepared by MBE, due to the low cost and easy maintenances, PLD is widely used by researchers all around the world.

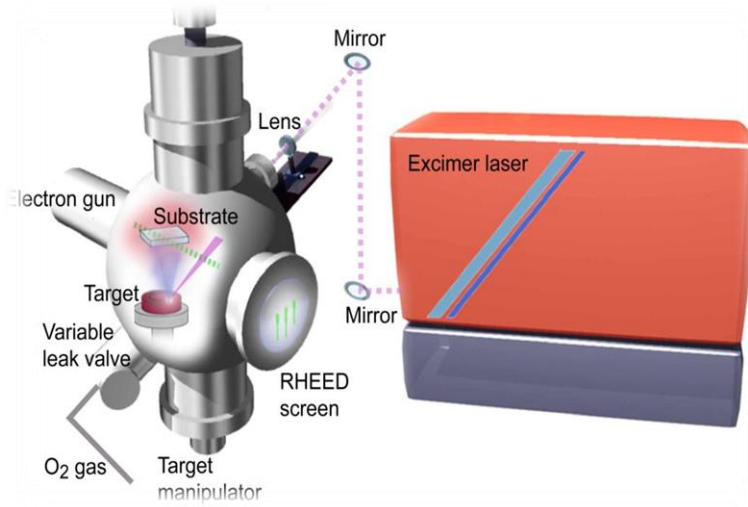


**Figure 2.6.** Schematic illustration of pulsed laser deposition (PLD) system.

In this study, PLD equipped with RHEED was used to fabricate  $\text{SrTiO}_3\text{-SrNbO}_3$  solid solution films and artificial superlattices. By precisely controlling of deposition conditions, high quality epitaxial films and superlattices were successfully prepared on (001) surface of  $\text{LaAlO}_3$  single crystalline substrates. As shown in Fig. 2.7, during the deposition RHEED oscillation diagram can be used to check the coverage of every unit cell of films, which was utilized for in-situ film quality and growth rate controls<sup>12,13</sup>.

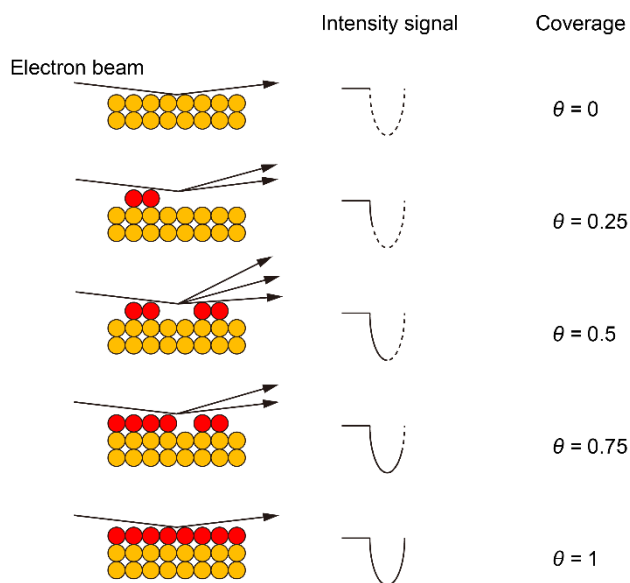


**Figure 2.7.** RHEED intensity oscillation and control of layer coverage.

## 2.2 Structure characterizations

The crystal structures of films are characterized by high-resolution X-ray diffraction (HRXRD) and scanning transmission electron microscope (STEM). The HRXRD was used to check the thickness and rough information on crystallinity while the STEM was used to reveal the local microstructures with a high resolution.

In HRXRD, the X-ray reflectometry (XRR) was used to measure the thickness and density of as-prepared films, which is based on oscillation pattern from the interference of the reflected beam at the interface and surface. **Fig. 2.8(a)** shows XRR pattern of Nb doped SrTiO<sub>3</sub> film on (001) LaAlO<sub>3</sub> single crystal substrate. The XRD scan range was 0.3-3°. Due to the density difference in film and substrate, the incident X-ray beam was reflected at film/substrate interface and interfere with the reflected beam at film surface. For this reason, the XRR contains the information of film thickness and density. **Fig.**

2.8(b) shows the out-of-plane patterns of Nb doped SrTiO<sub>3</sub> film, which is used to confirm epitaxial film growths on the substrates. Similar to XRR, the interference fringes originating from the thickness oscillation can be observed, which indicates a flat interface and surface. In out-of-plane XRD pattern, the film orientation can be confirmed. The (002) peaks of the film and substrate were detected, which suggests an epitaxial growth along the c-axis. In Fig. 2.8(b), the reciprocal space mapping (RSM) is presented, where the x-axis and y-axis of the plot correspond to the c-axis and a-axis of the film, respectively. Therefore, we can obtain both the in-plane and out-of-plane lattice characteristics of the film, and our films show incoherent growth on LaAlO<sub>3</sub> substrate, which indicates strain-free film behaviors.

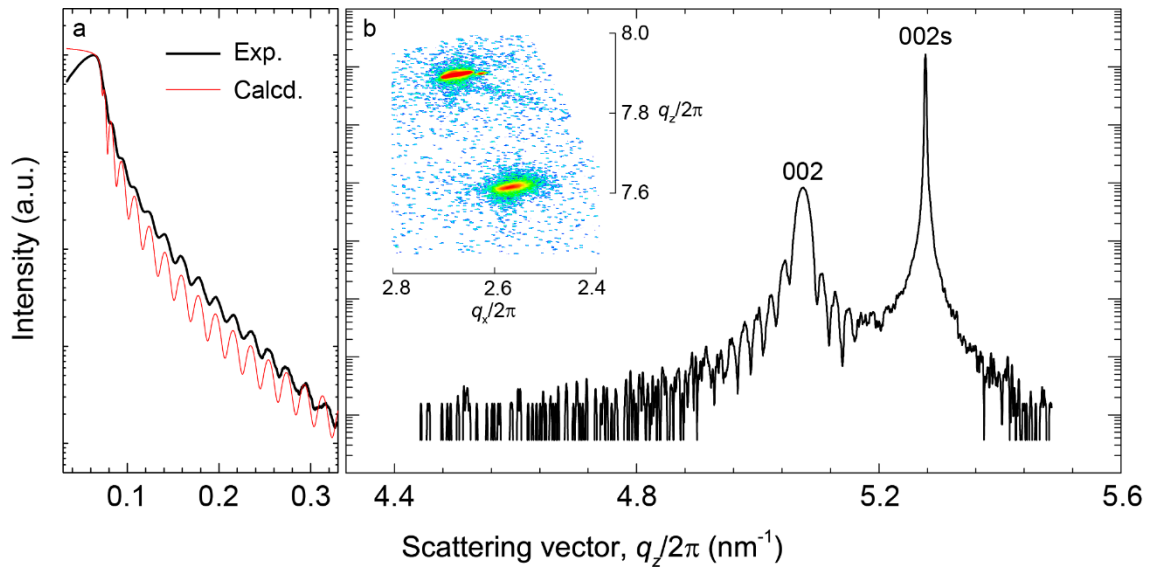


**Figure 2.8.** (a) X-ray reflectometry (XRR) and (b) out-of-plane XRD pattern for Nb doped SrTiO<sub>3</sub> film. Inset of (b) shows the reciprocal space mapping (RSM) image of (-103) diffraction spot of Nb doped SrTiO<sub>3</sub> film.

From the STEM micrographs, we can directly observe the microstructure of samples

## 2. Experimental Methods

in an atomic scale. STEM is a special type of conventional TEM, which observes fine atomic scale features using an electron beam passing through very thin samples (< 100 nm). In case of STEM, the electron beam focused on the specimen is also scanned over the specimen. The atoms in the specimen could be detected with different contrast depending on the atomic number (Z-value). As shown in Fig. 2.9(a), the STEM observation has two modes, which are annular dark-field (ADF) mode and annular bright-field (ABF) mode. For ADF mode, the contrast is directly related to atomic number, where heavy atoms can be easily distinguished. ABF mode is more sensitive to the light elements such as oxygens. STEM also has an important characterization method known as the electron energy loss spectroscopy (EELS). As the electron beam transmit through the sample, due to the inelastic scattering of the electrons by the ions in the sample, the electrons in the beam will lose some energy, which could be measured by an electron spectrometer. Using the EELS spectra, elemental ionization edges can be identified, allowing us to confirm the valence state of elements in the samples. As shown in Fig. 2.9(b), Ohta *et al.* used EELS to check the Ti valence state in SrTi<sub>0.8</sub>Nb<sub>0.2</sub>O<sub>3</sub>|SrTiO<sub>3</sub> quantum well structures, where a good confinement of Nb doping in the effective layers was confirmed. This study also used EELS to observe the valence state of Ti and Nb atoms in SrTi<sub>1-x</sub>Nb<sub>x</sub>O<sub>3</sub> thin films and artificial superlattices.

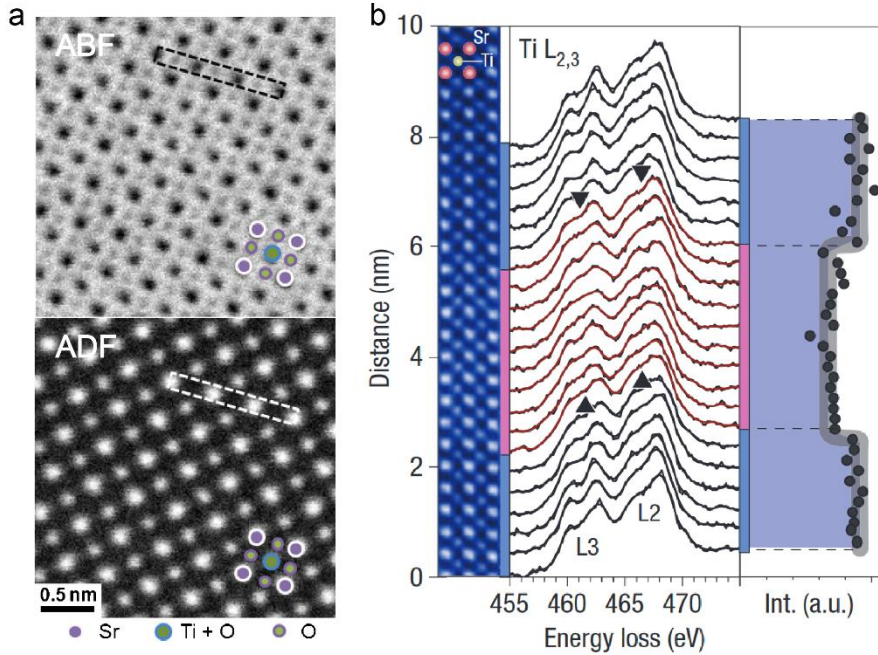


**Figure 2.9.** (a) Annular dark-field (ABF) and annular bright-field (ADF) images of  $\text{SrTiO}_3$ . In ABF image, oxygen with low atomic number can be observed<sup>14</sup>. (b) (left to right) High-resolution HAADF-STEM image, Ti-L<sub>2,3</sub> edge EELS profile, and integrated intensity profile of the Ti-L<sub>2,3</sub> edge EELS across a  $\text{SrTiO}_3/\text{SrTi}_{0.8}\text{Nb}_{0.2}\text{O}_3/\text{SrTiO}_3$  quantum well. Ti in the  $\text{SrTi}_{0.8}\text{Nb}_{0.2}\text{O}_3$  layer exhibits a +3/+4 mixed valence state<sup>15</sup>.

### 2.3 Band calculations

To validate the experimental results with theory, *ab-initio* electronic band structure calculation was performed for both  $\text{SrTi}_{1-x}\text{Nb}_x\text{O}_3$  ( $x = 0, 0.25, 0.5, 0.75$  and  $1$ ) full range solid solutions and  $[1 \text{ uc SrNbO}_3|10 \text{ uc SrTiO}_3]$  superlattice. The band structure was calculated using density functional theory (DFT) based on the projector augmented-wave (PAW) method,<sup>16</sup> using VASP code<sup>17,18</sup>. We adopted the Heyd–Scuseria–Ernzerhof hybrid functionals<sup>19-21</sup> and a plane-wave cutoff energy of 550 eV.

## 2. Experimental Methods

For the  $\text{SrTi}_{1-x}\text{Nb}_x\text{O}_3$  solid solutions, a  $6\times 6\times 6$   $k$ -point mesh was employed in the total-energy evaluation and geometry optimization for the unit cells. In case of  $\text{SrTiO}_3$  and  $\text{SrNbO}_3$  cubic-perovskite were implemented while special quasi-random structures (SQSs) were used in the case of  $\text{SrTi}_{1-x}\text{Nb}_x\text{O}_3$  ( $x = 0.25, 0.5, \text{ and } 0.75$ ). The SQSs with eight Sr or Ti sites were constructed by optimizing the correlation functions of seven types of independent pairs using the CLUPAN code<sup>22,23</sup>.

For [1 uc  $\text{SrNbO}_3$ |10 uc  $\text{SrTiO}_3$ ] superlattice,  $6\times 6\times 6$  and  $6\times 6\times 2$   $k$ -point meshes were employed in the total-energy evaluations and geometry optimization for the perovskite unit cells of  $\text{SrTiO}_3$  and the superlattice cell, respectively. The in-plane lattice constant of the superlattice cell was fixed at the optimized value of  $\text{SrTiO}_3$  while the out-of-plane lattice constant and the atomic coordinates were fully relaxed.

## References

- 1 Ohta, S., Nomura, T., Ohta, H. & Koumoto, K. High-temperature carrier transport and thermoelectric properties of heavily La-or Nb-doped  $\text{SrTiO}_3$  single crystals. *J Appl Phys* **97**, 034106 (2005).
- 2 Okuda, T., Nakanishi, K., Miyasaka, S. & Tokura, Y. Large thermoelectric response of metallic perovskites:  $\text{Sr}_{1-x}\text{La}_x\text{TiO}_3$  ( $0 < x < 0.1$ ). *Phys Rev B* **63**, 113104 (2001).
- 3 Zhao, L. D. *et al.* Ultralow thermal conductivity and high thermoelectric figure of merit in SnSe crystals. *Nature* **508**, 373 (2014).
- 4 Chang, C. *et al.* 3D charge and 2D phonon transports leading to high out-of-plane ZT in n-type SnSe crystals. *Science* **360**, 778-782 (2018).
- 5 Tomaszewski, P. E. Jan Czochralski—father of the Czochralski method. *Journal of Crystal Growth* **236**, 1-4 (2002).
- 6 Saramat, A. *et al.* Large thermoelectric figure of merit at high temperature in Czochralski-grown clathrate  $\text{Ba}_8\text{Ga}_{16}\text{Ge}_{30}$ . *J Appl Phys* **99**, 2163979 (2006).
- 7 Yonenaga, I. Czochralski growth of heavily impurity doped crystals of GeSi alloys.

- Journal of Crystal Growth* **226**, 47-51 (2001).
- 8 Zhao, L. D. *et al.* Raising the Thermoelectric Performance of p-Type PbS with Endotaxial Nanostructuring and Valence-Band Offset Engineering Using CdS and ZnS. *J Am Chem Soc* **134**, 16327-16333 (2012).
- 9 Rodenbacher, C. *et al.* Homogeneity and variation of donor doping in Verneuil-grown SrTiO<sub>3</sub>:Nb single crystals. *Sci Rep-Uk* **6** (2016).
- 10 Günther, K. Aufdampfschichten aus halbleitenden III-V-Verbindungen. *Zeitschrift für Naturforschung A* **13**, 1081-1089 (1958).
- 11 Cho, A. Y. & Arthur, J. Molecular beam epitaxy. *Progress in solid state chemistry* **10**, 157-191 (1975).
- 12 Zhang, Y. Q. *et al.* Double thermoelectric power factor of a 2D electron system. *Nat Commun* **9**, 2224 (2018).
- 13 Zhang, Y. Q. *et al.* Thermoelectric phase diagram of the SrTiO<sub>3</sub>-SrNbO<sub>3</sub> solid solution system. *J Appl Phys* **121**, 185102 (2017).
- 14 Okunishi, E., Sawada, H. & Kondo, Y. Experimental study of annular bright field (ABF) imaging using aberration-corrected scanning transmission electron microscopy (STEM). *Micron* **43**, 538-544 (2012).
- 15 Ohta, H. *et al.* Giant thermoelectric Seebeck coefficient of two-dimensional electron gas in SrTiO<sub>3</sub>. *Nature Materials* **6**, 129-134 (2007).
- 16 Blochl, P. E. Projector Augmented-Wave Method. *Phys Rev B* **50**, 17953-17979 (1994).
- 17 Kresse, G. & Joubert, D. From ultrasoft pseudopotentials to the projector augmented-wave method. *Phys Rev B* **59**, 1758-1775 (1999).
- 18 Kresse, G. & Furthmüller, J. Efficient iterative schemes for ab initio total-energy calculations using a plane-wave basis set. *Phys Rev B* **54**, 11169-11186 (1996).
- 19 Heyd, J., Scuseria, G. E. & Ernzerhof, M. Hybrid functionals based on a screened Coulomb potential (vol 118, pg 8207, 2003). *J Chem Phys* **124**, 2204597 (2006).
- 20 Krukau, A. V., Vydrov, O. A., Izmaylov, A. F. & Scuseria, G. E. Influence of the exchange screening parameter on the performance of screened hybrid functionals. *J Chem Phys* **125** (2006).
- 21 Heyd, J., Scuseria, G. E. & Ernzerhof, M. Hybrid functionals based on a screened Coulomb potential. *J Chem Phys* **118**, 8207-8215 (2003).
- 22 Seko, A., Koyama, Y. & Tanaka, I. Cluster expansion method for multicomponent systems based on optimal selection of structures for density-functional theory calculations. *Phys. Rev. B* **80**, 165122 (2009).
- 23 Seko, A. *clupan*, <<http://sourceforge.net/projects/clupan>> (2007).

## 2. *Experimental Methods*

### 3. Thermoelectric phase diagram of the SrTiO<sub>3</sub>–SrNbO<sub>3</sub> solid solution system

#### 3.1 Introduction

Thermoelectric energy conversion, in which waste heat is transformed into electricity by the Seebeck effect, is attracting significant research attention as a potential energy harvesting technology<sup>1,2</sup>. Generally, the performance of thermoelectric materials is evaluated in terms of a dimensionless figure of merit,  $ZT = S^2 \cdot \sigma \cdot T \cdot \kappa^{-1}$ , where  $ZT$  is the figure of merit,  $S$  is the thermopower (Seebeck coefficient),  $\sigma$  is the electrical conductivity,  $\kappa$  is the thermal conductivity, and  $T$  is the absolute temperature. Although the  $ZT$  values of several commercialized thermoelectric materials such as Bi<sub>2</sub>Te<sub>3</sub> ( $ZT \sim 1$  @400 K) and PbTe ( $ZT \sim 0.8$  @600 K) are roughly 1<sup>3,4</sup>, these heavy metal–based materials present environmental risks due to the toxicity of their constituent elements and their chemical and thermal instability. Recently, transition metal oxides (TMOs) including Na<sub>x</sub>CoO<sub>2</sub> ( $x \sim 0.75$ )<sup>5,6</sup>, Ca<sub>3</sub>Co<sub>4</sub>O<sub>9</sub><sup>7,8</sup>, and SrTiO<sub>3</sub><sup>9-11</sup> have drawn a high volume of research as high-temperature thermoelectric power generation materials: this group of materials are considered to be particularly suitable for these applications due to their chemical and thermal robustness, as well as their comparatively low environmental risk<sup>12</sup>.

Among the available TMOs, electron-doped SrTiO<sub>3</sub> has been one of the most extensively studied materials for thermoelectric applications<sup>13,14</sup>. In 2001, Okuda *et al.*<sup>9</sup> synthesized Sr<sub>1-x</sub>La<sub>x</sub>TiO<sub>3</sub> ( $0 \leq x \leq 0.1$ ) single crystals by the floating-zone method, and reported that they yielded a large power factor ( $S^2 \cdot \sigma$ ) of 2.8–3.6 mW m<sup>-1</sup> K<sup>-2</sup> at room temperature. After this, Ohta *et al.* reported the carrier transport properties of Nb- and La-doped SrTiO<sub>3</sub> single crystals (carrier concentration,  $n \sim 10^{20}$  cm<sup>-3</sup>) at high temperatures

### 3. Thermoelectric phase diagram of the $\text{SrTiO}_3\text{--SrNbO}_3$ solid solution system

(~1000 K) to clarify the intrinsic thermoelectric properties of these materials<sup>10</sup>. Furthermore, the experimental discovery of unusually large thermopower outputs from superlattices and two-dimensional electron gases in  $\text{SrTiO}_3$ <sup>15,16</sup> spurred substantial research efforts into  $\text{SrTiO}_3$  superlattices<sup>17,18</sup> and heterostructures<sup>19-21</sup> for thermoelectric applications; for example, a superlattice composed of 1 unit cell (uc)  $\text{SrTi}_{0.8}\text{Nb}_{0.2}\text{O}_3$  and 10 uc  $\text{SrTiO}_3$  exhibited giant thermopower, most likely due to an electron confinement effect. Although electron confinement is strongly correlated with the electronic structure<sup>22,23</sup>, a full understanding of the fundamental electronic phase behavior of the  $\text{SrTi}_{1-x}\text{Nb}_x\text{O}_3$  solid solution system has not yet been developed.

In this chapter, we clarified the thermoelectric phase diagram for the full range of the  $\text{SrTiO}_3\text{--SrNbO}_3$  solid solution system (hereafter referred to as the  $\text{SrTi}_{1-x}\text{Nb}_x\text{O}_3$  ss,  $0.05 \leq x \leq 1$ ), and analyzed their crystal lattice parameters, as well as their electrical properties such as carrier concentration, Hall mobility, and thermopower, from which the carrier effective masses and relaxation times were derived. During these experiments, I observed that two thermoelectric phase boundaries exist within the system, which originate from the step-like decrease in carrier effective mass at  $x \sim 0.3$ , and from the minimum in carrier relaxation time at  $x \sim 0.5$ . The origin of these phase boundaries were analyzed by considering cases of isovalent/heterovalent B-site substitution. Parabolic Ti 3d orbitals were found to dominate electron conduction for compositions with  $x < 0.3$ , whereas the Nb 4d orbitals became more influential for compositions with  $x > 0.3$ . At  $x = 0.5$ , tetragonal distortion of the lattice, in which the B-site was composed of predominantly  $[\text{Ti}^{4+}/\text{Nb}^{4+}]$  ions, led to the formation of tail-like impurity bands, which maximized the electron scattering. The results obtained in this study may be used as a foundation for further work that seeks to improve the thermoelectric performance of  $\text{SrTi}_{1-x}\text{Nb}_x\text{O}_3$ .

### 3.2 Experimental

High-quality single crystals of SrTi<sub>1-x</sub>Nb<sub>x</sub>O<sub>3</sub> species with  $x > 0.1$  are not available due to the low solubility limit of Nb in the lattice<sup>24</sup>, epitaxial films of these material compositions can be fabricated by pulsed laser deposition (PLD)<sup>25</sup>. So in this study, approximately 100 nm thick SrTi<sub>1-x</sub>Nb<sub>x</sub>O<sub>3</sub> ( $x = 0.05, 0.1, 0.2, 0.3, 0.4, 0.5, 0.55, 0.6, 0.7, 0.8, 0.9, \text{ and } 1.0$ ) epitaxial films were fabricated by PLD using dense ceramic disks of a SrTiO<sub>3</sub>–SrNbO<sub>3</sub> mixture. Insulating (001) LaAlO<sub>3</sub> (pseudo-cubic perovskite,  $a = 3.79 \text{ \AA}$ ) was selected as the substrate. Growth conditions were precisely controlled, with a substrate temperature of 850 °C, oxygen pressure of  $\sim 10^{-4}$  Pa, laser fluence of 0.5–1 J cm<sup>-2</sup> pulse<sup>-1</sup>, yielding a growth rate of 0.3 pm pulse<sup>-1</sup>. Details of the PLD growth process of SrTi<sub>1-x</sub>Nb<sub>x</sub>O<sub>3</sub> developed by our group have been published elsewhere<sup>11,26,27</sup>.

Crystallographic analyses of the resultant films were performed by X-ray diffraction (XRD, Cu K $\alpha_1$ , ATX-G, Rigaku) and scanning transmission electron microscopy (STEM). TEM samples were fabricated using a cryo ion slicer (IB-09060CIS, JEOL). The thin film was observed using scanning transmission electron microscope (STEM) (JEM-ARM200CF, JEOL Co. Ltd) operated at 200 keV. High-angle annular dark-field (HAADF) images were taken with detection angle of 68 – 280 mrad. The electron energy loss spectra (EELS) were acquired in STEM mode by an Enfinium spectrometer (Gatan Inc) with energy resolution of 1 eV.

Electrical conductivity ( $\sigma$ ), carrier concentration ( $n$ ), and Hall mobility ( $\mu_{\text{Hall}}$ ) were measured at room temperature by a conventional d.c. four-probe method, using an In–Ga alloy electrode with van der Pauw geometry.  $S$  was measured at room temperature by creating a temperature gradient ( $\Delta T$ ) of  $\sim 4$  K across the film using two Peltier devices (while using two small thermocouples to monitor the actual temperatures of each end of

### 3. Thermoelectric phase diagram of the SrTiO<sub>3</sub>–SrNbO<sub>3</sub> solid solution system

the SrTi<sub>1-x</sub>Nb<sub>x</sub>O<sub>3</sub> films). The thermo-electromotive force ( $\Delta V$ ) and  $\Delta T$  were measured simultaneously, and  $S$ -values were obtained from the slope of the  $\Delta V$ – $\Delta T$  plots.

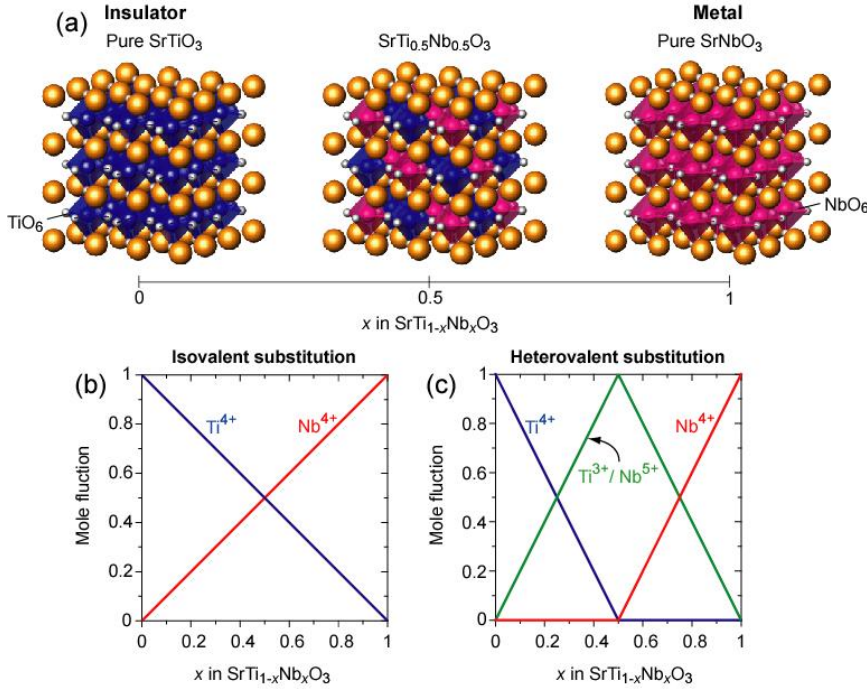
Band structures for SrTi<sub>1-x</sub>Nb<sub>x</sub>O<sub>3</sub> ( $x = 0, 0.25, 0.5, 0.75,$  and  $1$ ) were calculated based on the projector augmented-wave (PAW) method<sup>28</sup>, as implemented using VASP code<sup>29,30</sup>. For these calculations, Heyd-Scuseria-Ernzerhof (HSE) hybrid functionals were adopted<sup>31-33</sup>, and a plane-wave cutoff energy of 550 eV and a  $6 \times 6 \times 6$   $k$ -point mesh for cubic-perovskite were employed in the total-energy evaluation and geometry optimization for the unit cells of SrTiO<sub>3</sub> and SrNbO<sub>3</sub>, while special quasi-random structures (SQSs) were used in the case of SrTi<sub>1-x</sub>Nb<sub>x</sub>O<sub>3</sub> ( $x = 0.25, 0.5,$  and  $0.75$ ). The SQSs with eight Sr or Ti sites were constructed by optimizing the correlation functions of seven types of independent pairs using the CLUPAN code<sup>34,35</sup>.

### 3.3 Results and discussion

As summarized in Fig. 3.1, pure SrTiO<sub>3</sub> (space group  $Pm\bar{3}m$ , cubic perovskite structure,  $a = 3.905$  Å) is an insulator with a bandgap of 3.2 eV, in which the bottom of the conduction band is composed of triply degenerate, empty Ti 3d- $t_{2g}$  orbitals, while the top of the valence band is composed of fully occupied O 2p orbitals<sup>36</sup>. The valence state of Ti ions in crystalline SrTiO<sub>3</sub> is 4+ (Ti 3d<sup>0</sup>). On the other hand, pure SrNbO<sub>3</sub> (space group  $Pm\bar{3}m$ , cubic perovskite structure,  $a = 4.023$  Å) is a metallic conductor<sup>37-39</sup>, in which the valence state of the Nb ion is 4+ (Nb 4d<sup>1</sup>). In between SrTiO<sub>3</sub> and SrNbO<sub>3</sub> in the SrTi<sub>1-x</sub>Nb<sub>x</sub>O<sub>3</sub> ss, there are two possible types of valence state change in the Ti and Nb ions, as shown in Fig. 3.1(b) and (c): in the case of isovalent substitution [Fig. 3.1(b)], mole fraction of Ti<sup>4+</sup> proportionally decreases with increasing Nb<sup>4+</sup> ( $x$ ); on the other hand, heterovalent substitution, in which two Ti<sup>4+</sup> or Nb<sup>4+</sup> ions are substituted by adjacent

### 3. Thermoelectric phase diagram of the $\text{SrTiO}_3\text{--SrNbO}_3$ solid solution system

( $\text{Ti}^{3+}/\text{Nb}^{5+}$ ) ions, can occur as shown in Fig. 3.1(c). Based on these considerations, I focused on the valence state change of Ti and Nb ions in the  $\text{SrTi}_{1-x}\text{Nb}_x\text{O}_3$  ss.



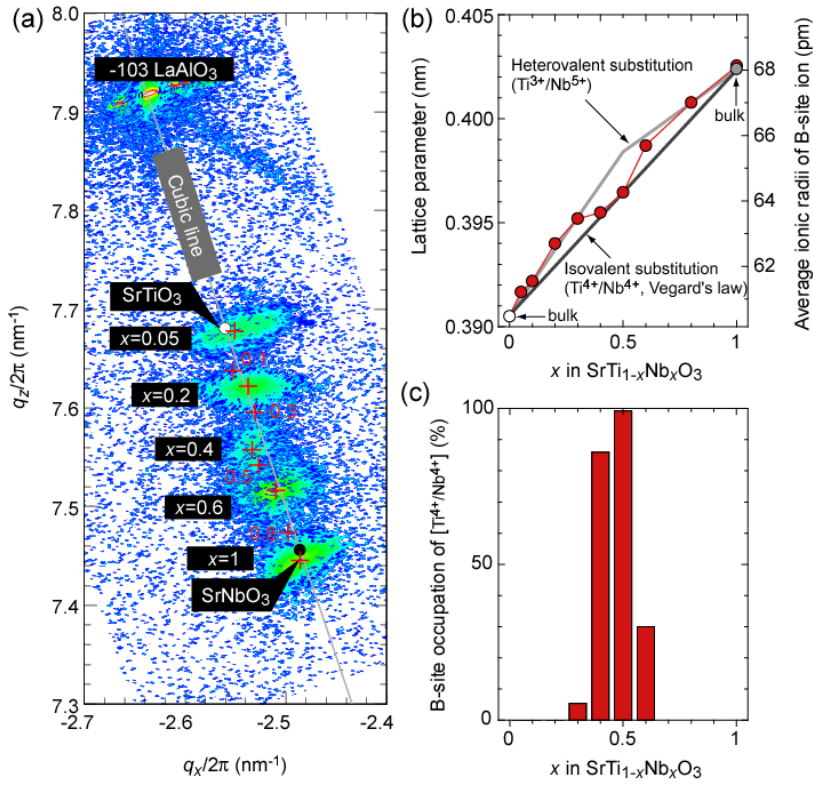
**Figure 3.1.** (Color online) Schematic crystal structure and possible valence state changes in the  $\text{SrTiO}_3\text{--SrNbO}_3$  solid solution system. (a) Schematic crystal structure. Pure  $\text{SrTiO}_3$  is an insulator with bandgap of 3.2 eV, in which the valence state of the Ti ions (blue,  $\text{TiO}_6$ ) is  $4+$  ( $\text{Ti } 3d^0$ ). On the other hand, pure  $\text{SrNbO}_3$  is a metal, in which the valence state of the Nb ions (Red,  $\text{NbO}_6$ ) is  $4+$  ( $\text{Nb } 4d^1$ ). (b)–(c) Possible valence state changes of Ti and Nb ions in the  $\text{SrTiO}_3\text{--SrNbO}_3$  solid solution system: (b) isovalent substitution, where  $\text{Ti}^{4+}$  is substituted by  $\text{Nb}^{4+}$ ; (c) heterovalent substitution, where two  $\text{Ti}^{4+}/\text{Nb}^{4+}$  ions are substituted by adjacent  $\text{Ti}^{3+}/\text{Nb}^{5+}$  ions.

Fig. 3.2(a) summarizes the X-ray reciprocal space mappings (RSMs) around the  $(\bar{1}03)$  diffraction spot of  $\text{LaAlO}_3$  (overlaid). Intense diffraction spots from  $(\bar{1}03)$   $\text{SrTi}_{1-x}\text{Nb}_x\text{O}_3$  are seen together with those from the  $\text{LaAlO}_3$  substrate, indicating that incoherent hetero-

### 3. Thermoelectric phase diagram of the SrTiO<sub>3</sub>–SrNbO<sub>3</sub> solid solution system

epitaxial growth of the target materials occurred for all  $x$  compositions. The peak positions of the diffraction spots from each composition correspond well with the cubic line ( $q_z/q_x = -3$ ), indicating that no epitaxial strain was induced in the films. It should be noticed that a slight tetragonal distortion was observed in the  $x = 0.4$  ( $c/a = 1.0057$ ) and  $0.5$  ( $c/a = 1.0050$ ) samples. From the RSMs of the SrTi<sub>1-x</sub>Nb<sub>x</sub>O<sub>3</sub> films, the lattice parameters were extracted using the formula  $a = (2\pi/q_x \cdot 2\pi/q_x \cdot 6\pi/q_z)^{1/3}$ . Fig. 3.2(b) plots the lattice parameters of the SrTi<sub>1-x</sub>Nb<sub>x</sub>O<sub>3</sub> film as a function of  $x$ : an M-shaped trend was observed, along with a general increase in the lattice parameter with increasing  $x$ . In order to analyze the changes in lattice parameter, we calculated the average ionic radii in the crystal structure and used Shannon's ionic radii as a comparison<sup>40</sup>: Ti<sup>4+</sup> (60.5 pm), Ti<sup>3+</sup> (67.0 pm), Nb<sup>4+</sup> (68.0 pm), and Nb<sup>5+</sup> (64.0 pm). In the ranges of  $0.05 \leq x \leq 0.3$  and  $x \geq 0.6$ , the observed lattice parameters closely followed the heterovalent substitution line, suggesting that two Ti<sup>4+</sup> or Nb<sup>4+</sup> ions are substituted by adjacent (Ti<sup>3+</sup>/Nb<sup>5+</sup>) ions<sup>41</sup>. On the other hand, at  $x = 0.4$  and  $0.5$ , the observed lattice parameter corresponded well with the isovalent substitution line; moreover, at  $x = 0.5$ , the B-site occupation of [Ti<sup>4+</sup>/Nb<sup>4+</sup>] was almost 100%, as shown in Fig. 3.2(c).

### 3. Thermoelectric phase diagram of the SrTiO<sub>3</sub>–SrNbO<sub>3</sub> solid solution system



**Figure 3.2.** (Color online) Crystallographic characterization of the SrTi<sub>1-x</sub>Nb<sub>x</sub>O<sub>3</sub> epitaxial films on a (001) LaAlO<sub>3</sub> single crystal substrate. (a) X-ray reciprocal space mappings around the ( $\bar{1}03$ ) diffraction spot of the SrTi<sub>1-x</sub>Nb<sub>x</sub>O<sub>3</sub> epitaxial films. The location of the LaAlO<sub>3</sub> diffraction spot,  $(q_x/2\pi, q_z/2\pi) = (-2.64, 7.92)$ , corresponds with the pseudo-cubic lattice parameter of LaAlO<sub>3</sub> ( $a = 0.379$  nm). Red symbols (+) indicate the peak positions of the SrTi<sub>1-x</sub>Nb<sub>x</sub>O<sub>3</sub> epitaxial films. (b) Changes in the lattice parameters of the SrTi<sub>1-x</sub>Nb<sub>x</sub>O<sub>3</sub> films (circles, left axis), with superimposed isovalent/heterovalent substitution lines (black line: isovalent substitution, gray line: heterovalent substitution, right axis), calculated using Shannon's ionic radii<sup>40</sup>. (c) Change in the B-site occupation by [Ti<sup>4+</sup>/Nb<sup>4+</sup>] derived from the data in (b).

In order to further clarify the occupation of B-sites by [Ti<sup>4+</sup>/Nb<sup>4+</sup>], the atomic arrangement and electronic structure of the  $x = 0.5$  film were analyzed by STEM and EELS. Fig. 3.3(a) shows a cross-sectional HAADF-STEM image of a SrTi<sub>0.5</sub>Nb<sub>0.5</sub>O<sub>3</sub> film.

### 3. Thermoelectric phase diagram of the SrTiO<sub>3</sub>–SrNbO<sub>3</sub> solid solution system

Periodical mismatch dislocations with an interval of ~8.5 nm were seen at the heterointerfaces. If the strain in the thin-film were fully relaxed by such misfit dislocations, it would be possible to calculate the spacing between dislocations ( $d$ ) from  $d = \mathbf{b} / \delta$ , where  $\mathbf{b}$  is the Burgers vector and  $\delta$  is the lattice mismatch between thin-film and substrate<sup>42</sup>: using the lattice parameters obtained from XRD [ $\delta = (q_{x\text{sub}} - q_{x\text{film}}) / q_{x\text{film}} = +0.0435$ ], a dislocation spacing of 8.7 nm was estimated, suggesting that the dislocations do fully relax the strain in the film.

Although superspots originating from (111) diffraction are often observed in AB<sub>0.5</sub>B'<sub>0.5</sub>O<sub>3</sub> compositions that crystallize in B-site-ordered double perovskite structures<sup>43</sup>, these were not observed in the SrTi<sub>0.5</sub>Nb<sub>0.5</sub>O<sub>3</sub> film [Fig. 3.3(b)], most likely due to the slight tetragonal distortion of the crystal structure. Fig. 3.3(c) and (d) shows the EELS spectra acquired around the Ti  $L$  (c) and O  $K$  edges (d); the reported EELS spectra of Ti<sup>3+</sup>/Ti<sup>4+</sup><sup>44</sup> and Nb<sup>4+</sup>/Nb<sup>5+</sup><sup>45</sup> are also plotted for comparison. In the Ti  $L$  edge spectrum (c),  $t_{2g}$  and  $e_g$  peak splitting was clearly observed for Ti  $L_3$ , indicating that the dominant valence state of Ti is 4+. In the O  $K$  edge spectra (d), two intense peaks (assigned as A and B) were clearly seen, with the intensity of peak B being higher than A, which was noted to be a characteristic feature of Nb<sup>4+</sup> in a previous study<sup>45</sup>; the peak intensity ratio A/B was calculated to be 0.66, which roughly corresponds with the Nb<sup>4+</sup> spectrum (0.66). From these results, it could be concluded that isovalent substitution of Ti<sup>4+</sup>/Nb<sup>4+</sup> dominates in the  $x = 0.5$  composition.

### 3. Thermoelectric phase diagram of the SrTiO<sub>3</sub>–SrNbO<sub>3</sub> solid solution system

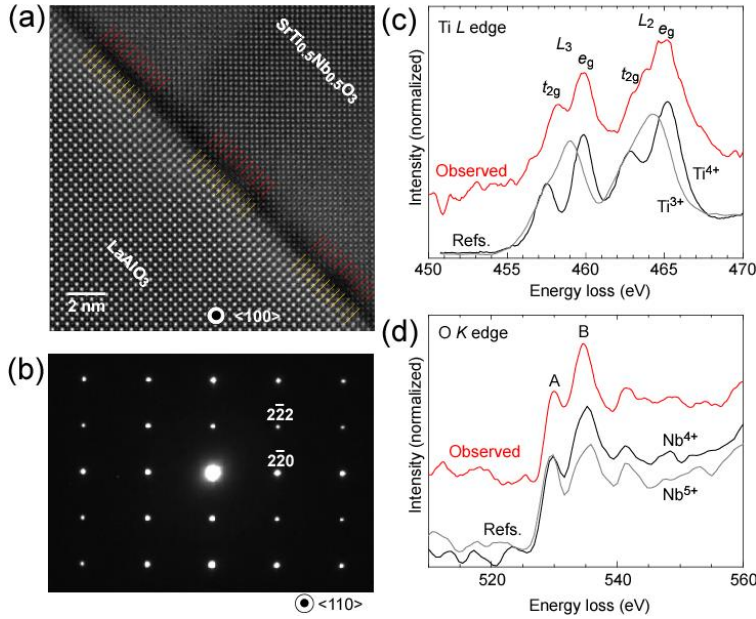


**Figure 3.3.** (Color online) | Electron microscopy analyses of a SrTi<sub>1-x</sub>Nb<sub>x</sub>O<sub>3</sub> film with composition  $x = 0.5$ . (a) HAADF-STEM image acquired with the electron beam incident along the  $\langle 100 \rangle$  direction. Periodic misfit dislocations ( $\sim 8.5$  nm interval) at the heterointerface are indicated by red lines. (b) Selected-area electron diffraction pattern acquired with the electron beam incident along the  $\langle 110 \rangle$  direction. (c)–(d) EELS spectra acquired around the Ti  $L$  edge (c) and O  $K$  edge (d). EELS spectra for Ti<sup>3+</sup>/Ti<sup>4+</sup><sup>44</sup> and Nb<sup>4+</sup>/Nb<sup>5+</sup><sup>45</sup> from previous studies are also plotted for comparison.

Then  $\sigma$ ,  $n$ , and  $\mu_{\text{Hall}}$  were measured by Hall effect measurements. Generally,  $\sigma$  was observed to increase with increasing  $x$ , as shown in Fig. 3.4(a); additionally, it was noted that there was a sharp increase in  $\sigma$  between  $0.5 < x < 0.6$ , suggesting the existence of an electronic phase boundary at  $x \sim 0.5$ .  $n$  was also measured to increase with increasing  $x$ , which is almost correspond with the nominal value ( $n = x$  in a unit cell) [Fig. 3.4(b)]. For the mobility, as shown in Fig. 3.4(c),  $\mu_{\text{Hall}}$  for compositions with  $x < 0.5$  remained almost constant at  $\sim 6$  cm<sup>2</sup> V<sup>-1</sup> s<sup>-1</sup>, which is consistent with other reported values<sup>46,47</sup>. As was observed for  $\sigma$ , a sharp increase in  $\mu_{\text{Hall}}$  from  $\sim 5$  cm<sup>2</sup> V<sup>-1</sup> s<sup>-1</sup> to  $\sim 10$  cm<sup>2</sup> V<sup>-1</sup> s<sup>-1</sup> was observed between compositions with  $x = 0.5$  and  $x = 0.6$ , after which the values steadily

### 3. Thermoelectric phase diagram of the SrTiO<sub>3</sub>–SrNbO<sub>3</sub> solid solution system

increased to  $\sim 12 \text{ cm}^2 \text{ V}^{-1} \text{ s}^{-1}$  at  $x = 1$  (cf. a value of  $\sim 14 \text{ cm}^2 \text{ V}^{-1} \text{ s}^{-1}$  measured for this composition in a previous study<sup>38</sup>). From these results, it can be concluded that the small  $\mu_{\text{Hall}}$  dominates the electronic phase boundary at  $x \sim 0.5$ .

In order to further elucidate the origin of the electronic phase boundary,  $S$  was measured across the composition range: by measuring the values of both  $n$  and  $S$ , the density of states effective mass ( $m^*$ ) could be further deduced, as outlined in equations (3-1)–(3-3) below. Not surprisingly,  $|S|$  was found to monotonically decrease with increasing  $x$ , as shown in Fig. 3.4(d). Then  $m^*$  was calculated using the following relation between  $n$  and  $S$ <sup>48</sup>,

$$S = -\frac{k_B}{e} \left[ \frac{(r+2)F_{r+1}(\xi)}{(r+1)F_r(\xi)} \right] - \xi \quad (3-1)$$

where  $k_B$ ,  $\xi$ ,  $r$ , and  $F_r$  are the Boltzmann constant, chemical potential, scattering parameter of relaxation time, and Fermi integral, respectively.  $F_r$  is given by,

$$F_r(\xi) = \int_0^\infty \frac{x^r}{1 + e^{x-\xi}} dx \quad (3-2)$$

and  $n$  by,

$$n_- = 4\pi \left( \frac{2m^*k_B T}{h^2} \right)^{3/2} F_{1/2}(\xi) \quad (3-3)$$

where  $h$  and  $T$  are the Planck constant and absolute temperature, respectively. Using the equations (3-1)–(3-3), values of  $m^*$  were obtained, which are presented in Fig. 3.4(e): a step-like decrease of  $m^*$  was observed with increasing  $x$  value.  $m^*$  for compositions with  $x < 0.3$  was calculated to be  $\sim 1.1m_0$ , which corresponds well with the values reported by Okuda *et al.*<sup>9</sup>, while for compositions with  $x > 0.3$ ,  $m^*$  was  $\sim 0.7m_0$ . At  $x = 1$  (SrNbO<sub>3</sub>),  $m^*$  further decreased to  $0.5m_0$ , agreeing well with values calculated in another study using spin-polarized DFT calculations ( $0.4m_0$ )<sup>49</sup>. It is speculated that there is a percolation threshold for compositions with  $x \sim 0.3$ , and that parabolic Ti 3d orbitals dominate electron conduction when  $x < 0.3$ , whereas the Nb 4d orbitals determine electron

### 3. Thermoelectric phase diagram of the SrTiO<sub>3</sub>–SrNbO<sub>3</sub> solid solution system

conduction when  $x > 0.3$ . Finally, the relaxation time,  $\tau$ , was extracted from the  $\mu_{\text{Hall}}$  and  $m^*$  values ( $= e \cdot \tau \cdot m^{*-1}$ ): these results are shown in Fig. 3.4(f). The  $\tau$  values in the range  $0.05 \leq x \leq 0.2$  are  $\sim 4$  fs, followed by a drop, reaching a minimum value of  $\sim 2$  fs at  $x = 0.5$ . After  $x = 0.5$ ,  $\tau$  initially increases sharply to 3.5 fs at  $x = 0.6$ , with a much more gradual increase with  $x$  composition in the range  $0.6 \leq x \leq 0.9$ . Lastly, there was a slight drop in  $\tau$  value to 3.2 fs for the  $x = 1$  composition. The trend's trough shape, in particular, the sharp increase of  $\tau$  from  $\sim 2$  to  $\sim 3.5$  fs in the range  $0.5 < x < 0.6$ , clearly indicates that  $\tau$  dominates the electronic phase boundary at  $x \sim 0.5$ . Yamamoto *et al.* reported that  $\tau$  of the SrTi<sub>0.8</sub>Nb<sub>0.2</sub>O<sub>3</sub> epitaxial films was significantly reduced by Sr-site substitution with Ca or Ba, due to the occurrence of tetragonal lattice distortion<sup>26</sup>: since slight tetragonal distortion was observed in the  $x = 0.4$  and 0.5 films, as shown in Fig. 3.2 (a), the tetragonal distortion may also minimize the  $\tau$  in this set of thin-films.

### 3. Thermoelectric phase diagram of the $\text{SrTiO}_3$ – $\text{SrNbO}_3$ solid solution system

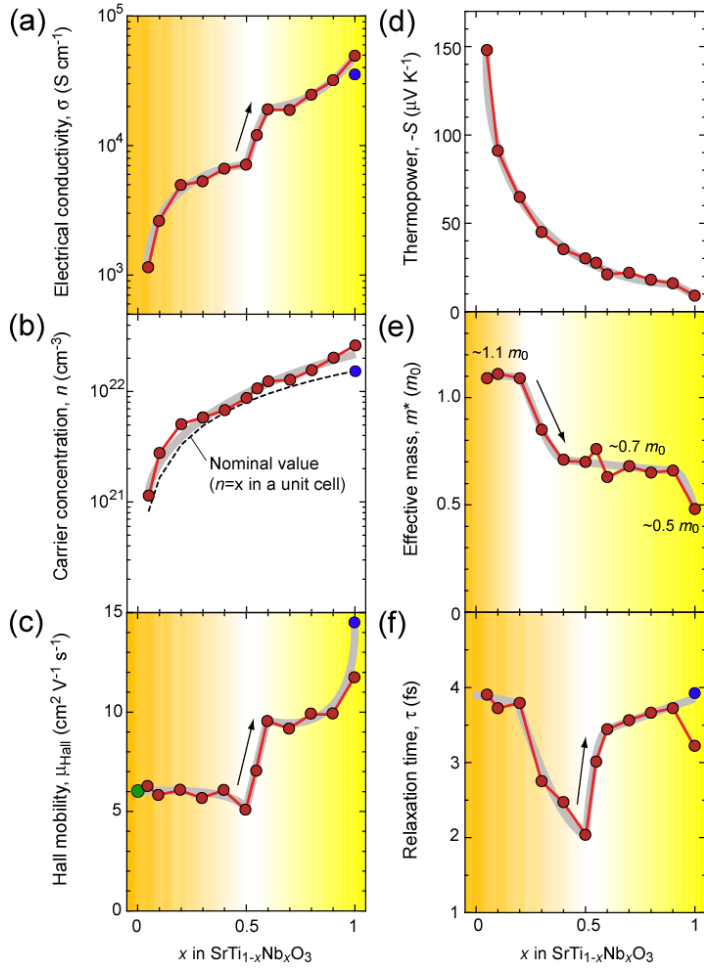


**Figure 3.4.** (Color online) Room temperature electron transport properties of the  $\text{SrTi}_{1-x}\text{Nb}_x\text{O}_3$  epitaxial films: (a) electrical conductivity ( $\sigma$ ), (b) carrier concentration ( $n$ ), (c) Hall mobility ( $\mu_{\text{Hall}}$ ), (d) thermopower ( $S$ ), (e) effective mass ( $m^*$ ), and (f) carrier relaxation time ( $\tau$ ). Previously reported data for  $\sigma$ ,  $n$ , and  $\mu_{\text{Hall}}$  are plotted for comparison (blue circles indicate a  $\text{SrNbO}_3$  film from<sup>38</sup>; green circles are for slightly Nb-doped  $\text{SrTiO}_3$ <sup>47</sup>). The gray lines are drawn as a visual guide.

Then, I plotted the thermoelectric power factor ( $S^2 \cdot \sigma$ ) of the  $\text{SrTi}_{1-x}\text{Nb}_x\text{O}_3$  ss together with values reported in previous studies (Fig. 3.5). In the region around  $x \sim 0.05$  where the observed data (red circles / red line) overlap with the reported values from Ref. 15

### 3. Thermoelectric phase diagram of the SrTiO<sub>3</sub>–SrNbO<sub>3</sub> solid solution system

(white circles / grey line), the two data sets match well. There are two local maxima in  $S^2 \cdot \sigma$  — firstly at  $x \sim 0.05$  ( $\sim 2.5 \text{ mW m}^{-1} \text{ K}^{-2}$ ), and secondly at  $\sim 0.55$  ( $\sim 0.9 \text{ mW m}^{-1} \text{ K}^{-2}$ ). Two thermoelectric phase boundaries were also observed in the system, occurring in the regions around  $x \sim 0.3$  and  $x \sim 0.5$ , as shown in the inset. Since  $S$  is strongly correlated with  $m^*$ , the sharp decrease in  $m^*$  at  $x \sim 0.3$  [Fig. 3.4 (e)] accounts for the concomitant reduction in  $S$ . In addition, the small value of  $\tau$  at  $x \sim 0.5$  (where  $\tau$  was measured to reach a minimum) contributed greatly to the observed reduction in  $\sigma$ . In conclusion, in order to maximize the thermoelectric performance of the SrTi<sub>1-x</sub>Nb<sub>x</sub>O<sub>3</sub> ss, the use of compositions with  $x \leq 0.2$  would be the most suitable.

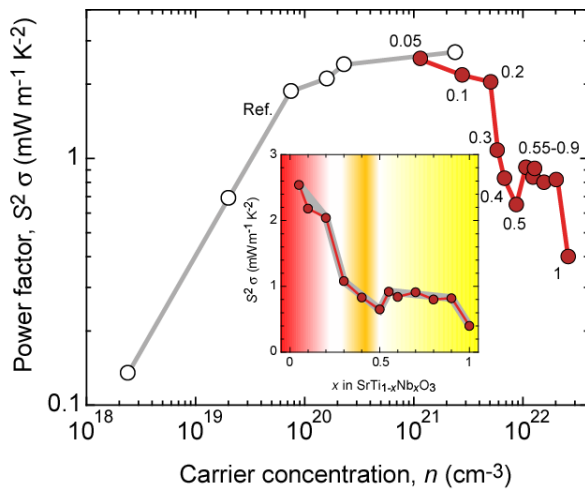


**Figure 3.5.** (Color online) Thermoelectric phase diagram for the SrTiO<sub>3</sub>–SrNbO<sub>3</sub> solid solution system. The thermoelectric power factor ( $S^2 \cdot \sigma$ ) of the SrTiO<sub>3</sub>–SrNbO<sub>3</sub> solid solution system is plotted, alongside previously reported values<sup>15</sup>. The  $x$  dependence of  $S^2 \cdot \sigma$  is shown in the inset. The system's thermoelectric phase boundaries are clearly seen at  $x \sim 0.3$  and  $\sim 0.5$ .

### 3. Thermoelectric phase diagram of the SrTiO<sub>3</sub>–SrNbO<sub>3</sub> solid solution system

Finally, the band structures for SrTi<sub>1-x</sub>Nb<sub>x</sub>O<sub>3</sub> ( $x = 0, 0.25, 0.5, 0.75,$  and  $1$ ) were calculated in order to elucidate the origin of the two electronic phase boundaries using  $2 \times 2 \times 2$  supercell model structures. Fig. 3.6 summarizes the resultant total and orbital-projected density of states (DOS) of the SrTi<sub>1-x</sub>Nb<sub>x</sub>O<sub>3</sub> compositions around the bandgap. The energy origin was set at the Fermi level,  $E_F$  (dotted line).  $E_F$  was found to increase gradually with the increase in  $x$ . When  $x > 0$ , the  $E_F$  was located higher energy side of the conduction band minimum (Ti 3d – Nb 4d hybridized orbital), indicating that the compositions in this range are degenerate semiconductors (or metals). The similar band structure between  $x = 0$  and  $x = 0.25$  compositions is consistent with the similar  $m^*$  and  $\tau$  values recorded experimentally from films with  $x < 0.3$ . Meanwhile, both  $x = 0.5$  and  $x = 0.75$  SrTi<sub>1-x</sub>Nb<sub>x</sub>O<sub>3</sub> were found to possess a tail-like feature in the DOS below the  $E_F$ . The major component of the tail at  $x = 0.75$  was the Ti 3d, whereas at  $x = 0.5$ , Ti 3d and Nb 4d orbitals both made comparable contributions to the observed feature. The former corroborates the suggestion from the experimental results that Ti<sup>3+</sup> ions are present [Figs. 3.2 (b) and (c)]. However, the latter is completely different from the experimentally obtained fact that isovalent substitution of Ti<sup>4+</sup>/Nb<sup>4+</sup> dominates in the  $x = 0.5$  composition. As mentioned above, we did not observe any superstructure such as B-site ordered Sr<sub>2</sub>TiNbO<sub>6</sub>. Although we used special quasi-random structures (SQSs) in the case of the band calculations of SrTi<sub>1-x</sub>Nb<sub>x</sub>O<sub>3</sub> ( $x = 0.25, 0.5, 0.75$ ), B-site ordering still remained due to the finite cell size ( $2 \times 2 \times 2$  supercell of cubic perovskite). This should be the main reason that the calculation result of  $x = 0.5$  does not reflect the experimentally obtained solid solution crystal. Moreover the characteristic decrease in  $\tau$  measured for compositions around  $x = 0.5$  (and was not observed when  $x > 0.6$ ) may imply that the electrons from the Nb 4d orbitals in the tail-like DOS do not contribute to the electrical conductivity of the SrTi<sub>1-x</sub>Nb<sub>x</sub>O<sub>3</sub> ss.

### 3. Thermoelectric phase diagram of the $\text{SrTiO}_3\text{--SrNbO}_3$ solid solution system

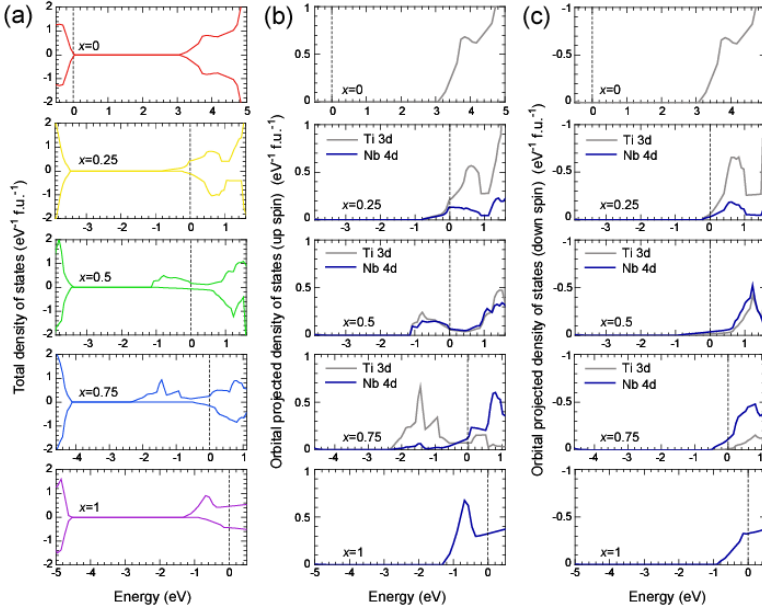


**Figure 3.6.** (Color online) Calculated density of states (DOS) for  $\text{SrTi}_{1-x}\text{Nb}_x\text{O}_3$  ss ( $x = 0, 0.25, 0.5, 0.75, \text{ and } 1$ ). (a) total DOS, (b)–(c) orbital-projected DOS. The energy origin was set at the Fermi level,  $E_F$ , indicated by the dotted line.

### 3.4 Conclusion

In this chapter, we have clarified the thermoelectric phase diagram for the  $\text{SrTi}_{1-x}\text{Nb}_x\text{O}_3$  ( $0.05 \leq x \leq 1$ ) solid solution system through characterization of epitaxial thin-films. Two thermoelectric phase boundaries were observed in the system, which originate from the combination of a step-like decrease in carrier effective mass at  $x \sim 0.3$  with the local minimum carrier relaxation time at  $x \sim 0.5$ . The origins of these electronic phase boundaries were analyzed in the context of isovalent/heterovalent B-site substitution. Parabola-shaped Ti 3d orbitals dominate electron conduction for compositions  $0 < x < 0.3$ , whereas the Nb 4d orbitals dominate when  $x > 0.3$ . At  $x \sim 0.5$ , a tetragonal distortion of the lattice occurs, in which the B-site is composed of predominantly  $[\text{Ti}^{4+}/\text{Nb}^{4+}]$  ions, leading to the formation of tail-like impurity bands in the density of states, which

maximizes electron scattering.

These findings may prove useful in further improving and optimizing the thermoelectric performance of SrTi<sub>1-x</sub>Nb<sub>x</sub>O<sub>3</sub>. Moreover, the analyses of the B-site ion valence states in this study provide valuable information that could be used in the design of other functional materials based on transition metal oxides.

## References

- 1 Rowe, D. M. *CRC Handbook of Thermoelectrics*. (CRC Press, 1995).
- 2 Goldsmid, H. J. *Introduction to Thermoelectricity*. (Springer, 2010).
- 3 Tritt, T. M. & Subramanian, M. A. Thermoelectric materials, phenomena, and applications: A bird's eye view. *MRS Bulletin* **31**, 188-194 (2006).
- 4 Snyder, G. J. & Toberer, E. S. Complex thermoelectric materials. *Nature Materials* **7**, 105-114 (2008).
- 5 Terasaki, I., Sasago, Y. & Uchinokura, K. Large thermoelectric power in NaCo<sub>2</sub>O<sub>4</sub> single crystals. *Phys. Rev. B* **56**, 12685-12687 (1997).
- 6 Lee, M. *et al.* Large enhancement of the thermopower in Na<sub>x</sub>CoO<sub>2</sub> at high Na doping. *Nature Materials* **5**, 537-540 (2006).
- 7 Masset, A. C. *et al.* Misfit-layered cobaltite with an anisotropic giant magnetoresistance: Ca<sub>3</sub>Co<sub>4</sub>O<sub>9</sub>. *Phys Rev B* **62**, 166-175 (2000).
- 8 Li, S. W., Funahashi, R., Matsubara, I., Ueno, K. & Yamada, H. High temperature thermoelectric properties of oxide Ca<sub>9</sub>Co<sub>12</sub>O<sub>28</sub>. *J Mater Chem* **9**, 1659-1660 (1999).
- 9 Okuda, T., Nakanishi, K., Miyasaka, S. & Tokura, Y. Large thermoelectric response of metallic perovskites: Sr<sub>1-x</sub>La<sub>x</sub>TiO<sub>3</sub> (0 ≤ x ≤ 0.1). *Phys Rev B* **63**, 113104 (2001).
- 10 Ohta, S., Nomura, T., Ohta, H. & Koumoto, K. High-temperature carrier transport and thermoelectric properties of heavily La- or Nb-doped SrTiO<sub>3</sub> single crystals. *J Appl Phys* **97**, 034106 (2005).
- 11 Ohta, S. *et al.* Large thermoelectric performance of heavily Nb-doped SrTiO<sub>3</sub> epitaxial film at high temperature. *Appl Phys Lett* **87**, 092108 (2005).
- 12 Koumoto, K. *et al.* Thermoelectric Ceramics for Energy Harvesting. *J Am Ceram Soc* **96**, 1-23 (2013).

### 3. Thermoelectric phase diagram of the SrTiO<sub>3</sub>–SrNbO<sub>3</sub> solid solution system

- 13 Ohta, H., Sugiura, K. & Koumoto, K. Recent progress in oxide thermoelectric materials: p-type Ca<sub>3</sub>Co<sub>4</sub>O<sub>9</sub> and n-type SrTiO<sub>3</sub>. *Inorganic Chemistry* **47**, 8429-8436 (2008).
- 14 Fergus, J. W. Oxide materials for high temperature thermoelectric energy conversion. *J. Eur. Ceram. Soc.* **32**, 525-540 (2012).
- 15 Ohta, H. *et al.* Giant thermoelectric Seebeck coefficient of two-dimensional electron gas in SrTiO<sub>3</sub>. *Nature Materials* **6**, 129-134 (2007).
- 16 Ohta, H. *et al.* Unusually Large Enhancement of Thermopower in an Electric Field Induced Two-Dimensional Electron Gas. *Adv. Mater.* **24**, 740-744 (2012).
- 17 Choi, W. S., Ohta, H. & Lee, H. N. Thermopower enhancement by fractional layer control in 2D oxide superlattices. *Adv Mater* **26**, 6701-6705 (2014).
- 18 Delugas, P. *et al.* Doping-induced dimensional crossover and thermopower burst in Nb-doped SrTiO<sub>3</sub> superlattices. *Phys Rev B* **88**, 045310 (2013).
- 19 Cain, T. A. *et al.* Seebeck coefficient of a quantum confined, high-electron-density electron gas in SrTiO<sub>3</sub>. *Appl Phys Lett* **100**, 161601 (2012).
- 20 Pallecchi, I. *et al.* Giant oscillating thermopower at oxide interfaces. *Nat Commun* **6**, 6678 (2015).
- 21 Shimizu, S., Ono, S., Hatano, T., Iwasa, Y. & Tokura, Y. Enhanced cryogenic thermopower in SrTiO<sub>3</sub> by ionic gating. *Phys Rev B* **92**, 165304 (2015).
- 22 Hicks, L. D. & Dresselhaus, M. S. Effect of quantum-well structures on the thermoelectric figure of merit. *Phys. Rev. B* **47**, 12727-12731 (1993).
- 23 Hung, N. T., Hasdeo, E. H., Nugraha, A. R. T., Dresselhaus, M. S. & Saito, R. Quantum Effects in the Thermoelectric Power Factor of Low-Dimensional Semiconductors. *Phys Rev Lett* **117**, 036602 (2016).
- 24 Rodenbacher, C. *et al.* Homogeneity and variation of donor doping in Verneuil-grown SrTiO<sub>3</sub>:Nb single crystals. *Sci Rep-Uk* **6**, 32250 (2016).
- 25 Tomio, T., Miki, H., Tabata, H., Kawai, T. & Kawai, S. Control of electrical-conductivity in laser-deposited SrTiO<sub>3</sub> thin-films with Nb doping. *J. Appl. Phys.* **76**, 5886-5890 (1994).
- 26 Yamamoto, M., Ohta, H. & Koumoto, K. Thermoelectric phase diagram in a CaTiO<sub>3</sub>-SrTiO<sub>3</sub>-BaTiO<sub>3</sub> system. *Appl. Phys. Lett.* **90**, 072101 (2007).
- 27 Mune, Y., Ohta, H., Koumoto, K., Mizoguchi, T. & Ikuhara, Y. Enhanced Seebeck coefficient of quantum-confined electrons in SrTiO<sub>3</sub>/SrTi<sub>0.8</sub>Nb<sub>0.2</sub>O<sub>3</sub> superlattices. *Appl. Phys. Lett.* **91**, 192105 (2007).
- 28 Blochl, P. E. Projector Augmented-Wave Method. *Phys Rev B* **50**, 17953-17979 (1994).

### 3. Thermoelectric phase diagram of the SrTiO<sub>3</sub>–SrNbO<sub>3</sub> solid solution system

- 29 Kresse, G. & Joubert, D. From ultrasoft pseudopotentials to the projector augmented-wave method. *Phys Rev B* **59**, 1758-1775 (1999).
- 30 Kresse, G. & Furthmuller, J. Efficient iterative schemes for ab initio total-energy calculations using a plane-wave basis set. *Phys Rev B* **54**, 11169-11186 (1996).
- 31 Heyd, J., Scuseria, G. E. & Ernzerhof, M. Hybrid functionals based on a screened Coulomb potential (vol 118, pg 8207, 2003). *J Chem Phys* **124**, 2204597 (2006).
- 32 Krukau, A. V., Vydrov, O. A., Izmaylov, A. F. & Scuseria, G. E. Influence of the exchange screening parameter on the performance of screened hybrid functionals. *J Chem Phys* **125**, 2404663 (2006).
- 33 Heyd, J., Scuseria, G. E. & Ernzerhof, M. Hybrid functionals based on a screened Coulomb potential. *J Chem Phys* **118**, 8207-8215 (2003).
- 34 Seko, A., Koyama, Y. & Tanaka, I. Cluster expansion method for multicomponent systems based on optimal selection of structures for density-functional theory calculations. *Phys. Rev. B* **80**, 165122 (2009).
- 35 Seko, A. *clupan*, <<http://sourceforge.net/projects/clupan>> (2007).
- 36 Mattheiss, L. F. Energy-Bands for KNiF<sub>3</sub>, SrTiO<sub>3</sub>, KMoO<sub>3</sub>, and KTaO<sub>3</sub>. *Phys Rev B* **6**, 4718-4740 (1972).
- 37 Turzhevsky, S. A., Novikov, D. L., Gubanov, V. A. & Freeman, A. J. Electronic-Structure and Crystal-Chemistry of Niobium Oxide Phases. *Phys Rev B* **50**, 3200-3208 (1994).
- 38 Oka, D., Hirose, Y., Nakao, S., Fukumura, T. & Hasegawa, T. Intrinsic high electrical conductivity of stoichiometric SrNbO<sub>3</sub> epitaxial thin films. *Phys. Rev. B* **92**, 205102 (2015).
- 39 Xu, X. X., Randorn, C., Efstathiou, P. & Irvine, J. T. S. A red metallic oxide photocatalyst. *Nature Materials* **11**, 595-598 (2012).
- 40 Shannon, R. D. Revised Effective Ionic-Radii and Systematic Studies of Interatomic Distances in Halides and Chalcogenides. *Acta Crystallogr A* **32**, 751-767 (1976).
- 41 Ishida, Y. *et al.* Coherent and incoherent excitations of electron-doped SrTiO<sub>3</sub>. *Phys. Rev. Lett.* **100**, 056401 (2008).
- 42 Ikuhara, Y. & Pirouz, P. High resolution transmission electron microscopy studies of metal/ceramics interfaces. *Microsc. Res. Tech.* **40**, 206-241 (1998).
- 43 Davies, P. K., Tong, J. Z. & Negas, T. Effect of ordering-induced domain boundaries on low-loss Ba(Zn<sub>1/3</sub>Ta<sub>2/3</sub>)O<sub>3</sub>-BaZrO<sub>3</sub> perovskite microwave dielectrics. *J. Am. Ceram. Soc.* **80**, 1727-1740 (1997).
- 44 Muller, D. A., Nakagawa, N., Ohtomo, A., Grazul, J. L. & Hwang, H. Y. Atomic-

3. Thermoelectric phase diagram of the SrTiO<sub>3</sub>–SrNbO<sub>3</sub> solid solution system

- scale imaging of nanoengineered oxygen vacancy profiles in SrTiO<sub>3</sub>. *Nature* **430**, 657-661 (2004).
- 45 Chen, C. L., Wang, Z. C., Lichtenberg, F., Ikuhara, Y. & Bednorz, J. G. Patterning Oxide Nanopillars at the Atomic Scale by Phase Transformation. *Nano Lett.* **15**, 6469-6474 (2015).
- 46 Tufte, O. N. & Chapman, P. W. Electron Mobility in Semiconducting Strontium Titanate. *Phys. Rev.* **155**, 796 (1967).
- 47 Frederikse, H. P. R., Thurber, W. R. & Hosler, W. R. Electronic transport in strontium titanate. *Phys. Rev.* **134**, A442 (1964).
- 48 Vining, C. B. A model for the high-temperature transport properties of heavily doped n-type silicon-germanium alloys. *J. Appl. Phys.* **69**, 331-341 (1991).
- 49 Zhu, Y. T., Dai, Y., Lai, K. R., Li, Z. J. & Huang, B. B. Optical Transition and Photocatalytic Performance of d(1) Metallic Perovskites. *J Phys Chem C* **117**, 5593-5598 (2013).

## 4. Fabrication and Thermoelectric Properties of $\text{SrTi}_{1-x}\text{Nb}_x\text{O}_3/\text{SrTiO}_3$ ( $0.1 \leq x \leq 0.9$ ) Superlattices

### 4.1 Introduction

Currently, more than 60% of the energy produced from fossil fuels is lost as waste heat. Thermoelectric energy conversion, which is the process where waste heat is transformed into electricity by the Seebeck effect, is attracting attention as a potential energy harvesting technology<sup>1-4</sup>. The performance of thermoelectric materials is generally evaluated in terms of a dimensionless figure of merit,  $ZT = S^2 \cdot \sigma \cdot T \cdot \kappa^{-1}$ , where  $Z$  is the figure of merit,  $T$  is the absolute temperature,  $S$  is the thermopower ( $\equiv$ Seebeck coefficient),  $\sigma$  is the electrical conductivity, and  $\kappa$  is the sum of the electronic ( $\kappa_{ele}$ ) and lattice thermal conductivities ( $\kappa_{lat}$ ) of a thermoelectric material.

There are two strategies to improve  $ZT$  of a thermoelectric material. One is to reduce  $\kappa_{lat}$ . Recently, state-of-the-art nanostructuring techniques have reduced  $\kappa_{lat}$  significantly through phonon scattering by nanosized structural defects<sup>5-8</sup>. Such techniques have realized high-performance thermoelectric materials with a large  $ZT$  of 1.5–2. The other strategy is an enhancement of the product  $S^2 \cdot \sigma$ , which is called the power factor (PF). However, it is extremely difficult to enhance PF due to the trade-off relationship between  $S$  and the carrier concentration ( $n$ ). Therefore, PF has a local maximum value in three-dimensional bulk systems.

In a two-dimensional electron system (2DES) such as metal/insulator superlattices, carrier electrons are confined within a thin layer (thickness  $<$  de Broglie wavelength,  $\lambda_D$ ). 2DES is an efficient strategy to achieve an enhanced PF [Fig. 4.1(a)]. The effectiveness

of 2DES was theoretically predicted by Hicks and Dresselhaus in 1993;<sup>9</sup> 2DES in extremely narrow layers exhibits an enhanced  $S$  without reducing  $\sigma$  because the DOS near the bottom of the conduction band increases as the 2DES layer thickness decreases. These layers are narrower than the  $\lambda_D$ ,

$$\lambda_D = \frac{h}{\sqrt{3 \cdot m^* \cdot k_B \cdot T}} \quad (4-1)$$

, where  $h$ ,  $m^*$ , and  $k_B$  are Planck's constant, effective mass of conductive electron or hole, and Boltzmann constant, respectively<sup>9-13</sup>.

Many experimental studies have been made to clarify the effectiveness of 2DES to enhance PF using PbTe/Pb<sub>1-x</sub>Eu<sub>x</sub>Te multiple-quantum-well,<sup>10</sup> electron-doped SrTiO<sub>3</sub> based superlattices,<sup>14,15</sup> SiGe based superlattices,<sup>16,17</sup> and Bi<sub>2</sub>Te<sub>3</sub>-based superlattices<sup>18</sup>. These 2DES layers showed enhanced  $S$ . However, total enhancement of PF was very small because of the insulator layer thickness. Thus, the effectiveness of 2DES has not been experimentally clarified thus far. In order to enhance total PF of 2DES, two-dimensionality should be enhanced. Use of longer  $\lambda_D$  should be effective if the carrier electrons are confined within a defined thickness layer [Fig. 4.1(b)].

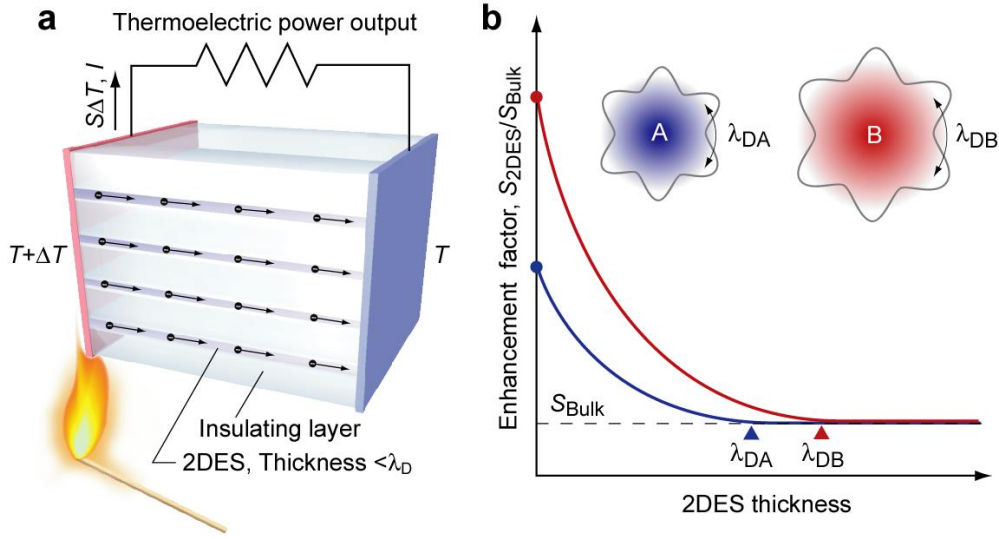


**Figure 4.1.** Thermoelectric effect of a 2D electron system. (a) Schematic illustration of thermoelectric Seebeck effect in a 2DES. Thermoelectric power output ( $= S \cdot \Delta T \cdot I$ ) can be obtained when  $\Delta T$  is introduced. (b) The hypothesis that a 2DES with longer de Broglie wavelength ( $\lambda_D$ ) shows a larger enhanced factor of thermopower.

In the previous chapter, we observed a steep decrease in  $m^*/m_e$  at  $x \sim 0.3$  in  $\text{SrTiO}_3$ - $\text{SrNbO}_3$  solid solution system,  $\text{SrTi}_{1-x}\text{Nb}_x\text{O}_3$  ( $0.05 \leq x \leq 0.9$ ) (Fig. 4.2)<sup>19</sup>. The  $\text{SrTi}_{1-x}\text{Nb}_x\text{O}_3$  can be divided into two regions, Region A ( $x < 0.3$ ) and Region B ( $x > 0.3$ ). The origin of two regions is most likely due to the difference in the overlap population between the Ti 3d and Nb 4d orbitals ( $r_{\text{Ti}3d} = 48.9$  pm and  $r_{\text{Nb}4d} = 74.7$  pm)<sup>20</sup>.  $\lambda_D$  values of  $\text{SrTi}_{1-x}\text{Nb}_x\text{O}_3$  ( $0.05 \leq x \leq 0.9$ ) were calculated using the equation (4-1). The  $\lambda_D$  value in Region B is  $\sim 5.2$  nm, which is 27% longer than that in Region A ( $\sim 4.1$  nm). One can expect that  $S$ -enhancement factor in Region B is much higher than that in Region A because of higher two-dimensionality. Therefore, it could be hypothesized that  $\text{SrTi}_{1-x}\text{Nb}_x\text{O}_3$  based 2DES can be used to clarify the effectiveness of 2DES to enhance PF experimentally.

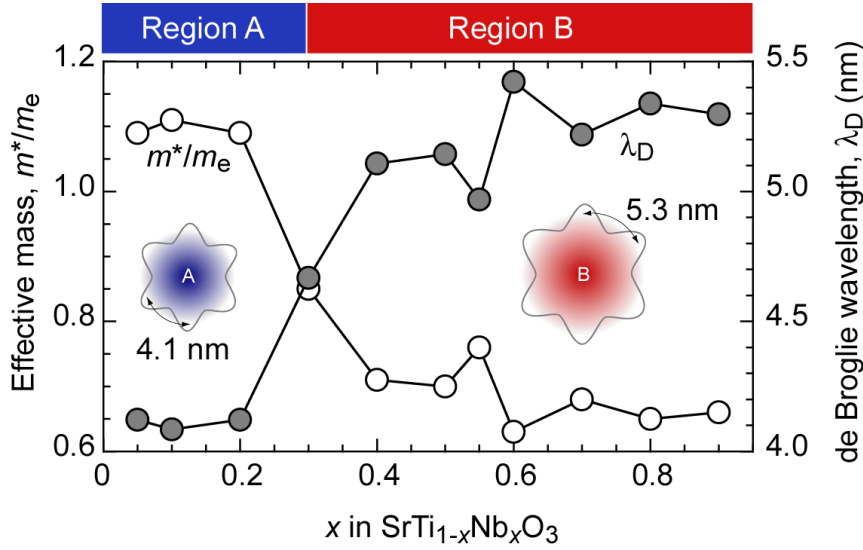


**Figure 4.2.**  $\text{SrTiO}_3$ - $\text{SrNbO}_3$  solid-solution: A model system having two different  $\lambda_D$ .  $x$  dependent effective mass ( $m^*/m_e$ , white symbols) and  $\lambda_D$  (grey symbols) for  $\text{SrTi}_{1-x}\text{Nb}_x\text{O}_3$  solid solutions.  $m^*/m_e$  exerts a decreasing tendency with  $x$ , resulting in an increased  $\lambda_D$ . Sharp changes in both  $m^*/m_e$  and  $\lambda_D$  are detected around  $x = 0.3$  due to the conduction band transition from Ti 3d to Nb 4d.  $\text{SrTi}_{1-x}\text{Nb}_x\text{O}_3$  solid solutions can be divided into two regions based on the conduction bands (Ti 3d  $\rightarrow$  Region A and Nb 4d  $\rightarrow$  Region B). Inset: Schematic illustrations of conduction electrons at Region A and B. At Region B,  $\lambda_D$  is  $\sim 5.3$  nm, while it is  $\sim 4.1$  nm at Region A.

In this chapter, it has been clarified that an enhanced two-dimensionality of 2DES is efficient to enhance thermoelectric PF. As a 2DES, we measured thermoelectric properties of  $[N \text{ uc SrTi}_{1-x}\text{Nb}_x\text{O}_3|11 \text{ uc SrTiO}_3]_{10}$  superlattices ( $1 \leq N \leq 12$ ,  $x = 0.2-0.9$ ). The  $S$ -enhancement factor  $S_{2\text{DES}}/S_{\text{Bulk}}$  of the 2DES ( $N = 1$ ) for  $x > 0.3$  were  $\sim 10$ , whereas those for  $x < 0.3$  were 4–5. Maximum PF of the 2DES ( $N = 1$ ,  $x = 0.6$ ) exceeded  $\sim 5 \text{ mW m}^{-1} \text{ K}^{-2}$ , which doubles the value of optimized bulk  $\text{SrTi}_{1-x}\text{Nb}_x\text{O}_3$  (PF  $\sim 2.5 \text{ mW m}^{-1} \text{ K}^{-2}$ ). The present 2DES approach ‘Use of longer  $\lambda_D$ ’ is epoch-making and is fruitful to design

good thermoelectric materials showing high PF.

## 4.2 Experimental

### Fabrication and analyses of the 2DESs

A series of superlattices with the chemical formula of [*N* uc SrTi<sub>1-x</sub>Nb<sub>x</sub>O<sub>3</sub> | 11 uc SrTiO<sub>3</sub>]<sub>10</sub> ( $1 \leq N \leq 12$ ,  $x = 0.2-0.9$ ) were fabricated by a pulsed laser deposition (PLD) technique using dense ceramic disks of a SrTiO<sub>3</sub>-SrNbO<sub>3</sub> mixture and a SrTiO<sub>3</sub> single crystal as the targets. The substrate was insulating (001) LaAlO<sub>3</sub> (pseudo-cubic perovskite,  $a = 3.79 \text{ \AA}$ , The surface area:  $1 \text{ cm} \times 1 \text{ cm}$ ). The growth conditions were precisely controlled. The substrate temperature was 900 °C, the oxygen pressure was  $\sim 10^{-4}$  Pa, and the laser fluence was  $\sim 1.2 \text{ J cm}^{-2} \text{ pulse}^{-1}$ . The thicknesses of different layers were monitored in-situ using the intensity oscillation of the reflection high-energy electron diffraction (RHEED) spots. Details of our PLD growth process of the superlattices are reported elsewhere<sup>14,21</sup>.

Crystallographic analyses of the resultant superlattices were performed by X-ray diffraction (XRD, Cu K $\alpha$ <sub>1</sub>, ATX-G, Rigaku Co.), atomic force microscopy (AFM, Nanoscope, Hitachi Hi-Tech), and scanning transmission electron microscopy (STEM, 200 keV, JEM-ARM 200CF, JEOL Co. Ltd). TEM samples were fabricated using a cryo ion slicer (IB-09060CIS, JEOL Co. Ltd). High-angle annular dark-field (HAADF) images were taken with the detection angle of 68–280 mrad. Electron energy loss spectra (EELS) were acquired in STEM mode with the energy resolution of 0.8 eV.

### **Measurements of the thermoelectric properties of the 2DESs**

Electrical conductivity ( $\sigma$ ), carrier concentration ( $n$ ), and Hall mobility ( $\mu_{\text{Hall}}$ ) were measured at room temperature by a conventional d.c. four-probe method with a van der Pauw geometry.  $S$  was measured at room temperature by creating a temperature difference ( $\Delta T$ ) of  $\sim 4$  K across the film using two Peltier devices. (Two small thermocouples were used to monitor the actual temperatures of each end of a superlattice.) The thermoelectromotive force ( $\Delta V$ ) and  $\Delta T$  were measured simultaneously, and the  $S$ -values were obtained from the slope of the  $\Delta V$ - $\Delta T$  plots (The correlation coefficient:  $> 0.9999$ ).

Cross-plane thermal conductivity ( $\kappa$ ) was measured by time-domain thermoreflectance (TDTR, Picotherm Co.) method. Mode-locked fiber pulse lasers with 1550 nm and 775 nm wavelengths were used for heating and measuring, respectively. Both lasers are with the repetition frequency of 20 MHz and pulse duration of 0.4 ps. Before measurement, Mo film with a thickness of 100 nm was firstly deposited on the surface of the sample as the transducer. During measurement, time-dependent transient thermoreflectance phase signal of Mo transducer was measured, from which  $\kappa$  was further simulated. Time-domain thermoreflectance was measured based on amplified laser systems (5 kHz and  $\sim 200$  fs centered at 1030 nm). Degenerate pump and probe photons were separated by the cross polarization, and a polarizing filter was employed before the lock-in detection. A mechanical delay stage was used for time scan up to 1.5 ns. Pump to probe intensity ratio was greater than 15, and the size ratio was around 6.

## **Energy band calculation of the 2DES**

Band structure for the [1 uc SrNbO<sub>3</sub>|10 uc SrTiO<sub>3</sub>] superlattice was calculated based on the projector augmented-wave (PAW) method,<sup>22</sup> as implemented in the VASP code<sup>23,24</sup>. We adopted the Heyd-Scuseria-Ernzerhof (HSE) hybrid functionals<sup>25-27</sup> and a plane-wave cutoff energy of 550 eV. 6×6×6 and 6×6×2 *k*-point meshes were employed in the total-energy evaluations and geometry optimization for the perovskite unit cells of SrTiO<sub>3</sub> and the superlattice cell, respectively. The in-plane lattice constant of the superlattice cell was fixed at the optimized value of SrTiO<sub>3</sub> while the out-of-plane lattice constant and the atomic coordinates were fully relaxed.

### **4.3 Results and discussion**

We fabricated [*N* uc SrTi<sub>1-x</sub>Nb<sub>x</sub>O<sub>3</sub>|11 uc SrTiO<sub>3</sub>]<sub>10</sub> superlattices (1 ≤ *N* ≤ 12, *x* = 0.2–0.9) by a pulsed laser deposition (PLD) technique on insulating (001) LaAlO<sub>3</sub> (pseudo-cubic perovskite, *a* = 3.79 Å) single crystal substrates using dense ceramic disks of a SrTiO<sub>3</sub>–SrNbO<sub>3</sub> mixture and SrTiO<sub>3</sub> single crystal as the targets. The thicknesses of different layers were monitored in-situ using the intensity oscillation of the reflection high-energy electron diffraction (RHEED) spots. High-resolution X-ray diffraction (XRD) measurements revealed that the resultant superlattices were heteroepitaxially grown on (001) LaAlO<sub>3</sub> with cube-on-cube epitaxial relationship with superlattice structure. Atomically smooth surfaces with stepped and terraced structure were observed by an atomic force microscopy (AFM).

Fig. 4.3 shows out-of-plane XRD patterns for  $[1 \text{ uc SrTi}_{1-x}\text{Nb}_x\text{O}_3|11 \text{ uc SrTiO}_3]_{10}$  ( $0.6 \leq x \leq 0.9$ ) superlattices. Diffraction peaks from (002) plane of both superlattices and  $\text{LaAlO}_3$  substrate could be observed. All the samples have been fully relaxed along the out-of-plane direction. And in addition to the main peaks from the superlattices, we can also observe the satellite peaks from the superlattice structures, indicating sharp interface between Nb substituted layer and  $\text{SrTiO}_3$  barrier layers and also the high quality of our superlattices.

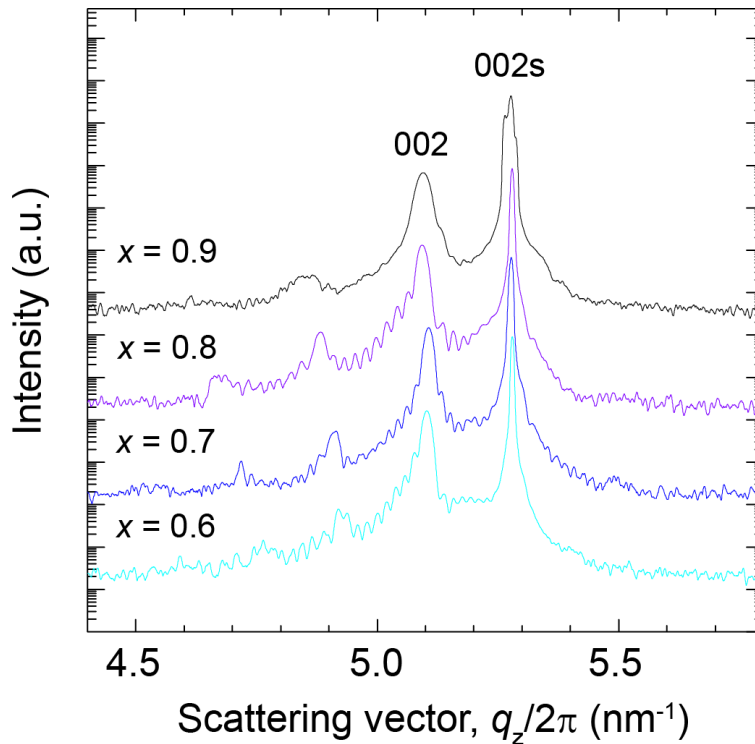


**Figure 4.3.** Out-of-plane XRD patterns for  $[1 \text{ uc SrTi}_{1-x}\text{Nb}_x\text{O}_3|11 \text{ uc SrTiO}_3]_{10}$  ( $0.6 \leq x \leq 0.9$ ) superlattices. All the superlattices show full relaxed lattice along the out-of-plane direction. Obvious satellite peaks from superlattice structure could be observed for all the samples indicating sharp interface between Nb substituted layer and  $\text{SrTiO}_3$  barrier layers.

Fig. 4.4(a) summarizes the atomic arrangements of the [1 uc  $\text{SrTi}_{0.4}\text{Nb}_{0.6}\text{O}_3$ |11 uc  $\text{SrTiO}_3$ ]<sub>10</sub> superlattice. Rather bright bands are observed near each  $\text{SrTi}_{0.4}\text{Nb}_{0.6}\text{O}_3$  layer in the Cs-corrected high-angle annular dark-field scanning transmission electron microscopy (HAADF-STEM) image (left). In the magnified image (center), the #4 atom in the B-site column is brighter than nearby atoms. However, there is no obvious difference in the A-site column, indicating Nb substitution occurs for the #4 atom in the B-site column. The electron energy loss spectroscopy (EELS) signal (right) of #4 is broader than those of nearby atoms, implying the coexistence of  $\text{Ti}^{4+}/\text{Ti}^{3+}$  in the  $\text{SrTi}_{0.4}\text{Nb}_{0.6}\text{O}_3$  layers.<sup>28</sup> Therefore, in our superlattice fabrication, Nb ions are successfully confined into the 1 uc  $\text{SrTi}_{0.4}\text{Nb}_{0.6}\text{O}_3$  layers.<sup>29</sup>

In order to clarify the 2DES formation, the electronic band structures of the [1 uc  $\text{SrNbO}_3$ |10 uc  $\text{SrTiO}_3$ ] superlattices were calculated based on the projector augmented-wave (PAW) method [Fig. 4.4(b)]. The  $E_F$  is located on the higher energy side of the conduction band minimum for the 1<sup>st</sup> and 2<sup>nd</sup> nearest neighbor  $\text{SrTiO}_3$  layers (Ti 1<sup>st</sup> NN and Ti 2<sup>nd</sup> NN) together with the 1 uc  $\text{SrNbO}_3$  layer (Nb) (left). The carrier electrons can seep from the  $\text{SrNbO}_3$  layers into the  $\text{SrTiO}_3$  layer (right). Delugas *et al.* have also predicted theoretically that for lower Nb substituted samples, it is much easier for the electrons, especially in the  $d_{xz}$  and  $d_{yz}$  bands, to spill into the neighboring  $\text{SrTiO}_3$  layers and deteriorate the two-dimensionality.<sup>30</sup> However, as the Nb content increases, the minimum barrier layer thickness may be reduced to 5 uc in the  $\text{SrNbO}_3$  case. There is no doubt that the electron exudation cannot be removed thoroughly in superlattice structure, but exudation effects can be effectively suppressed by the high Nb substitution. From the band calculation, 2DES in our work is mainly confined to the 1 uc  $\text{SrTi}_{1-x}\text{Nb}_x\text{O}_3$  layers and should contribute to the  $S$  enhancement.

4. Fabrication and Thermoelectric Properties of  $\text{SrTi}_{1-x}\text{Nb}_x\text{O}_3/\text{SrTiO}_3$  ( $0.1 \leq x \leq 0.9$ ) Superlattices

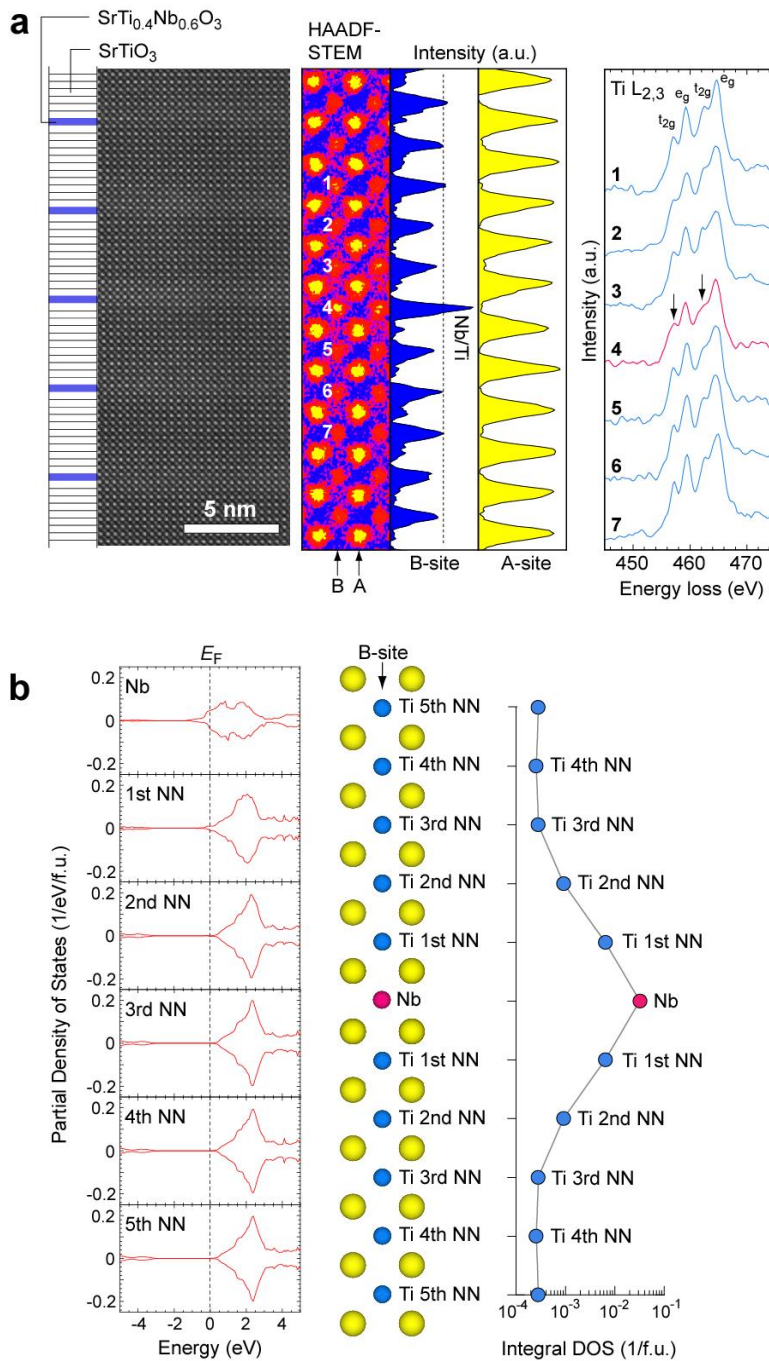


**Figure 4.4.** Experimental and theoretical analyses of the 2DES. (a) Cross-sectional HAADF-STEM image of the  $[1 \text{ uc SrTi}_{0.4}\text{Nb}_{0.6}\text{O}_3|11 \text{ uc SrTiO}_3]_{10}$  superlattice (left). Layer stacking sequence is also shown. Rather bright bands are seen near each  $\text{SrTi}_{0.4}\text{Nb}_{0.6}\text{O}_3$  layer. In the magnified image (center), the #4 atom in the B-site column is

brighter than nearby atoms, whereas no obvious difference is observed in the A-site column. EELS spectrum (right) of #4 is broader than that of nearby atoms, indicating the co-existence of Ti<sup>4+</sup>/Ti<sup>3+</sup> in the SrTi<sub>0.4</sub>Nb<sub>0.6</sub>O<sub>3</sub> layers. (b) Calculated partial DOS of Nb 4d or Ti 3d in the [1 uc SrNbO<sub>3</sub>|10 uc SrTiO<sub>3</sub>] superlattice (left). Fermi energy ( $E_F$ ) is located on the higher energy side of the conduction band minimum for the 1<sup>st</sup> and 2<sup>nd</sup> nearest neighbor (Ti 1<sup>st</sup> NN and Ti 2<sup>nd</sup> NN) SrTiO<sub>3</sub> layers together with 1 uc SrNbO<sub>3</sub> layer (Nb) suggest that the carrier electrons can seep from the SrTi<sub>1-x</sub>Nb<sub>x</sub>O<sub>3</sub> layers into the SrTiO<sub>3</sub> layers (right).

In order to further confirm the superlattice structure, we measured the  $\kappa$  of the [1 uc SrTi<sub>0.4</sub>Nb<sub>0.6</sub>O<sub>3</sub>|11 uc SrTiO<sub>3</sub>]<sub>10</sub> superlattice along the cross-plane direction by time-domain thermal reflectance (TDTR) method. The total  $\kappa$  could be suppressed to ~3.3 W m<sup>-1</sup> K<sup>-1</sup>, similar to the minimum value of CaTiO<sub>3</sub>/SrTiO<sub>3</sub> based superlattices ( $\kappa$  ~3.2 W m<sup>-1</sup> K<sup>-1</sup>) reported by Ravichandran *et al.*<sup>31</sup> From these results, we judged that our [ $N$  uc SrTi<sub>1-x</sub>Nb<sub>x</sub>O<sub>3</sub>|11 uc SrTiO<sub>3</sub>]<sub>10</sub> superlattices (1 ≤  $N$  ≤ 12,  $x$  = 0.2–0.9) are appropriate to clarify the effectiveness of 2DES to enhance PF.

The electrical conductivity ( $\sigma$ ), carrier concentration ( $n$ ), and Hall mobility ( $\mu_{\text{Hall}}$ ) of the superlattices were measured at room temperature by a conventional d.c. four-probe method with a van der Pauw geometry.  $S$  was measured at room temperature by creating a temperature difference ( $\Delta T$ ) of ~4 K across the film using two Peltier devices. Fig. 4.5(a) summarizes the  $n$  dependent  $S$  of [ $N$  uc SrTi<sub>1-x</sub>Nb<sub>x</sub>O<sub>3</sub>|11 uc SrTiO<sub>3</sub>]<sub>10</sub> superlattices (1 ≤  $N$  ≤ 12,  $x$  = 0.2, 0.3, and 0.8) along with bulk (~100-nm-thick SrTi<sub>1-x</sub>Nb<sub>x</sub>O<sub>3</sub> films with  $x$  = 0.2, 0.3, and 0.8, respectively) values for comparison. The bulk  $S$  for  $x$  = 0.2 was -143  $\mu\text{V K}^{-1}$ ,  $x$  = 0.3 was -73  $\mu\text{V K}^{-1}$ , and  $x$  = 0.8 was -19  $\mu\text{V K}^{-1}$ , respectively. The  $n$  value

#### 4. Fabrication and Thermoelectric Properties of SrTi<sub>1-x</sub>Nb<sub>x</sub>O<sub>3</sub>/SrTiO<sub>3</sub> (0.1 ≤ x ≤ 0.9) Superlattices

was measured based on the total thickness of the 2DES, which includes the insulating SrTiO<sub>3</sub> layers. All the 2DESs show enhanced thermopower ( $-S$ ) with a reduced  $N$ . Compared to the bulk samples at a similar  $n$ , a much higher  $-S$  is observed in superlattices as  $N$  is reduced below 3 uc.

To confirm the increasing two-dimensionality with  $x$ , the  $S$ -enhancement factors ( $S_{2DES}/S_{Bulk}$ ) were plotted versus the  $N$  values [Fig. 4.5(b)]. For 2DES with  $x = 0.2$  and 0.3, the highest  $S_{2DES}/S_{Bulk}$  values are around 4 and 5, respectively, whereas that for the  $x = 0.8$  counterpart is  $\sim 10$ . As hypothesized, the enhanced  $S_{2DES}/S_{Bulk}$  should stem from the increasing  $\lambda_D$  with  $x$ . In our experiment,  $S_{2DES}/S_{Bulk}$  for the  $x = 0.2$  and 0.3 2DESs are saturated around 11 uc, which is consistent with  $\lambda_D$  in Region A ( $\sim 4.2$  nm indicated by dashed line  $\lambda_{DA}$ ). As  $\lambda_D$  increases in Region B, the saturation position for the  $x = 0.8$  2DES has a thickness larger than the  $\lambda_D$  ( $\sim 5.2$  nm indicated by dashed line  $\lambda_{DB}$ ). As a result, an obviously enhanced two-dimensionality is achieved in the  $x > 0.3$  Region B, which fits well with our hypothesis and suggests that Region B has the potential to further enhance the thermoelectric PF.

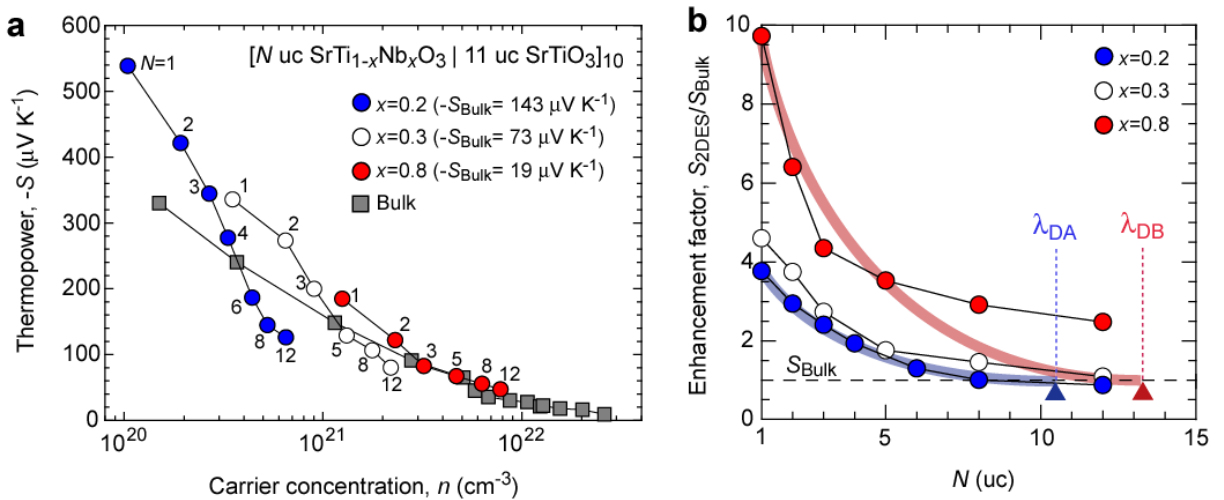


**Figure 4.5.** Two-dimensionality of 2DES: A key to enhance thermopower. (a) Plots of thermopower of the 2DESs, [N uc SrTi<sub>1-x</sub>Nb<sub>x</sub>O<sub>3</sub>|11 uc SrTiO<sub>3</sub>]<sub>10</sub> superlattices (x = 0.2, 0.3, and 0.8), vs. the carrier concentration (n). Compared to bulk values (gray squares), all the 2DESs show an enhanced -S as N is reduced under 3 uc. (b) Enhancement factors in -S (S<sub>2DES</sub>/S<sub>Bulk</sub>) for three sets of 2DESs. For x = 0.2 and 0.3 2DESs, the highest S<sub>2DES</sub>/S<sub>Bulk</sub> values are obtained at N = 1, which are 4 and 5, respectively, while that of x = 0.8 can reach 10.

Based on the conclusions above, we tried to enhance the thermoelectric PF in [1 uc SrTi<sub>1-x</sub>Nb<sub>x</sub>O<sub>3</sub>|11 uc SrTiO<sub>3</sub>]<sub>10</sub> superlattices by adjusting x between x = 0.2–0.9. Fig. 4.6 summarizes the n dependences of the thermoelectric properties of [1 uc SrTi<sub>1-x</sub>Nb<sub>x</sub>O<sub>3</sub>|11 uc SrTiO<sub>3</sub>]<sub>10</sub> superlattices at room temperature along with the reported bulk values for comparison.<sup>19</sup> Following the bulk values, σ increases almost linearly with n [Fig. 4.6(a)], indicating that n dominates σ. In the SrTi<sub>1-x</sub>Nb<sub>x</sub>O<sub>3</sub> system, carriers are mostly due to Nb substitution. The high n also induces a highly Nb substituted region with a superiority in σ. However, σ for the superlattices remains lower than the bulk value due to the coexistence of 11 uc SrTiO<sub>3</sub> insulating layers.

μ<sub>Hall</sub> for lower x 2DESs (x ≤ 0.5) fluctuates around 3–5 cm<sup>2</sup> V<sup>-1</sup> s<sup>-1</sup>, while for higher x 2DESs (x ≥ 0.6) values are ~6 cm<sup>2</sup> V<sup>-1</sup> s<sup>-1</sup> [Fig. 4.6(b)]. Usually, μ<sub>Hall</sub> is controlled by the conduction band of materials along with the effects of crystal defects such as impurities and grain boundaries. In the bulk samples, μ<sub>Hall</sub> sharply increases due to the transition of the conduction band from Ti 3d to Nb 4d as x increases into the highly Nb substituted region.<sup>19</sup> This pattern is also conserved in the superlattice counterparts. A higher μ<sub>Hall</sub> (≥ 6 cm<sup>2</sup> V<sup>-1</sup> s<sup>-1</sup>) is observed in samples with x ≥ 0.6 than that for x ≤ 0.5 (3–5 cm<sup>2</sup> V<sup>-1</sup> s<sup>-1</sup>).

Compared to the bulk samples, all the superlattices exert a much lower  $\mu_{\text{Hall}}$ , which may result from an insufficient crystal quality or electron exudation into the pure SrTiO<sub>3</sub> barrier layers. Regardless, a conduction band transition from Ti 3d to Nb 4d is recognized in our superlattice systems. Due to the high overlapping population of the Nb 4d orbital, a superior electron transport property is realized in higher  $x$  2DES.

**Fig. 4.6(c)** plots the  $S$  values for all the superlattices versus  $n$  along with reported bulk values.<sup>19</sup> The solid line depicts the overall tendency. In the diagram, the superlattices have an obviously enhanced  $-S$  compared to bulk samples at similar  $n$  values. As indicated by the solid lines, the experimental points for 2DES and bulk show different slopes of  $-300 \mu\text{V K}^{-1} \text{ decade}^{-1}$  and  $-200 \mu\text{V K}^{-1} \text{ decade}^{-1}$ , respectively. The relationship between  $-S$  and  $n_{\text{eff}}$  can be expressed by the following equation

$$-S = -k_{\text{B}}/e \cdot \ln 10 \cdot A \cdot (\log n + B) \quad (4-2)$$

, where  $k_{\text{B}}$  is the Boltzmann constant and  $e$  is an electron charge.  $A$  and  $B$  are the parameters that depend on the type of materials and their electronic band structures. Bulk shows a 3D electronic band structure with a parabolic shaped DOS near  $E_{\text{F}}$ , where the  $A$  value is equal to 1 and the slope reflects a constant value of  $-k_{\text{B}}/e \cdot \ln 10$  ( $\equiv -198 \mu\text{V K}^{-1}$ ). On the other hand, the slope of the 2DESs may reach  $-300 \mu\text{V K}^{-1} \text{ decade}^{-1}$ , indicating that the  $A$  value is equal to 1.5. Therefore, the 2DESs work well to enhance the  $S$  even for the whole superlattice including SrTiO<sub>3</sub> insulating layers.

Finally, we calculated PF of the [1 uc SrTi<sub>1-x</sub>Nb<sub>x</sub>O<sub>3</sub>|11 uc SrTiO<sub>3</sub>]<sub>10</sub> superlattices ( $x = 0.2-0.9$ ) using the observed  $S$  and  $\sigma$  values [**Fig. 4.6(d)**]. PF is doubly enhanced for  $x = 0.6$  ( $5.1 \text{ mW m}^{-1} \text{ K}^{-2}$  at  $n \sim 8 \times 10^{20} \text{ cm}^{-3}$ ). Since the PF values are scattered due to the rather large distribution of  $\mu_{\text{Hall}}$  ( $3-6 \text{ cm}^2 \text{ V}^{-1} \text{ s}^{-1}$ ), we calculated PFs using the relationship between  $S$  and  $n$  (c) at constant  $\mu_{\text{Hall}}$  ( $6 \text{ cm}^2 \text{ V}^{-1} \text{ s}^{-1}$ ). The optimized PF of the 2DES should

be  $\sim 5 \text{ mW m}^{-1} \text{ K}^{-2}$  at  $n \sim 8 \times 10^{20} \text{ cm}^{-3}$ , which doubles that of bulk  $\text{SrTi}_{1-x}\text{Nb}_x\text{O}_3$  ( $PF \sim 2.5 \text{ mW m}^{-1} \text{ K}^{-2}$  at  $n \sim 2 \times 10^{21} \text{ cm}^{-3}$ ).

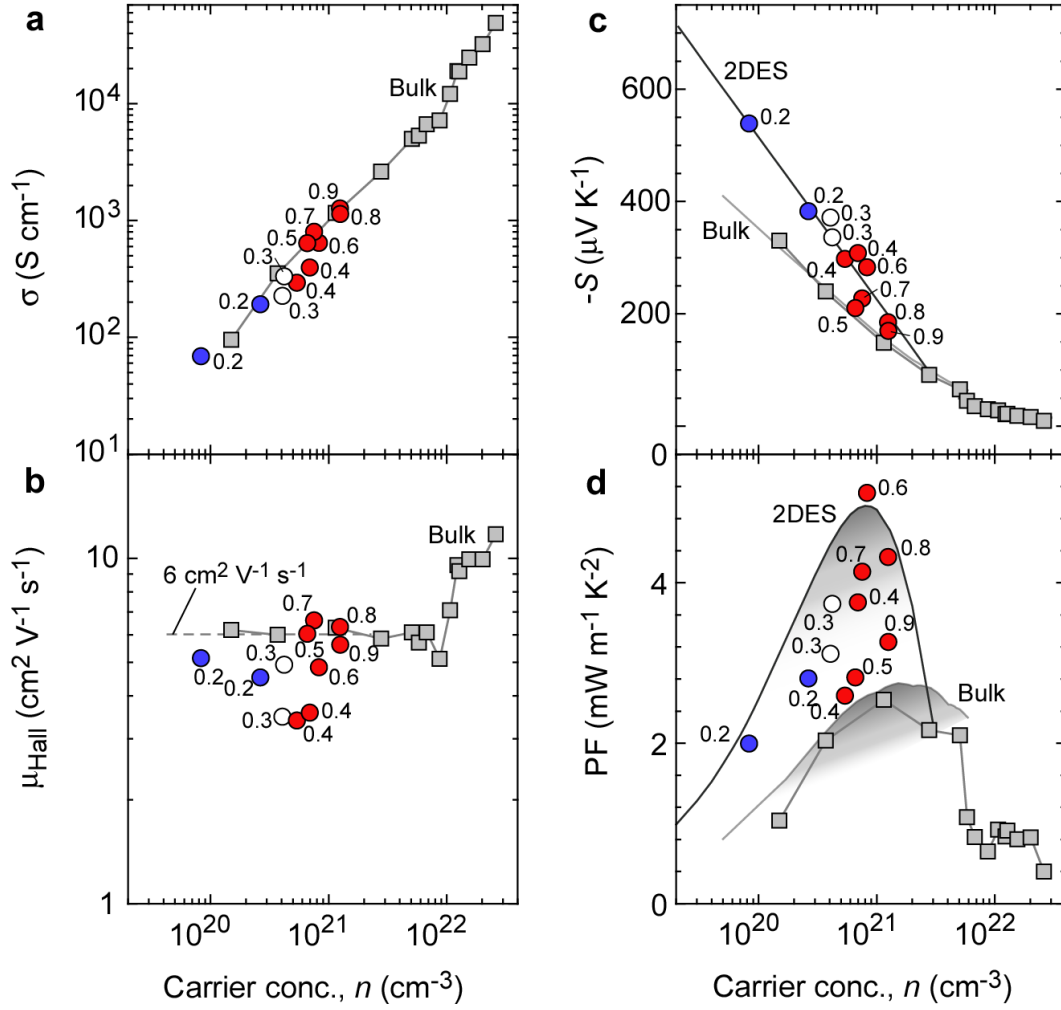


**Figure 4.6.** Double enhancement of the thermoelectric power factor in a 2DES. Carrier concentration dependences of (a) Electrical conductivity ( $\sigma$ ), (b) Hall mobility ( $\mu_{\text{Hall}}$ ), (c) thermopower ( $-S$ ), and (d) power factor [ $PF$  ( $S^2 \cdot \sigma$ )] of [1 uc  $\text{SrTi}_{1-x}\text{Nb}_x\text{O}_3$  | 11 uc  $\text{SrTiO}_3$ ] $_{10}$  2DESs ( $x = 0.2-0.9$ ) at room temperature. Similar to the trends in the bulk values,  $\sigma$  increases almost linearly with  $n$ .  $\mu_{\text{Hall}}$  for lower  $x$  samples ( $x \leq 0.5$ ) fluctuates around  $3-5 \text{ cm}^2 \text{ V}^{-1} \text{ s}^{-1}$ , while that for higher  $x$  ones ( $x \geq 0.6$ ) is  $\sim 6 \text{ cm}^2 \text{ V}^{-1} \text{ s}^{-1}$ . Slope of

$-S$  vs.  $\log n$  for bulk SrTi<sub>1-x</sub>Nb<sub>x</sub>O<sub>3</sub> is  $-198 \mu\text{V K}^{-1}$ , which  $\sim 1.5$  times lower than  $-300 \mu\text{V K}^{-1}$  for the 2DESs. Double enhancement of PF is seen in  $x = 0.6$  ( $5.1 \text{ mW m}^{-1} \text{ K}^{-2}$  at  $n \sim 8 \times 10^{20} \text{ cm}^{-3}$ ). Since the PF values are scattered due to the rather large distribution of  $\mu_{\text{Hall}}$  ( $3\text{--}6 \text{ cm}^2 \text{ V}^{-1} \text{ s}^{-1}$ ), we calculated PFs using the relationship between  $S$  and  $n$  (c) at constant  $\mu_{\text{Hall}}$  ( $6 \text{ cm}^2 \text{ V}^{-1} \text{ s}^{-1}$ ). The optimized PF of the 2DES should be  $\sim 5 \text{ mW m}^{-1} \text{ K}^{-2}$  at  $n \sim 8 \times 10^{20} \text{ cm}^{-3}$ , which is double that of bulk SrTi<sub>1-x</sub>Nb<sub>x</sub>O<sub>3</sub> ( $PF \sim 2.5 \text{ mW m}^{-1} \text{ K}^{-2}$  at  $n \sim 2 \times 10^{21} \text{ cm}^{-3}$ ).

The present 2DES, [1 uc SrTi<sub>1-x</sub>Nb<sub>x</sub>O<sub>3</sub>|11 uc SrTiO<sub>3</sub>]<sub>10</sub> superlattices ( $x = 0.2\text{--}0.9$ ), has several merits to enhance PF as compared with other 2DESs such as PbTe/Pb<sub>1-x</sub>Eu<sub>x</sub>Te multiple-quantum-well,<sup>10</sup> SiGe based superlattices,<sup>16,17</sup> and Bi<sub>2</sub>Te<sub>3</sub>-based superlattices,<sup>18</sup> which are already commercialized thermoelectric materials. This is because SrTi<sub>1-x</sub>Nb<sub>x</sub>O<sub>3</sub> can be deposited with 1 uc layer accuracy by PLD. Therefore, we can easily reduce the 2DEG thickness to  $\sim 0.4 \text{ nm}$  (1 uc layer). Further, there are two different  $\lambda_{\text{D}}$  in SrTi<sub>1-x</sub>Nb<sub>x</sub>O<sub>3</sub>;  $\sim 4.1 \text{ nm}$  in the low conducting region and  $\sim 5.2 \text{ nm}$  in the high conducting region. In enhancing PF, both  $S$  and  $\sigma$  play important roles. The present research implies that high conducting region is effective to enhance the thermoelectric PF in the 2DES. Herein highly Nb substitution realizes the coexistence of both a high electron transport (high  $n$  and  $\mu_{\text{Hall}}$ ) and a high two-dimensionality (large  $\lambda_{\text{D}}$ ).

#### 4.4 Conclusion

In summary, we have experimentally clarified that an enhanced two-dimensionality of 2DES is efficient to enhance thermoelectric PF. We measured the thermoelectric

properties of 2DESs [*N* uc SrTi<sub>1-x</sub>Nb<sub>x</sub>O<sub>3</sub>|11 uc SrTiO<sub>3</sub>]<sub>10</sub> superlattices (1 ≤ *N* ≤ 12, *x* = 0.2–0.9) because there are two different  $\lambda_D$  in this 2DES (*x* > 0.3:  $\lambda_D \sim 5.2$  nm, *x* < 0.3:  $\lambda_D \sim 4.1$  nm). The *S*-enhancement factor  $S_{2DES}/S_{Bulk}$  of the 2DES (*N* = 1) for *x* > 0.3 were  $\sim 10$ , whereas those for *x* < 0.3 were 4–5. Maximum PF of the 2DES (*N* = 1, *x* = 0.6) exceeded  $\sim 5$  mW m<sup>-1</sup> K<sup>-2</sup>, which doubles the value of optimized bulk SrTi<sub>1-x</sub>Nb<sub>x</sub>O<sub>3</sub> (PF  $\sim 2.5$  mW m<sup>-1</sup> K<sup>-2</sup>). The present 2DES approach ‘Use of longer  $\lambda_D$ ’ is epoch-making and is fruitful to design good thermoelectric materials showing high PF.

## References

- 1 DiSalvo, F. J. Thermoelectric cooling and power generation. *Science* **285**, 703-706 (1999).
- 2 Snyder, G. J. & Toberer, E. S. Complex thermoelectric materials. *Nature Materials* **7**, 105-114 (2008).
- 3 Vining, C. B. An inconvenient truth about thermoelectrics. *Nature Mater.* **8**, 83-85 (2009).
- 4 Zhang, Q. H. *et al.* Thermoelectric Devices for Power Generation: Recent Progress and Future Challenges. *Adv. Eng. Mater.* **18**, 194-213 (2016).
- 5 Hsu, K. F. *et al.* Cubic AgPb<sub>m</sub>SbTe<sub>2+m</sub>: Bulk thermoelectric materials with high figure of merit. *Science* **303**, 818-821 (2004).
- 6 Poudel, B. *et al.* High-thermoelectric performance of nanostructured bismuth antimony telluride bulk alloys. *Science* **320**, 634-638 (2008).
- 7 Il Kim, S. *et al.* Dense dislocation arrays embedded in grain boundaries for high-performance bulk thermoelectrics. *Science* **348**, 109-114 (2015).
- 8 Biswas, K. *et al.* High-performance bulk thermoelectrics with all-scale hierarchical architectures. *Nature* **489**, 414-418 (2012).
- 9 Hicks, L. D. & Dresselhaus, M. S. Effect of quantum-well structures on the thermoelectric figure of merit. *Phys. Rev. B* **47**, 12727-12731 (1993).
- 10 Hicks, L. D., Harman, T. C., Sun, X. & Dresselhaus, M. S. Experimental study of the effect of quantum-well structures on the thermoelectric figure of merit. *Phys Rev B* **53**, 10493-10496 (1996).

- 11 Hung, N. T., Hasdeo, E. H., Nugraha, A. R. T., Dresselhaus, M. S. & Saito, R. Quantum Effects in the Thermoelectric Power Factor of Low-Dimensional Semiconductors. *Phys Rev Lett* **117**, 036602, doi:Artn 036602 10.1103/Physrevlett.117.036602 (2016).
- 12 Mao, J., Liu, Z. H. & Ren, Z. F. Size effect in thermoelectric materials. *Npj Quantum Mater* **1**, 16028 (2016).
- 13 Hung, N. T., Nugraha, A. R. T. & Saito, R. Two-dimensional InSe as a potential thermoelectric material. *Appl. Phys. Lett.* **111**, 092107 (2017).
- 14 Ohta, H. *et al.* Giant thermoelectric Seebeck coefficient of two-dimensional electron gas in SrTiO<sub>3</sub>. *Nature Materials* **6**, 129-134 (2007).
- 15 Choi, W. S., Ohta, H. & Lee, H. N. Thermopower enhancement by fractional layer control in 2D oxide superlattices. *Adv Mater* **26**, 6701-6705 (2014).
- 16 Koga, T., Cronin, S. B., Dresselhaus, M. S., Liu, J. L. & Wang, K. L. Experimental proof-of-principle investigation of enhanced Z<sub>(3D)</sub>T in (001) oriented Si/Ge superlattices. *Appl. Phys. Lett.* **77**, 1490-1492 (2000).
- 17 Samarelli, A. *et al.* The thermoelectric properties of Ge/SiGe modulation doped superlattices. *J. Appl. Phys.* **113**, 233704 (2013).
- 18 Peranio, N., Eibl, O. & Nurnus, J. Structural and thermoelectric properties of epitaxially grown Bi<sub>2</sub>Te<sub>3</sub> thin films and superlattices. *J. Appl. Phys.* **100**, 114306 (2006).
- 19 Zhang, Y. *et al.* Thermoelectric phase diagram of the SrTiO<sub>3</sub>-SrNbO<sub>3</sub> solid solution system. *J. Appl. Phys.* **121**, 185102 (2017).
- 20 Shannon, R. D. Revised Effective Ionic-Radii and Systematic Studies of Interatomic Distances in Halides and Chalcogenides. *Acta Crystallogr A* **32**, 751-767 (1976).
- 21 Mune, Y., Ohta, H., Koumoto, K., Mizoguchi, T. & Ikuhara, Y. Enhanced Seebeck coefficient of quantum-confined electrons in SrTiO<sub>3</sub>/SrTi<sub>0.8</sub>Nb<sub>0.2</sub>O<sub>3</sub> superlattices. *Appl. Phys. Lett.* **91**, 192105 (2007).
- 22 Blochl, P. E. Projector Augmented-Wave Method. *Phys Rev B* **50**, 17953-17979 (1994).
- 23 Kresse, G. & Joubert, D. From ultrasoft pseudopotentials to the projector augmented-wave method. *Phys Rev B* **59**, 1758-1775 (1999).
- 24 Kresse, G. & Furthmuller, J. Efficient iterative schemes for ab initio total-energy calculations using a plane-wave basis set. *Phys Rev B* **54**, 11169-11186 (1996).
- 25 Heyd, J., Scuseria, G. E. & Ernzerhof, M. Hybrid functionals based on a screened Coulomb potential. *J. Chem. Phys.* **124**, 219906 (2006).

4. *Fabrication and Thermoelectric Properties of SrTi<sub>1-x</sub>Nb<sub>x</sub>O<sub>3</sub>/SrTiO<sub>3</sub> (0.1 ≤ x ≤ 0.9) Superlattices*

- 26 Krukau, A. V., Vydrov, O. A., Izmaylov, A. F. & Scuseria, G. E. Influence of the exchange screening parameter on the performance of screened hybrid functionals. *J. Chem. Phys.* **125**, 224106 (2006).
- 27 Heyd, J., Scuseria, G. E. & Ernzerhof, M. Hybrid functionals based on a screened Coulomb potential. *J Chem Phys* **118**, 8207-8215 (2003).
- 28 Ohtomo, A., Muller, D. A., Grazul, J. L. & Hwang, H. Y. Artificial charge-modulation in atomic-scale perovskite titanate superlattices. *Nature* **419**, 378-380 (2002).
- 29 Mizoguchi, T., Ohta, H., Lee, H. S., Takahashi, N. & Ikuhara, Y. Controlling Interface Intermixing and Properties of SrTiO<sub>3</sub>-Based Superlattices. *Adv. Funct. Mater.* **21**, 2258-2263 (2011).
- 30 Delugas, P. *et al.* Doping-induced dimensional crossover and thermopower burst in Nb-doped SrTiO<sub>3</sub> superlattices. *Phys Rev B* **88**, 045310 (2013).
- 31 Ravichandran, J. *et al.* Crossover from incoherent to coherent phonon scattering in epitaxial oxide superlattices. *Nature Mater.* **13**, 168-172 (2014).

## 5. Summary

In this study, we have clarified thermoelectric phase diagram for SrTiO<sub>3</sub>-SrNbO<sub>3</sub> full range solid solution based epitaxial films and artificial superlattices.

In the first part, thermoelectric phase diagram of SrTiO<sub>3</sub>-SrNbO<sub>3</sub> full range solid solutions was clarified. By PLD method, we successfully fabricated high quality SrTi<sub>1-x</sub>Nb<sub>x</sub>O<sub>3</sub> (0.05 ≤ *x* ≤ 1) epitaxial thin films. Two phase boundaries were revealed, which are dominated by a step decrease in *m*<sup>\*</sup> at *x* = 0.3 and a minimum in  $\mu_{\text{Hall}}$  at *x* = 0.5. Due to the transition of parabolic conduction band from Ti 3d to Nb 4d at *x* = 0.3, the *m*<sup>\*</sup> decreases from ~1.1*m*<sub>e</sub> to ~0.7*m*<sub>e</sub>. Isovalent/heterovalent B-site substitution was found in SrTi<sub>1-x</sub>Nb<sub>x</sub>O<sub>3</sub> with increasing *x*. As *x* ~ 0.5, the B site of SrTi<sub>0.5</sub>Nb<sub>0.5</sub>O<sub>3</sub> is composed of Ti<sup>4+</sup> and Nb<sup>4+</sup> ions with a tetragonal distortion, which further leads to a formation of tail-like impurity bands and maximizes the electron scattering. The thermoelectric phase diagram of SrTiO<sub>3</sub>-SrNbO<sub>3</sub> full range solid solutions revealed in this study will provide guidance for further developments in SrTi<sub>1-x</sub>Nb<sub>x</sub>O<sub>3</sub> based thermoelectric materials.

In the second part, ascribed to the conduction band transition in SrTiO<sub>3</sub>-SrNbO<sub>3</sub> full range solid solutions,  $\lambda_{\text{D}}$  was calculated to increase from 4.1 nm to 5.3 nm at *x* = 0.3 in SrTi<sub>1-x</sub>Nb<sub>x</sub>O<sub>3</sub>. As a result, SrTi<sub>1-x</sub>Nb<sub>x</sub>O<sub>3</sub> could be divided into two regions by the point of *x* = 0.3 (*x* ≤ 0.3 → Region A, *x* > 0.3 → Region B). Using [*N* unit cell SrTi<sub>1-x</sub>Nb<sub>x</sub>O<sub>3</sub>]*N*[11 unit cell SrTiO<sub>3</sub>]<sub>10</sub> (1 ≤ *N* ≤ 12, *x* = 0.2, 0.3 and 0.8) superlattice structures, we observed a *S* enhancement factor of 10 in superlattices with *x* = 0.8, which is much higher than the 4 and 5 in superlattices with *x* = 0.2 and 0.3. Using the high enhancement factor of *S* in region B, we successfully increased the effective PF to 5 mW m<sup>-1</sup> K<sup>-2</sup> in [1 unit cell SrTi<sub>0.4</sub>Nb<sub>0.6</sub>O<sub>3</sub>]*N*[11 unit cell SrTiO<sub>3</sub>]<sub>10</sub> at room temperature, realizing a 200% enhancement

## 5. *Summary*

compared with bulk counterparts. In this part, we experimentally proved the effectiveness of 2D confinement in enhancing thermoelectric performance. And using longer  $\lambda_D$  materials is a promising way to further increase performance of thermoelectric materials.

The research results presented in this thesis will not only provide design guidance for SrTiO<sub>3</sub> based thermoelectric materials, but also suggestions for other thermoelectric material systems.

## **Acknowledgements**

This research work was conducted under the kind guidance of Prof. Hiromichi Ohta at Research Institute for Electronic Science, Hokkaido University.

Firstly, I would like to express my deep gratitude to Prof. Hiromichi Ohta, my supervisor, for his generous guidance and supports. He has walked me through all the stages in my Ph.D course studying. During the three years in Japan, he provided constant helps not only in my research but also in my daily life. I benefit a lot from his rigorous attitudes and enthusiasm towards scientific research. The knowledge of research and attitudes towards life he taught me will always be helpful to me in the future.

Secondly, I would like to thank Prof. Yamanouchi (RIES, Hokkaido Univ.), Prof. Katase (Tokyo Institute of Technology) and Prof. Cho (RIES, Hokkaido Univ.) for the helps during my research life in Hokkaido University, whose advices have enriched my skills not only in experiments but also in theoretical knowledge.

Thirdly, I would like to show my gratitude to my colleagues, Dr. Anup Kumar Sanchelar (PD, RIES, Hokkaido Univ.), Mr. Takaki Onozato (Ph.D candidate, IST, Hokkaido Univ.), Ms. Mian Wei (Ph.D candidate, IST, Hokkaido Univ.), Ms. Gwoon Kim (Ph.D candidate, IST, Hokkaido Univ.), Ms. Doudou Liang (Ph.D candidate, USTB), Mr. Yukio Nezu (Master candidate, IST, Hokkaido Univ.), Mr. Tatsuro Oyamada (Master candidate, IST, Hokkaido Univ.) Mr. Yuzhang Wu (Master candidate, IST, Hokkaido Univ.) *et al.* for the helps during my study in Ohta's Lab. Especially, Mr. Onozato taught me a lot about the basic manipulation of facilities in laboratory.

I also really appreciate the collaborations from Prof. Ikuhara, Prof. Tohei and Prof. Feng from University of Tokyo on TEM measurement, Prof. Tanaka and Prof. Hayashi

### *Acknowledgements*

from Kyoto University on the theoretical calculation, and Prof. Sheu from National Chiao Tung University on TDTR measurement. Without their helps and discussions, I cannot fulfil my recent research works.

Finally I would like to show my deepest appreciation to my parents, my girlfriend and my motherland. Their supports have always been the greatest encouragement and driving force to my study and life in Japan.

Yuqiao Zhang

## Publication Lists

### Papers related to this thesis

1. Y. Zhang, B. Feng, H. Hayashi, C. Chang, Y. Sheu, I. Tanaka, Y. Ikuhara, and H. Ohta: 「Double thermoelectric power factor of a 2D electron system」, *Nature Commun.* **9**, 2224 (2018) (IF=12.353, TC=1 ※)
2. Y. Zhang, B. Feng, H. Hayashi, T. Tohei, I. Tanaka, Y. Ikuhara, and H. Ohta: 「Thermoelectric phase diagram of the SrTiO<sub>3</sub>-SrNbO<sub>3</sub> solid solution system」, *J. Appl. Phys.* **121**, 185102-1-7 (2017). (IF=2.176, TC=3 ※)

### Other papers

1. Y. Nezu, Y. Zhang, C. Chen, Y. Ikuhara, and H. Ohta: 「Solid-phase epitaxial film growth and optical properties of a ferroelectric oxide, Sr<sub>2</sub>Nb<sub>2</sub>O<sub>7</sub>」, *J. Appl. Phys.* **122**, 135305 (2017).
2. G. Kim, Y. Zhang, T. Min, H. Suh, J.H. Jang, H. Kong, J. Lee, J. Lee, T. Jeon, I. Lee, J. Cho, H. Ohta, and H. Jeon, 「Extremely light carrier-effective mass in a distorted simple metal oxide」, *Adv. Electron. Mater.* DOI: 10.1002/aelm.201800504.

## Presentation Lists

1. Y. Zhang, H.J. Cho, M. Mikami, W.S. Shin, W.S. Choi, and H. Ohta, “Anomalous phonon transport in  $\text{SrTi}_{1-x}\text{Nb}_x\text{O}_3$  alloy”, The 2nd Workshop on Functional Materials Science, Busan, South Korea, October 22-23, 2018
2. Yuqiao Zhang, Bin Feng, Hiroyuki Hayashi, Cheng-Ping Chang, Yu-Miin Sheu, Isao Tanaka, Yuichi Ikuhara, and Hiromichi Ohta, “Double thermoelectric power factor of a 2D electron system,  $\text{SrTiO}_3$ -based superlattice”, 日本セラミックス協会 第 31 回秋季シンポジウム, 名古屋工業大学 (愛知), 2018 年 9 月 5 日-7 日
3. Yuqiao Zhang, Bin Feng, Hiroyuki Hayashi, Cheng-Ping Chang, Yu-Miin Sheu, Isao Tanaka, Yuichi Ikuhara, Hiromichi Ohta, “Double thermoelectric power factor of a 2D electron system”, The first International Joint Symposium of CEFMS-NCTU, RCAS-AS (Taiwan) and 5-Star Alliance (Japan), National Chiao Tung University, Taiwan, 18th-20th May, 2018
4. Y. Zhang, B. Feng, H. Hayashi, I. Tanaka, Y. Ikuhara, and H. Ohta, “Double enhancement of thermoelectric power factor in advanced oxide two-dimensional electron system”, 2018 MRS Spring Meeting & Exhibit, Phoenix, Arizona, 2-6 April, 2018 (Oral)
5. Y. Zhang, B. Feng, H. Hayashi, I. Tanaka, Y. Ikuhara, and H. Ohta, “Double enhancement of thermoelectric power factor in advanced oxide two-dimensional

- electron system”, The 18th RIES-Hokudai International Symposium 極 [Kyoku], Chateraise Gateaux Kingdom Sapporo, Sapporo, Japan, 30 Nov.-1 Dec. 2017 (Poster)
6. Yuqiao Zhang, Bin Feng, Hiroyuki Hayashi, Isao Tanaka, Yuichi Ikuhara and Hiromichi Ohta, “Large enhancement in effective thermoelectric power factor of Sr(Ti,Nb)O<sub>3</sub> superlattice”, 平成 29 年度日本セラミックス協会 東北北海道支部 研究発表会, Sendai, Japan, 1-2 November, 2017 (Oral)
  7. Y. Zhang, B. Feng, H. Hayashi, T. Tohei, I. Tanaka, Y. Ikuhara, and H. Ohta, “Thermoelectric Performance of SrTi<sub>1-x</sub>Nb<sub>x</sub>O<sub>3</sub> System (Bulk and Superlattices)”, IUMRS-ICAM 2017 (The 15th International Conference on Advanced Materials), Yoshida Campus, Kyoto University, Kyoto, Japan, 27 Aug.-1 Sep. 2017 (Oral).
  8. Yu-Qiao Zhang, Feng Bin, Yuichi Ikuhara, and Hiromichi Ohta, “Thermoelectric power factor of Sr(Ti,Nb)O<sub>3</sub>/SrTiO<sub>3</sub> superlattices”, 新学術領域研究「ナノ構造情報」のフロンティア開拓 — 材料科学の新展開」第 5 回若手の会, Tokyo, Japan, 25-26 July, 2017 (Poster)
  9. Yu-Qiao Zhang and Hiromichi Ohta, “Effective power factor of Sr(Ti,Nb)O<sub>3</sub>/SrTiO<sub>3</sub> superlattices”, 第 64 回応用物理学会春季学術講演会, Yokohama, Japan, 14-17 March, 2017 (Oral)
  10. Yu-Qiao Zhang and Hiromichi Ohta, “Improvement of thermoelectric power factor of heavily Nb-doped SrTiO<sub>3</sub> superlattices”, 第 52 回応用物理学会北海道支部/第 13

- 回日本光学会北海道支部合同学術講演会, Kitami, Japan, 7-8 January, 2017  
(Oral)
11. Y. Zhang, T. Katase, T. Onozato, B. Feng, H. Hayashi, T. Tohei, I. Tanaka, Y. Ikuhara, and H. Ohta, “Thermoelectric properties of SrTiO<sub>3</sub>-SrNbO<sub>3</sub> full range solid solutions”, The 17th RIES-Hokudai International Symposium 柔 [Ju], Chateraise Gateaux Kingdom Sapporo, Sapporo, Japan, 13-14 Dec. 2016 (Poster)
  12. Y. Zhang, T. Onozato, T. Katase, and H. Ohta, “Thermoelectric properties of SrTiO<sub>3</sub>-SrNbO<sub>3</sub> full range solid solutions”, International Workshop on Oxide Electronics 23, Nanjing International Conference Hotel, Nanjing, China, 12-14 Oct. 2016 (poster)
  13. Yuqiao Zhang, Takaki Onozato, Takayoshi Katase, Hiromichi Ohta, “Electron transport properties of SrTiO<sub>3</sub>-SrNbO<sub>3</sub> full range solid solutions”, HOKUDAI-NCTU International Joint Symposium on Nano, Opto and Bio Sciences, Hokkaido University, Sapporo, Japan, 4-5 Oct. 2016 (poster)
  14. Yuqiao Zhang, Takayoshi Katase, Takaki Onozato, Bin Feng, Hiroyuki Hayashi, Tetsuya Tohei, Isao Tanaka, Yuichi Ikuhara, Hiromichi Ohta, “Hidden Electronic Phase Boundary in the SrTiO<sub>3</sub>-SrNbO<sub>3</sub> Solid-solution System”, 2016年 第77回応用物理学会秋季学術講演会, Niigata, Japan, 13-16 September, 2016 (Poster)
  15. Y. Zhang, T. Katase, T. Onozato, B. Feng, H. Hayashi, T. Tohei, I. Tanaka, Y. Ikuhara and H. Ohta, “Electron transport properties of SrTiO<sub>3</sub>-SrNbO<sub>3</sub> full range solid-

solution epitaxial films”, 新学術領域研究「ナノ構造情報のフロンティア開拓  
— 材料科学の新展開」第4回若手の会, Ibaraki, Japan, 25-26 July, 2016 (Poster)